CORRELATIONS BETWEEN LARGE-SCALE SOLAR PHOTOSPHERIC AND CHROMOSPHERIC MOTIONS, Ca II (K) EMISSION, AND MAGNETIC FIELDS

Thesis by

George Warren Simon

In Partial Fulfillment of the Requirements
For the Degree of
Doctor of Philosophy

California Institute of Technology
Pasadena, California

1963

ACKNOWLEDGEMENTS

I should like to thank in particular my thesis advisor, Professor R.B. Leighton, for his help in all phases of this research, and for his encouragement and patience. Many of the ideas pursued in the course of this investigation are his; without them this work would undoubtedly have been less fruitful and much more difficult.

Also I am very grateful to Dr. Robert Howard for the use of his 1958 magnetograph tracings, for his supervision of the experiment described in Part IV(F), and for several helpful discussions.

In addition I wish to thank Mr. Gary Fitzpatrick for his great help in several stages of the data reduction and in the observations. I appreciate very much the permission of Dr. R.W. Noyes to quote freely and extensively from his thesis (1) and thank both him and Mr. Neil Sheeley for many fruitful discussions and their help with the observations. Thanks also go to my father, Mr. Heinz Simon, for aid in data reduction.

Fellowships from the Hughes Aircraft Company and Space Technology Laboratories were greatly appreciated, as was financial and other aid from the California Institute of Technology, the United States Office of Naval Research, and the Mount Wilson and Palomar Observatories.

Finally, especial thanks are offered to my wife Patti, for assistance with observing, data reduction, typing, but most of all for her never failing optimism and encouragement.

ABSTRACT

As previously reported (2, 3), large-scale, principally horizontal, motions have been observed in the solar photosphere. These motions have a cellular appearance, with the flow proceeding from the center of each "cell" toward the outer boundary, with velocities of 0.3 - 0.5 km/sec. These cells are arranged in a more-or-less regular pattern over the solar surface, with an average cell diameter of 30000 - 35000 km. Cross-correlation measurements obtained by superposition of velocity plates and Ca II (λ3933) plates show that the K_{232} emission network occurs directly above the boundaries of the velocity cells. Downward velocities of 1.0 - 2.0 km/sec are observed in the wings of Hα ($\Delta\lambda$ = 0.7A) and Hβ ($\Delta\lambda$ = 0.4A). These localized motions exist in a network pattern which coincides with the position of the K_{232} emission and the velocity cell boundaries. The lifetime of the K_{232} network has been measured by cross-correlating plates taken at various time intervals, and has a mean life of 17 - 21 hours, in excellent agreement with the findings of Macris (4, 5). Using magnetograph measurements obtained by Howard (6), we find a very high degree of correlation between the positions of weak magnetic fields (1.5 - 15 gauss) and the K_{232} network, the correlation increasing as the field strength increases.

These observations suggest that the average solar magnetic field (0.5 - 1.0 gauss) is swept to the cell boundaries by the horizontal currents, and concentrates there in strengths several times greater than the average field. These narrow regions of

enhanced field strength could then account for the presence of the K_{2v2} emission at the cell boundaries, and perhaps also indirectly for the downflow of chromospheric material in this region, as well as the small "dots" of rising material seen at the edges of the downward flowing network, which may be spicules seen on the disc. The origin of the "supergranulation" may be related to helium ionization which occurs at a depth of $0.5 - 1.5 \times 10^4$ km in the sun. Most of these results have already been reported (7).

TABLE OF CONTENTS

I. INTRODUCTION

The observations described in this thesis were mainly obtained with the 60 foot solar tower telescope and 13 foot spectroheliograph at Mount Wilson Observatory during the summers of 1961 and 1962, using special auxiliary apparatuses designed by Professor Leighton (3, 8). This equipment has been described in great detail by Noyes (1); the reader is referred to his paper (henceforth called simply "RWN") if he desires more information than that found in reference 3.

Many of the measurements discussed in the following sections involve line-of-sight velocities of matter in the solar atmosphere. Using Leighton's apparatuses and well-known photographic subtraction techniques, these velocities appear on "Doppler plates" as density variations, which can then be analyzed by direct microphotometer tracings or by the use of statistical correlation methods. In addition we have analyzed a number of regular spectroheliograms taken in the K_{232} core of the Ca II (λ3933) line. A third source of data came from magnetographic (9, 10) observations of the solar magnetic field made with the 150 foot solar tower telescope and spectrograph at Mount Wilson. Some of these had been obtained earlier by Howard (6), and some were made during 1962 by Howard and the author.

In Part II of this paper we describe briefly some of the basic apparatus, observational procedures, and theory. This is followed

in Part III by a discussion of the techniques and problems of data reduction and an analysis of correlation functions. Part IV contains the bulk of this thesis, namely, a description of the observations and results. Finally in Part V we summarize the observations and offer some suggestions as to their possible interpretations.

Some of the results which are described in the following sections have already been reported (2, 3, 7). In particular, we shall often mention reference 3 in what follows, and henceforth will refer to it as "LNS."

II. BASIC APPARATUS, OBSERVATIONAL PROCEDURES, AND THEORY

A. Basic Apparatus

Since the spectroheliograph and associated equipment have been described in detail by RWN and LNS, we will here mention only an addition to the basic optical system which has been used extensively in this thesis research. This new instrument, designed by Leighton, is a concave mirror of 30 foot focal length mounted on a rotating arm, so that it can be easily swung either into the observing or into the storage position. In the observing position this mirror rests directly above the fixed-position 21 foot focal length mirror used for many years in making spectroheliograms having an image diameter of 5 cm. The new mirror has a 10 inch diameter, with 5 and 7 inch aperture stops also available. A flat, which also can be swung in and out of the telescope's optical path, returns the light to a focus at the entrance slit of the spectroheliograph; the resulting image size is 8.4 cm.

For many applications this new image has several important advantages over the 5 and 17 cm images available previously. The added size (area ratio of 2.82) over the 5 cm image provides much better spatial resolution, yet permits side-by-side <u>full disc</u> images of the sun to appear on the photographic plate when using the splitter, an impossibility when employing the 17 cm image. The advantage and importance of a full disc image when one attempts to line up two plates of the sun for cross correlations cannot be overemphasized, especially if the two plates show different

phenomena; e.g., velocity cells and the Ca II network.

Unfortunately, one difficulty exists with the 8.4 cm image, which prevents accurate photographic subtraction over the entire image when combining plates for Doppler sums or differences: The side-by-side images are approximately 0.4 mm different in size on the photographic plate. Thus any small-scale phenomena are "washed-out" in the cancellation steps except over a very small region of the sun.* The source of this difficulty had not been located at the time of this writing. For the study of large cells this error is not disastrous, since LC diameters are about 30000 km. However, it prevented successful study of the narrow velocity network seen in the wings of Hα and Hβ, and of small-scale low-strength magnetic fields by Leighton's method (8). These latter two phenomena were thus investigated by other techniques, namely the 17 cm image and the magnetograph, respectively.

B. Observational Procedures

The general method of data collection and reduction is described in detail by RWN, pp. 14-20. In the present study, which mainly involved the use of Doppler sum plates, the two plates were normally taken about two to three minutes apart, so that the small-scale oscillating field, analyzed by RWN (also see reference 11), is approximately 180° out of phase, and tends to "cancel

* At the center of the disc, an error of 0.4 mm corresponds to a solar distance of 6700 km for the 8.4 cm image.

itself out."

Observations were generally made during periods of "good" atmospheric seeing beginning shortly after sunrise and continuing for up to two hours. In the study of the Ca II network lifetime, spectroheliograms were taken at two to twelve hour intervals over a fifty hour period, whenever the sun was visible, regardless of seeing conditions.

Large cells were studied with the photospheric spectral lines Ca (λ6103), Ba^+ (λ4554), and Na (λ5896), while the chromospheric network was investigated with the Hα, Hβ, and Ca^+ (λ3933) lines.

C. Theory

The basic equation used in the study of line-of-sight velocities is that describing the Doppler shift of a spectral line. As discussed by RWN, pp. 24-27, we make a number of assumptions:

1. A line-of-sight velocity extending over an area large enough to be resolved by the instrument shifts the entire spectral line by an amount $\Delta\lambda = v\lambda/c$, without changing the shape or residual intensity of the line.

2. The slope of the line profile is constant over a wavelength range larger than any Doppler shift encountered.

3. The spectral line is symmetric; hence the slope has the same magnitude but opposite sign at equidistant points on the two wings of the line.

With these assumptions, the change in intensity at corresponding points on the two images (taken in opposite wings of the line) is directly proportional to the velocity at that point, increasing on one image, and decreasing an equal amount on the other. This can be expressed by the relation:

$$\delta = \frac{\Delta I}{I} = \pm \frac{v\lambda}{Ic} \cdot \frac{dI}{d\lambda} = \pm \frac{v\lambda}{c} \cdot \frac{d(\ln I)}{d\lambda} \qquad (1)$$

where I is the intensity, λ the wavelength, v the velocity on the sun, and c the velocity of light. That is, we can describe the variations of the velocity field by the intensity changes of the light incident on the photographic plate as follows:

$$I(x,y) = I_o(1 + \delta(x,y)), \qquad (2)$$

where I_o is the mean intensity and (x,y) are the coordinates on the plate.

Equation 2 involves a fourth assumption; namely, that only Doppler shifts change the light intensity. Actually there may be other fluctuations, such as temperature changes (which are canceled out in the photographic subtraction process), and other sources of "noise" (which may or may not cancel out). A conservative "limit of error" on velocities due to all sources of error has been estimated by RWN (pp. 31-36) as 30 - 40 percent.

The fifth assumption concerns the photographic plate sensitivity (gamma). We assume that it is constant over the range of intensities encountered, so that we may write for the transmission of the photographic plate:

$$T = \text{const} \times I^{-\gamma} = T_o(1 + \delta)^{-\gamma} \ . \qquad (3)$$

In addition it was assumed in LNS and RWN that gamma is unity during all stages of the photographic subtraction procedure. As will be discussed in Part III, this last assumption appears to be invalid.

A sixth assumption made both by RWN and LNS seems to be quite inaccurate. It was asserted in these two papers that $\Delta I/I \ll 1$, so that it is valid to expand $T = T_o(1 + \delta)^{\gamma}$ as $T = T_o(1 + \delta\gamma)$. This will also be discussed in Part III which follows.

To summarize the method for determining line-of-sight velocities on the sun, we measure point-by-point changes in the transmission on a Doppler sum (or difference) plate by microphotometer tracings or correlation functions (ref. Part III(B), following). If we know the gammas of the photographic plate, we can then compute δ by equation 3, and obtain the velocity by equation 1. The only missing information is the line profile slope $d(\ln I)/d\lambda$ which is determined from a calibration procedure described by RWN, pp. 30-31.

III. TECHNIQUES AND PROBLEMS IN DATA REDUCTION

A. The Gamma Problem

The complete darkroom procedures necessary to convert an original spectroheliogram into a Doppler sum (or difference) plate is described by RWN, pp. 18-19. One basic assumption made by LNS and RWN in the data reduction of a Doppler sum plate is that the plate sensitivity (gamma) is constant and equal to unity during the four exposure and development stages required in the photographic subtraction method. Let us now consider the more general case in which each gamma, though constant, may differ from the others. We use the symbol γ_o for the gamma of the initial exposure and development stage carried out at Mount Wilson Observatory. (This usually has a value between 2.0 and 2.5; ref. RWN, figure 2-2(b)). For the four subsequent darkroom stages we write γ_1, γ_2, γ_3, and γ_4, where γ_1 refers to the first contact print stage, γ_2 to the next (projection) stage, etc. For each stage which has a gamma γ, we apply equation 3; namely, $T = T_o(1 + \delta)^{-\gamma}$. Thus, suppose that the transmission of the original violet-wing spectroheliogram is given by

$$T = T_o(1 + \delta)^{-\gamma_o} , \tag{4}$$

then the contact print made from this plate has a transmission

$$T = T_o\left[(1 + \delta)^{-\gamma_o}\right]^{-\gamma_1} = T_o(1 + \delta)^{\gamma_o\gamma_1} \qquad (5)$$

where T_o in equation 5 is not the same as in equation 4. (T_o is just a normalization factor, and represents the average transmission on any plate). Next we glue the contact print (of the violet-wing spectroheliogram) to the original red-wing spectroheliogram and obtain for the transmission through the glued pair:

$$T = T_o(1 - \delta)^{-\gamma_o} \cdot (1 + \delta)^{\gamma_o\gamma_1} \qquad (6)$$

in which different signs occur in the two parenthetical expressions since an intensity change ($+ \delta$) on the violet side appears as ($- \delta$) on the red side. This procedure can be continued through all four darkroom stages, and results in the following final expression for the transmission of either member of a right-left pair:*

$$T = T_o(1 + \delta)^{-\gamma_o\gamma_2\gamma_4 - \gamma_o\gamma_1\gamma_2\gamma_3\gamma_4}(1 - \delta)^{\gamma_o\gamma_1\gamma_2\gamma_4 + \gamma_o\gamma_2\gamma_3\gamma_4} \qquad (7)$$

First note that γ_o appears as an exponent in all terms of equation 7, and can be neglected since γ_o also appears in the denominator of δ, and effectively cancels itself out if we expand $(1 + \delta)^{\gamma_o} = 1 + \delta\,\gamma_o + .5\,\delta^2\gamma_o(\gamma_o - 1) + \ldots$. (This cancellation is perfect through the second order expansion, and has an error in the third order of $.67\,\gamma_o\delta^3$, which is negligible since $\delta \approx 0.1$ in most cases.) In the following equations we thus replace δ by

---

* A right-left pair consists of two projection prints of a single plate. These prints are mirror images of each other, so that they may be placed in register with their emulsions in contact.

$\delta' = \delta\gamma_o$ and remove γ_o from the exponents in equation 7. (The prime in δ' will also be dropped for simplicity). Now consider that the assumptions of the earlier papers are valid; i.e., that $\gamma_1 = \gamma_2 = \gamma_3 = \gamma_4 = 1$, and that $\delta \ll 1$, so that we need to expand equation 7 only to first order in δ. Then we get

$$T = T_o(1 + \delta)^{-2} (1 - \delta)^2 \tag{8a}$$

$$\approx T_o(1 - 4\delta) \tag{8b}$$

which agrees with equation 2.15 of RWN. The accuracy of this expansion leaves much to be desired. If the gammas are unity, and δ has the typical values $\pm$ 0.1 as calculated by equation 8a, then the approximate values of δ from equation 8b are -0.1234 and 0.0827, errors of 23 percent and 17 percent, respectively. Occasionally, one encounters δ values as large as $\pm$ 0.3, which lead to approximate values -0.611 and 0.178, errors of 104 percent and 41 percent! The only justification for the use of equation 8b by LNS and RWN was the resulting simplification in analyzing autocorrelation functions (ref. Section C, following). In the present work, most of the calculations have been performed on an IBM 7090 computer; hence the correct expression (equation 7) was used.

Next we investigated the magnitudes of γ_1, γ_2, γ_3, and γ_4. Calibrated stepwedges were contact- and projection-printed according to the standard procedures developed earlier for processing Doppler plates. The transmission (T_i) through the original stepwedge was compared with that (T_p) of the printed stepwedge.

The slope of the resulting T_f vs T_i curve (on logarithmic paper) is the negative of gamma.* These curves are shown in Figure 1(a). The numbers labeled C and P along the bottom are the gammas for the values of ln T_i indicated by the arrows, C standing for contact print, P for projection print. Over the range of T_i values usually encountered, γ varies between 0.95 and 1.05 for the contact stage; this is reasonably constant and close to unity. However, in the projection stage, γ varies between 1.0 and 1.4, which can neither be called constant nor unity. With the present developer formula and development time, one would require much denser projection prints in order to get onto the straight line portion of the curve, and even if this were done, the resultant constant gamma would be between 1.3 and 1.4. Since this problem unfortunately was not recognized until after all the Doppler plates had been processed, it was decided to make an ex post facto attempt to estimate the actual gammas of the developed plates. An added difficulty is that now even equation 7 is inaccurate, since both γ_2 and γ_4 (the projection stages) are variable quantities. Therefore equation 7 was rewritten as

$$T = T_o\left(\frac{1 - \delta}{1 + \delta}\right)^{\gamma} \tag{9}$$

where γ is the average of $(\gamma_2\gamma_4 + \gamma_1\gamma_2\gamma_3\gamma_4)$ and $(\gamma_1\gamma_2\gamma_4 + \gamma_2\gamma_3\gamma_4)$,

---

* Speaking in a strict photographic sense one calls this slope "gamma" only if it is constant. We shall continue to use the term "gamma" even if we are operating in the knee or shoulder of the H-D curve, where the slope is changing.

Figure 1. a) Ln T_f vs ln T_i for contact (C) and projection (P) prints. Numbers labeled C and P indicate plate sensitivity (gamma) at various positions along curve.

b) Height of A-C function vs Doppler parameter δ^2 for three values of γ using "hexagonal-cell velocity" model. Dashed line is an approximate solution assuming validity of equation 8b.

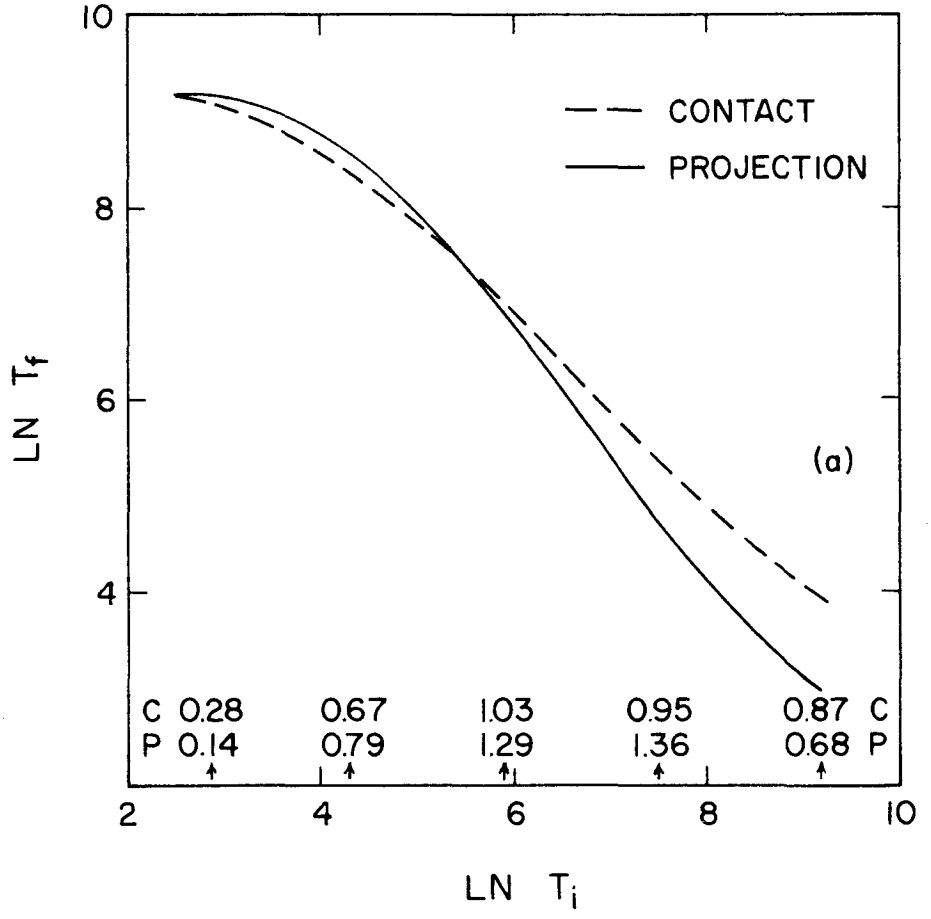

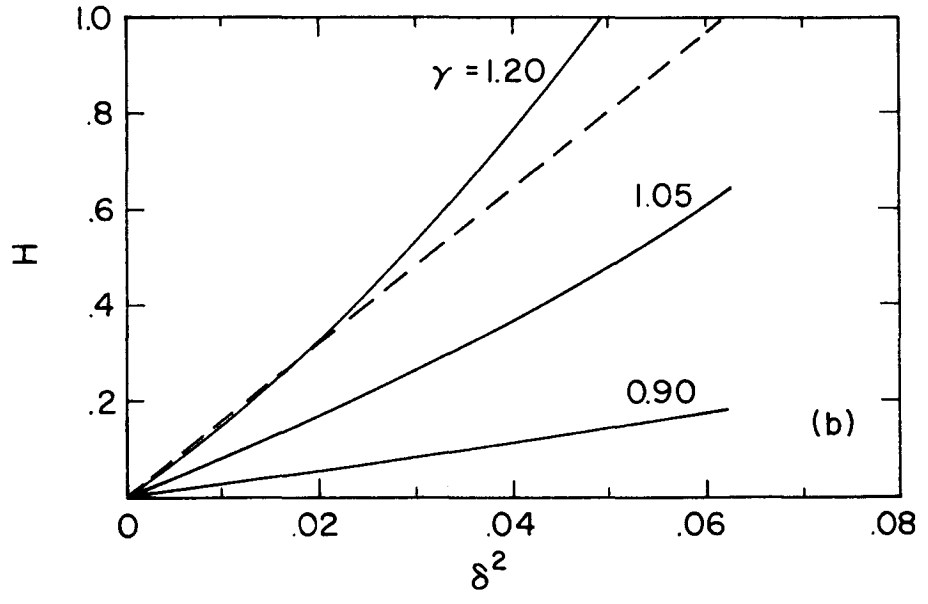

Figure 1. Caption on facing page.

and in which γ_2 and γ_4 are, we hope, reasonable averages of these two variables. This is admittedly not a very satisfactory solution to a rather complex problem, but it is somewhat better than simply using equation 8b. Previous estimates of the error in velocities due to deviations of gamma from unity were ± 10 percent. In light of these new difficulties, we must raise this error to 20 - 30 percent.

B. The Foreshortening-Removal Apparatus

In order to study the lifetime of the Ca II network (Part IV(D), following) by cross-correlation techniques it was necessary to "remove" the geometrical foreshortening of elements on the sun as seen from earth. This distortion has very much the same appearance as the well-known barrel distortion. To counteract this effect, we deliberately introduced pincushion distortion by placing a 6.5 inch diameter planoconvex condensing lens of 10 inch focal length directly above the photographic emulsion during the projection-printing stage. Since the apparent size of an object on the sun is $S(\theta) = S_o \cos \theta$, we attempted by trial and error to produce a distortion proportional to sec θ. With the distorting lens removed, normal images with magnifications M = 1.0, 1.2, and 1.4 were formed in the focal plane. The distorting lens was then introduced into the optical path, and the emulsion exposed. (The slight amount of defocusing which resulted was negligible.) Using the image of a piece of polar graph paper

as a test plate, it was easy to measure the distortion with a "comparator" normally used for measuring cosmic ray events. The results are shown in Figure 2(a), in which the dashed line is the correct sec θ curve for a 17 cm solar image and the horizontal line represents the usual uncorrected plate. It can be seen that the M = 1.4 curve which proved satisfactory lies within about one percent of the correct curve out to a radius of 1.9 inches,* which corresponds to $\theta = 34^{\circ}$. If we take 14° per day for the angular rotational velocity of the sun, it is thus possible to follow an object virtually distortionless across the sun from sunrise on the first day to sunset on the fifth day. In Figure 2(b) we show a normal uncorrected photo on the top, and a corrected one underneath. The scale of the latter has been adjusted so that objects at the center of the disc are of equal size in the two images.

C. Correlation Functions

The analysis of data by correlation techniques has been discussed both by LNS and RWN (pp. 20-24). They have also described a machine for photometrically obtaining two-dimensional correlation functions. For completeness we repeat the basic equation

---

* Larger radii could not be used due to limitations of lens size (6.5 inches) and plate size (4 × 5 inch).

Figure 2. a) Foreshortening removal through introduction of pincushion distortion. Dashed line represents perfect compensation for foreshortening; horizontal line illustrates usual uncorrected image.

b) Ca II (K_3) plate of 7/31/62. Upper photo is uncorrected image; lower one is corrected image with M = 1.4. Scale of photos agrees at center of the disc (marked by X), but lower image appears larger near edges of photo.

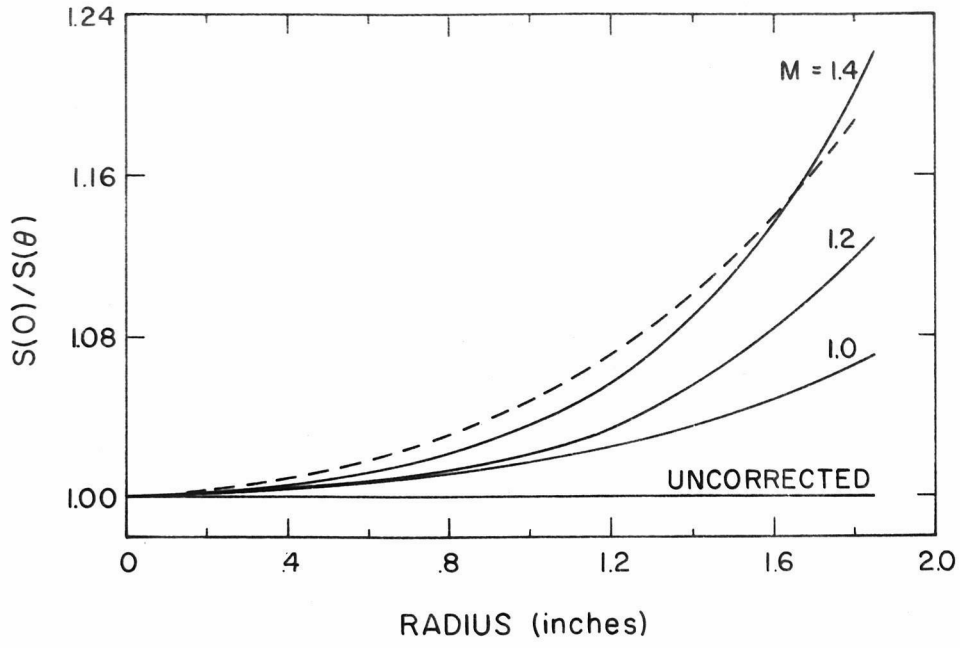

(a)

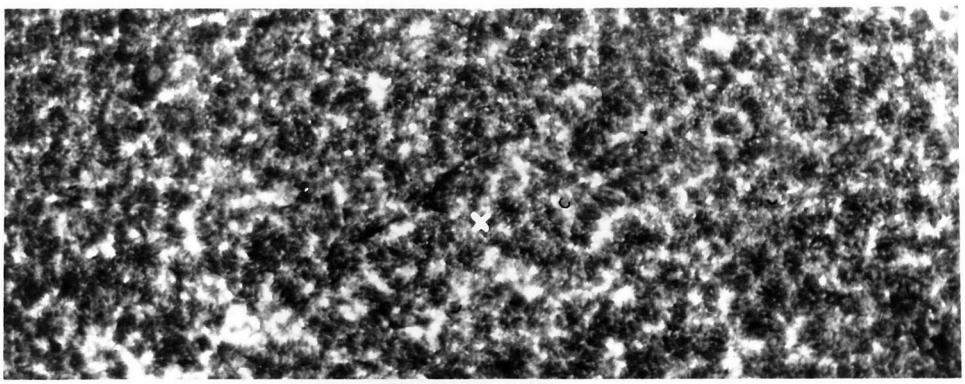

UNCORRECTED

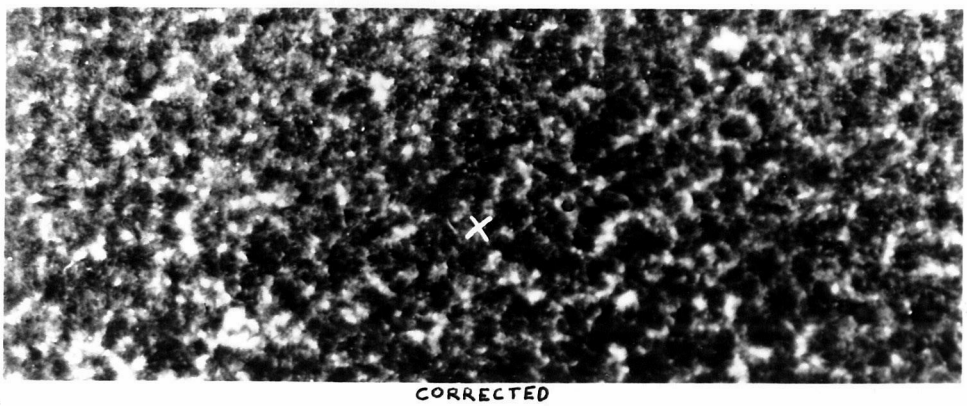

CORRECTED

Figure 2

for the correlation function C(s,t):

$$C(s,t) = \frac{K}{A} \iint T_1(x,y)\, T_2(x + s,\, y + t)\, dA$$

$$\equiv K \langle T_1(x,y)\, T_2(x + s,\, y + t) \rangle \qquad (10)$$

where A is the area of integration, T(x,y) is the transmission of the photographic plate, and K is a normalization constant. If $T_1 = T_2$, then C(s,t) is called an auto-correlation (A-C) function, and we redefine C(s,t) as AC(s,t). If T_1 is not equal to T_2, then C(s,t) is a cross-correlation (C-C) function, and is written CC(s,t).

Two pieces of information are easily extracted from C(s,t). One is the full width at half-maximum (FWHM) and the other is the height (H). The height is normally defined by

$$H = \frac{C(0,0) - C(\infty,\infty)}{C(\infty,\infty)} \quad . \qquad (11)$$

For the study of large cells in Part IV it is necessary to understand the relationship between H and the actual velocity field on the sun. To get a qualitative feeling for this relation we shall first consider four mathematically simple one-dimensional transmission functions, as illustrated in Figure 3. These four functions are Gaussian, triangular, rectangular, and sinusoidal, and each is shown both as a symmetric (S) and an antisymmetric (A) function about the origin. The horizontal scale of each has been chosen so that the transmission goes to zero at $x = \pm 1$*,

* Except for the Gaussian which extends to infinity and whose scale was selected so that the maximum transmission of the A function occurs at $x = \pm 0.5$, in agreement with the behavior of both the triangular and sinusoidal models.

Figure 3. "Theoretical" A-C curves for the various one-dimensional symmetric and antisymmetric functions shown in upper right-hand corner of each drawing. The horizontal and vertical scales have been chosen arbitrarily for convenient intercomparison. a, Gaussian; b, triangular; c, rectangular; d, sinusoidal.

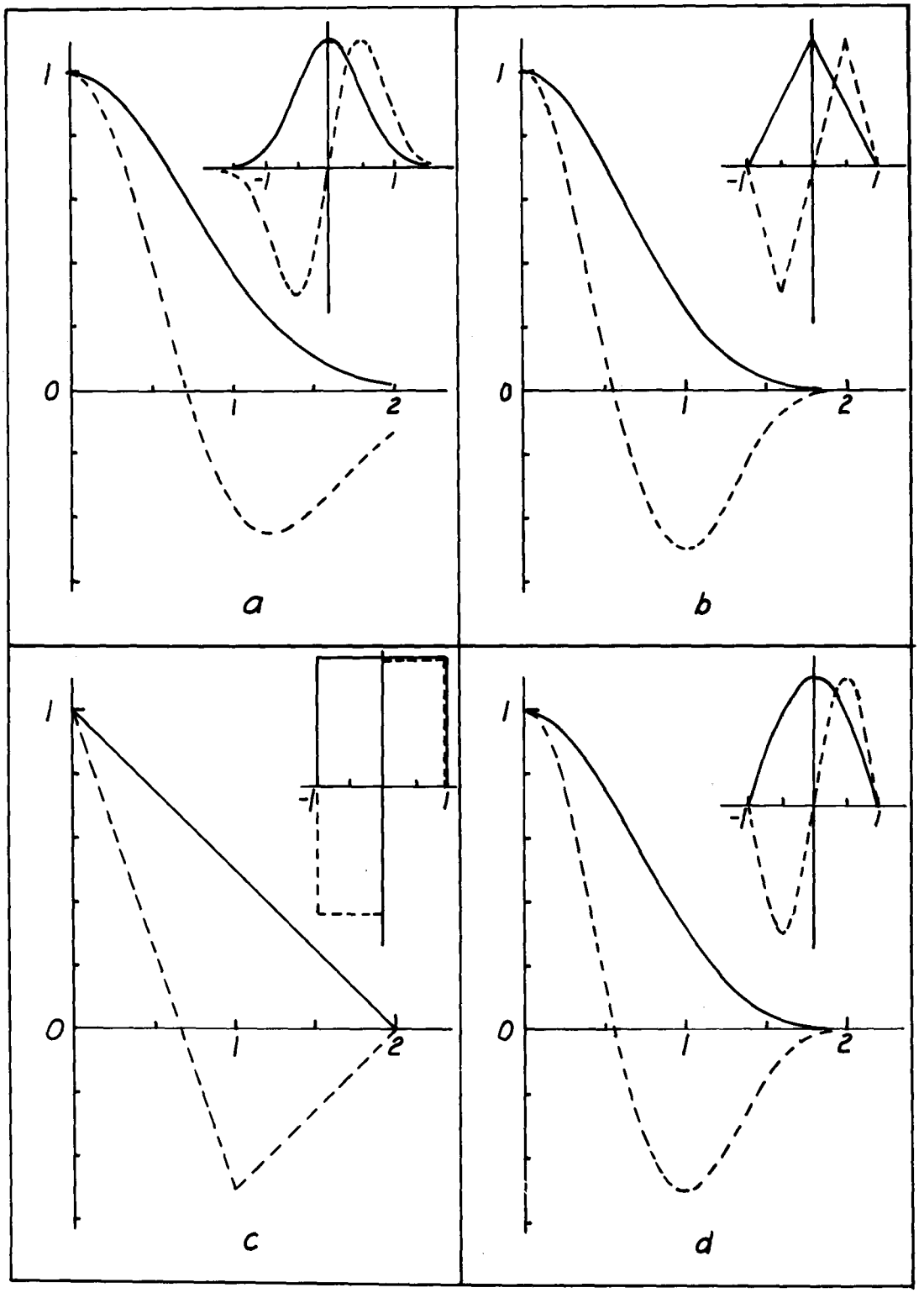

Figure 3

which correspond to the "cell boundaries;" i.e., the "cell size" is L = 2.0. The vertical scale of each was chosen so that C(0) = 1.0, for ease of intercomparison. The properties of the resultant A-C functions are summarized in Table 1.

Table 1

Function	Type	x_{min}	FWHM	H	TH
Gaussian	A	1.22	1.12	1.45	0.57
	S		1.64	1.00	
Triangular	A	1.0	0.88	1.50	0.33
	S		1.44	1.00	
Rectangular	A	1.0	1.00	1.50	1.00
	S		2.00	1.00	
Sinusoidal	A	1.0	0.92	1.50	0.50
	S		1.56	1.00	

Perhaps the most striking feature of these A-C functions is their similar appearance, despite the large variance in the originating functions. Several basic conclusions can be drawn. Antisymmetric functions always lead to a dip or "undershoot" in the A-C function. If we measure H not by equation 11, but by the total height from the top of the central maximum to the bottom of the undershoot, we see that this height in every case is very close to 1.5 times the height defined in equation 11. Secondly we note that the different A-C functions lead to consistent values for the FWHM. For A functions, the FWHM $\approx$ 0.5 L, while S functions

have FWHM's which are about 0.8 L. The cell size can also be measured in the case of A functions by the distance, $2x_{min}$, between the bottoms of the undershoots. This is roughly equal to the cell size L.

By normalizing all the heights C(0) to unity, we have hidden the one feature which clearly differentiates the various functions. Let us see what the unnormalized true height (TH) is for each case if the propagating function has a maximum transmission of unity. (This maximum occurs at x = 0 for S functions; at x = 0.5 for A functions.) These results are also shown in Table 1. Although the four true heights vary considerably, the two "reasonable," smoothly-varying functions, namely the sinusoidal and Gaussian, still are in good agreement.

All of the above qualitative discussion has been incorrect in two respects. Firstly we have calculated one-dimensional rather than two-dimensional integrals. Secondly we have assumed that the transmission at the cell boundary goes to zero; on a photographic plate it goes to an average transmission T_o. That is to say, we have been using a function $T = T_o\delta$, instead of the correct form given in equation 9. The more accurate formulation is required if we wish to interpret correctly the H vs δ dependence. Inserting equation 9 into equation 10, we have calculated the necessary two-dimensional numerical integrals on an IBM 7090 computer, using Weddle's rule, for two models. One is a sinusoidal function representing the horizontal velocity in large cells which is discussed in detail in Part IV(A). Results for

this model are shown in Figure 1(b) for three values of γ. This artificial gamma is the average of the darkroom gammas, namely $\gamma = (\gamma_1 + \gamma_2 + \gamma_3 + \gamma_4)/4$. The values γ = 1.20, 1.05, and 0.90 correspond roughly to the values encountered in Na (λ5896), Ca (λ6103), and Ba^+ (λ4554) plates, respectively. Also included is a dashed line which represents the result one obtains by assuming that all the gammas are unity and by using the first order expansion of equation 8b.

Not pictured is the second model which was used to interpret autocorrelations of the velocity network in Hα and Hβ, which will be discussed in Part IV(E). These observations show that this velocity network occurs at the boundaries of the large cells, and has a width approximately one-sixth of the average cell diameter L. Therefore we express this symmetric velocity field as an annulus with the form

$$\delta(\rho,\phi) = V_o \sin(3\pi\rho/R) \qquad 2/3 \leq \rho/R \leq 1 \qquad (12)$$

$$\delta(\rho,\phi) = 0 \qquad \rho/R > 1;\ \rho/R < 2/3 \qquad (13)$$

where (ρ,ϕ) are the co-ordinates of a plane-polar system with origin at the center of the cell. Note that equation 12 attains its maximum value at $\rho_o = 5R/6 = L/2$, where L is the cell diameter. These expressions for $\delta(\rho,\phi)$ are put into equations 9 and 10 and again integrated numerically to obtain H.

Finally, we must note that the above analysis has assumed that all cells have equal sizes and velocities. This is far from

the truth, so that the actual A-C functions obtained from large cell plates must be interpreted as representing an average size and velocity of all the cells in the field of view. Also we have assumed above that the value of $C(s,t)$ is $K\,T_o^2$ if we auto-correlate over separation distances larger than the cell size L. In actuality, we usually observe a secondary maximum at a distance L, due to neighboring cells. Fortunately, these subsidiary maxima are usually less than five percent of the central peak height H, and thus should not introduce sizable errors into the results.

Before continuing to Part IV and a description of the observations, we should note one modification made to the correlation machine (RWN, pp. 23-24) for the study of large cells. To permit "circular" scans parallel to the solar limb, a concentric circular gear track was attached to several of the plate holders. The plate holder was then rotated by a motor with a gear mounted on a vertical drive-shaft. For scans perpendicular to the solar limb, the previously described "linear" drive mechanism was employed.

IV. OBSERVATIONS AND RESULTS

In the following six sections, we shall begin with a description of the large-scale velocity cells. Then we will discuss the correlation between these cells and the Ca II (K) network. This will be followed by an analysis of two features of the Ca II network itself, its spatial structure and its lifetime. In the fifth section we shall discuss the velocity network seen in Hα and Hβ, and finally describe the correlation between the Ca II network and low-intensity magnetic fields.

A. The Large-Scale Velocity Field

One of the most interesting phenomena discovered by Leighton (2) in the first Doppler plates during the summer of 1960 was a system of "large cells" or "supergranulation," distributed rather uniformly over the solar surface. Such a Doppler sum photograph, taken in the wings ($\Delta\lambda = 0.07$A) of the Ca (λ6103) line with the 8.4 cm image, is shown in Figure 4. Three characteristics of these large cells (often abbreviated henceforth as "LC") are immediately apparent:

1. The cells virtually disappear into the grey background at the center of the disc, implying that this velocity field consists mostly of horizontal motions on the solar surface.

2. Away from the center of the disc, most of the individual cells, which range from roughly 20000 - 50000 km in size, have a definite polarity, with a dark side toward the limb, a light

Figure 4. Doppler sum plate of 6/11/62 taken in Ca (λ6103) line. Note system of large cells which disappear at center of the disc. Dark regions correspond to receding line-of-sight velocities.

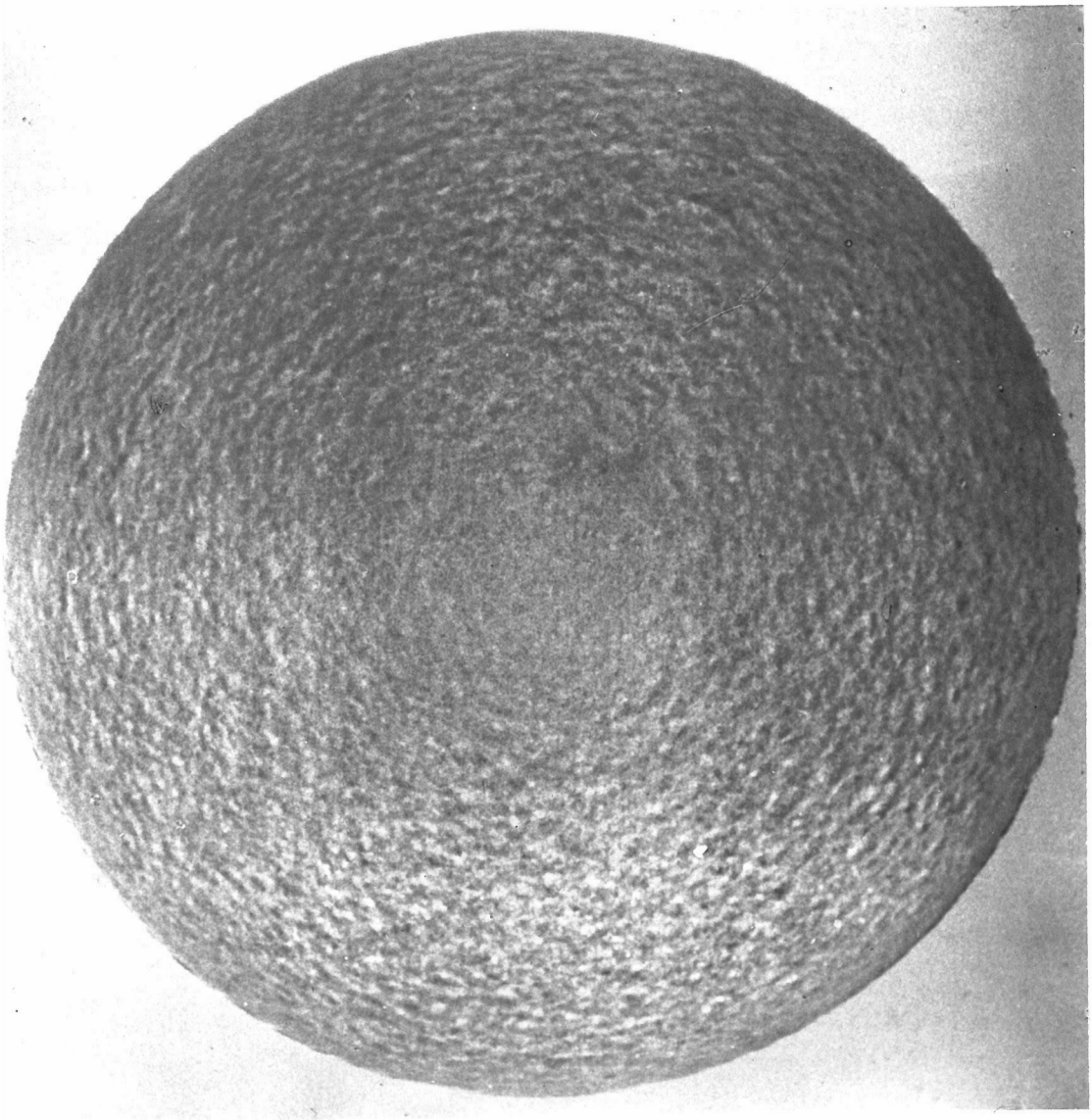

Figure 4

side nearer the center of the disc. On this photograph, dark regions correspond to receding line-of-sight velocities, while light areas are approaching.

3. In general the cells appear elongated parallel to the limb, as if seen in projection. That is, if the cells were visible at the disc center, they would have a roughly circular or perhaps polygonal plan form.

These observations taken together infer the existence of a system of mainly horizontal currents on the sun, distributed in cells several tens of thousands of kilometers in diameter, with the motion in each cell proceeding from the center toward the outer boundary.

Two other important properties of these cells are not apparent in Figure 4. One is the long lifetime ($\approx$ 20 hours) of the cells,* which is clearly demonstrated by the strong moiré pattern when two LC photos, taken several hours apart, are superimposed. The other property is the very faint appearance of rising velocities at the center of each cell, and a network of descending motions at the cell boundary, which is visible under close inspection (and perhaps with a bit of the observer's imagination added!) on some of these Doppler sum plates at the center of the disc.

Before going further into a detailed study of these cells, it

---

* The lifetime will be discussed in Section D, following.

should be pointed out that the existence of such large-scale horizontal motions has been suspected for many years, although they have not been seen on spectroheliograms until now. Wasiutynski (12) has reported that Janssen, in his classical granulation studies (13), discovered a "photospheric net" in 1877, with the granules sharply defined along the polygonal sides of this network, but obliterated or deformed within the polygons, as if distorted by horizontal currents.* The first positive identification of large-scale, long-lived motions in the photosphere was made in 1954 by Hart, who discovered them while spectroscopically measuring the equatorial rotation of the sun (16). In a subsequent investigation Miss Hart (17) found a subsidiary maximum at 26000 km in velocity auto-correlations, and a lifetime of at least several hours. Numerous other authors (18 - 22) have reported the presence of subsidiary maxima at roughly 15000 km while studying brightness and/or velocity fluctuations of the small-scale granulation field. Most recently, Evans and Michard (23) have confirmed the observations of LNS by finding large (10000 - 20000 km), non-periodic, horizontal motions near the limb of the sun.

Let us suppose now that it is possible to describe the velocity in a typical "cell" by $\underline{V}(\rho)$, where ρ is the radius vector of a plane polar co-ordinate system in the solar surface with origin

---

* Although Hansky (14) and Chevalier (15), who continued Janssen's work, both suspected that this network pattern was not a solar phenomenon, but rather due to distortions of Janssen's image due to poor seeing conditions.

at the center of the cell. The line-of-sight velocity component observed at an angle θ from the vertical is then:

$$V_L(x,z) = \frac{\beta z}{\rho} F_h(\rho) + \mu F_v(\rho) = G_h + G_v \qquad (14)$$

where $F_h(\rho)$ and $F_v(\rho)$ are the horizontal and vertical components of $\underline{V}(\rho)$, respectively, $\mu = \cos\theta$, $\beta = \sin\theta$, $z = y/\mu$, $x^2 + z^2 = \rho^2$, and (x,y) are rectangular coordinates on the photographic plate, with x parallel to the solar limb. Note that we compensate for geometrical foreshortening by use of the coordinate z in place of y.

We do not know, of course, what is the form of the actual solar functions F_h and F_v. However, we saw in Part III(C) that A-C curves are quite insensitive to the exact shape of the transmission function in the integrand; i.e., any "resonable" function will suffice. We shall use functions very similar to those described by Pellew and Southwell (24) for velocities in hexagonal convection cells, although, of course, their idealized convection model with fixed boundary conditions is certainly not a proper description of the complex solar phenomenon we are observing. These descriptive, though artificial, functions are:

$$F_h(\rho) = V_h \sin(2\pi\rho/L) \qquad (15)$$

and

$$F_v(\rho) = \frac{2V_v}{3}(S^2 + S - .5) \qquad (16)$$

where $S = \cos(4\pi\rho/3L)$ and L is the cell "diameter." Inserting

these functions in equation 14, we show schematically in Figure 5(a) the two components of $V_L(0,z)$, the horizontal component G_h with a solid line, the vertical G_v by a dashed line.

From our remarks at the beginning of this section, it follows that $V_h > V_v$. In addition, as we approach the limb, G_v is further reduced relative to G_h by the factor $\mu/\beta = \text{ctn } \theta$, until it is practically negligible. This is apparent from Figure 5(b), an actual microphotometer scan across a large cell, in a direction perpendicular to the limb (i.e., $V(0,z)$). This typical tracing shows a close resemblance to the sinusoidal character of G_h. Table 2 gives the average value of D and V_h from 45 such scans on 15 different cells in three different spectral lines. The quantity D is the separation distance between the two peaks in the sinusoidal velocity distribution; theoretically we thus expect that L = 2D = cell size. No appreciable difference is observed among the various lines, although of course the number of samples is small, and the results therefore statistically are not too significant. The quoted errors are standard deviations in the mean, and, in the case of V_h, do not include errors due to the uncertainty in gamma, which may be as large as 20 - 30 percent. The distribution of D sizes is shown in Figure 6(a).

With considerable difficulty, a few structures were found, at the center of the disc on the best LC plate studied, which <u>may</u> be large cells. These appeared to have cores of rising material and narrow boundaries of falling material. Microphotometer tracings

Figure 5. a) Theoretical model of velocity distribution in a large cell. Solid line represents horizontal component G_h; the dashed line represents vertical component G_v.

b) Actual microphotometer tracing across a cell on $Ba^+(\lambda 4554)$ Doppler sum plate of 6/23/62. Note similarity to solid line of Figure 5(a) above.

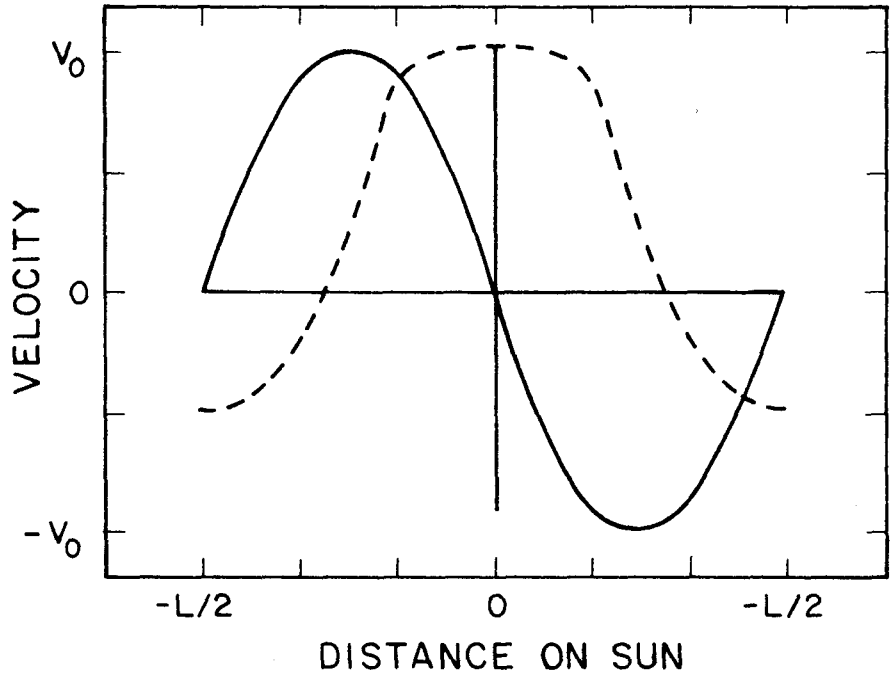

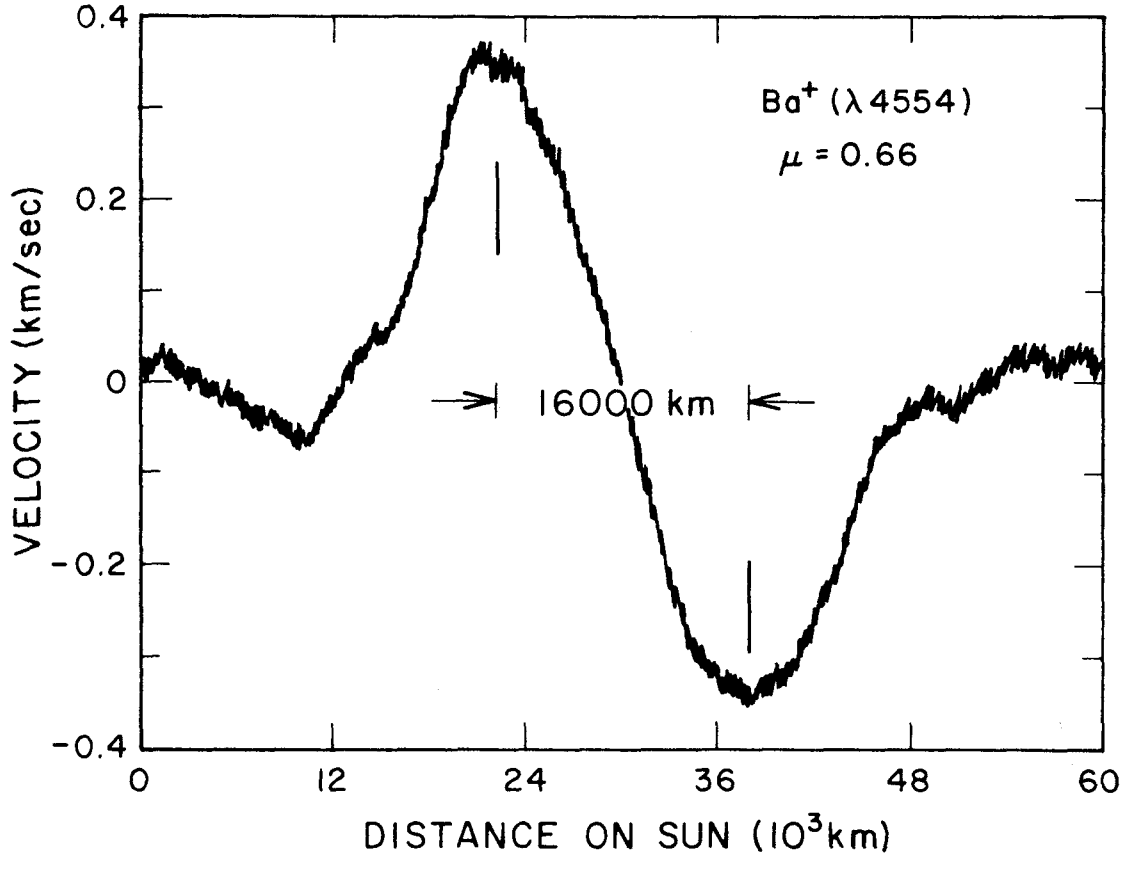

Figure 5. Caption on facing page.

Figure 6. a) Histogram showing spread in D sizes for 45 microphotometer tracings across large cells. Arrow indicates mean value of D.

b) Distribution of distances L to first subsidiary maxima on large cell A-C curves. L corresponds to the cell "diameter."

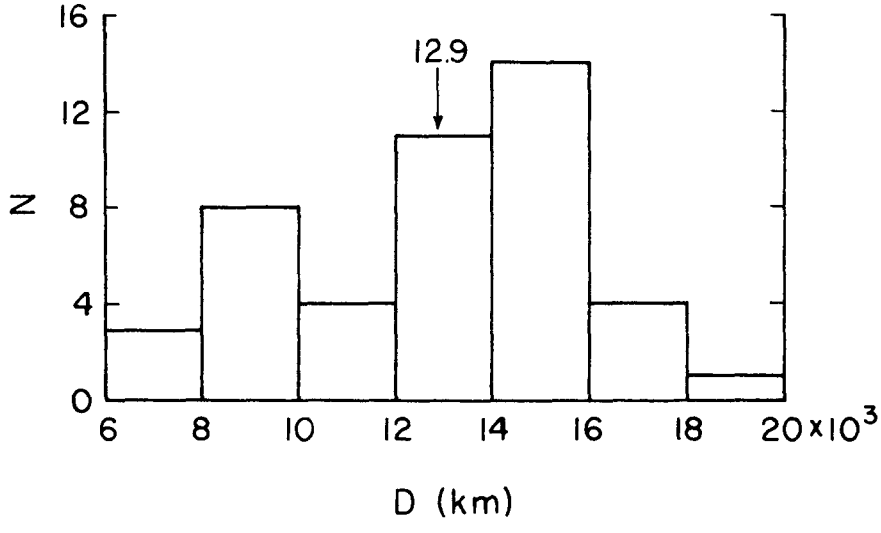

(a)

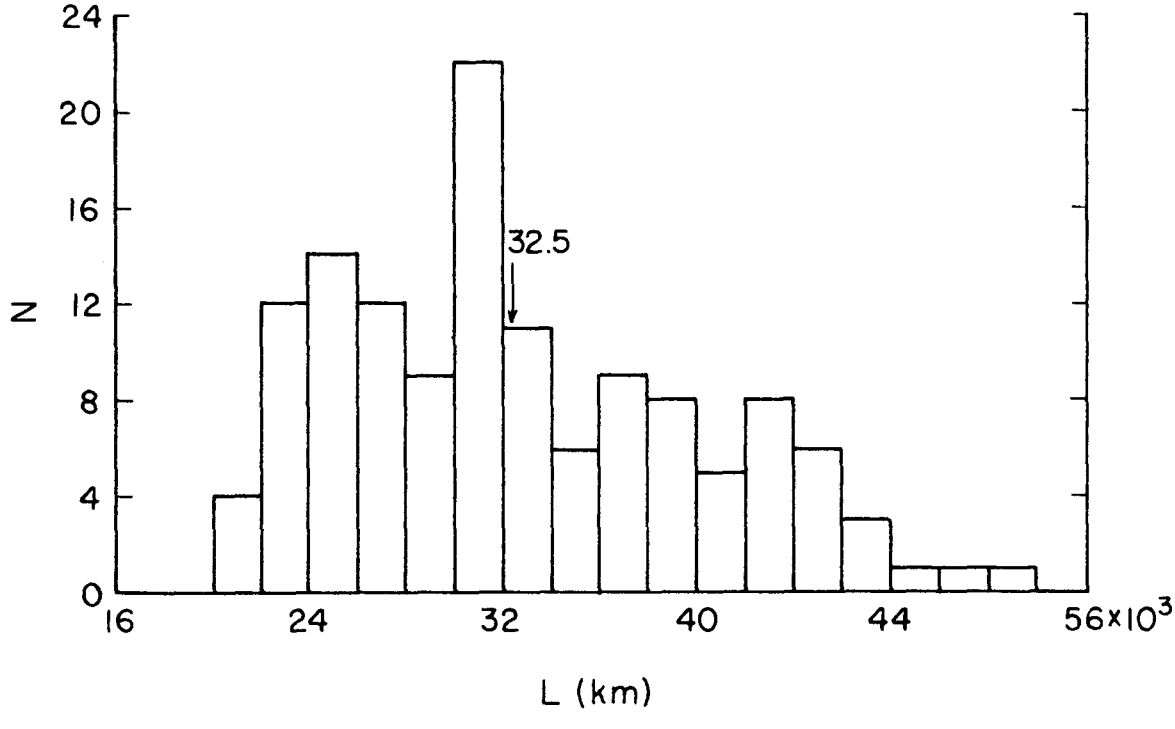

(b)

Figure 6. Caption on facing page.

Table 2

Line	Cells	Scans	μ	Image Size	D	V_h (km/sec)
Ca 6103	6	18	.52-.78	8.4 cm	11.6 ± 0.8	0.45
Ba^+4554	5	15	.61-.77	8.4 cm	14.0 ± 0.6	0.41
Na 5896	4	12	.45-.63	16.8 cm	13.6 ± 0.7	0.38
TOTAL	15	45	.45-.78	-	12.9 ± 0.4	0.42

across four such objects yielded velocities V_v of 0.13 - 0.30 km/sec. with an average of 0.20 km/sec. If these are indeed large cells, then it would seem that the vertical velocity in a cell in general does not exceed about 50 percent of the horizontal component.

To increase the statistical significance of the measurements, we next analyzed the LC velocities and sizes with A-C functions. Since the functions G_v and G_h of equation 14 are symmetric and anti-symmetric functions about the (x,z) origin, respectively, then cross-terms in the A-C function disappear,* and we can write:

$$C(s,t) = \beta^2 C_h(s,t) + \mu^2 C_v(s,t) \qquad (17)$$

where C_h and C_v, the A-C functions of the horizontal and vertical velocities, respectively, are independent of θ. The same result is obtained if for example G_v is a random, or time-oscillating function with $(G_v)_{ave} = 0$, and G_h is any arbitrary function. Rewriting equation 17 in terms of the height (H) of the A-C function, and noting that $\mu^2 = 1 - \beta^2$, we get:

---

* This is strictly true only in the limit of very small velocities, such that we may write $\left(\frac{1+\delta}{1-\delta}\right)^{\gamma} \approx (1 + 2\delta\gamma)$.

$$H = H_v + \beta^2 (H_h - H_v) \tag{18}$$

which is a straight line when using (β^2, H) coordinates, such that $H = H_v$ when $\theta = 0^\circ$, and $H = H_h$ when $\theta = 90^\circ$.

Six 8.4 cm *LC* plates were studied by this technique. On each plate 27 A-C scans were made at 13 different radial positions, the field of view consisting of annular openings with widths corresponding to distances of 120000 - 170000 km on the sun. Fourteen of the scans on each plate were made perpendicular to the solar limb (the z direction), the others parallel to the limb. A complete annulus was used for the "parallel" scans, but only a 40° sector centered on the z axis was open for the "perpendicular" tracings. Results for one of the six plates are shown in Figure 7(a). It will be noted that $H_\perp$ and $H_{||}$ converge as $\theta \to 0^\circ$, but diverge as $\theta \to 90^\circ$.* Also $H_\perp$ is larger than $H_{||}$. We have pointed out in Part III(C) that H for an antisymmetric function (such as G_h in equation 14 for scans perpendicular to the limb) is roughly 1.5 times the height of the corresponding symmetric function (G_h scanned parallel to the limb). If we take the ratio $H_\perp/H_{||}$ at the limb (where H is due entirely to the horizontal motions) for the six plates studied we find the average ratio to be 1.54, surprisingly (and probably fortuitously) close to the predicted value. A typical pair of actual A-C scans is shown in Figure 8. These point out the striking differences between the appearance of scans made

* The straight-line fits include only points for which β^2 is less than 0.4. Beyond this point, as one approaches the limb of the sun, loss of spatial resolution smears out or obscures the contribution of the smaller elements, thus reducing the height of the A-C curve.

Figure 7. a) Height of A-C curve as function of $\sin^2\theta$ for scans parallel and perpendicular to the limb; Ca (λ6103) plate of 6/23/62. Solid line is least-squares fit of data for $\sin^2\theta < 0.4$.

b) Composite curve of FWHM vs sin θ for all six cases studied.

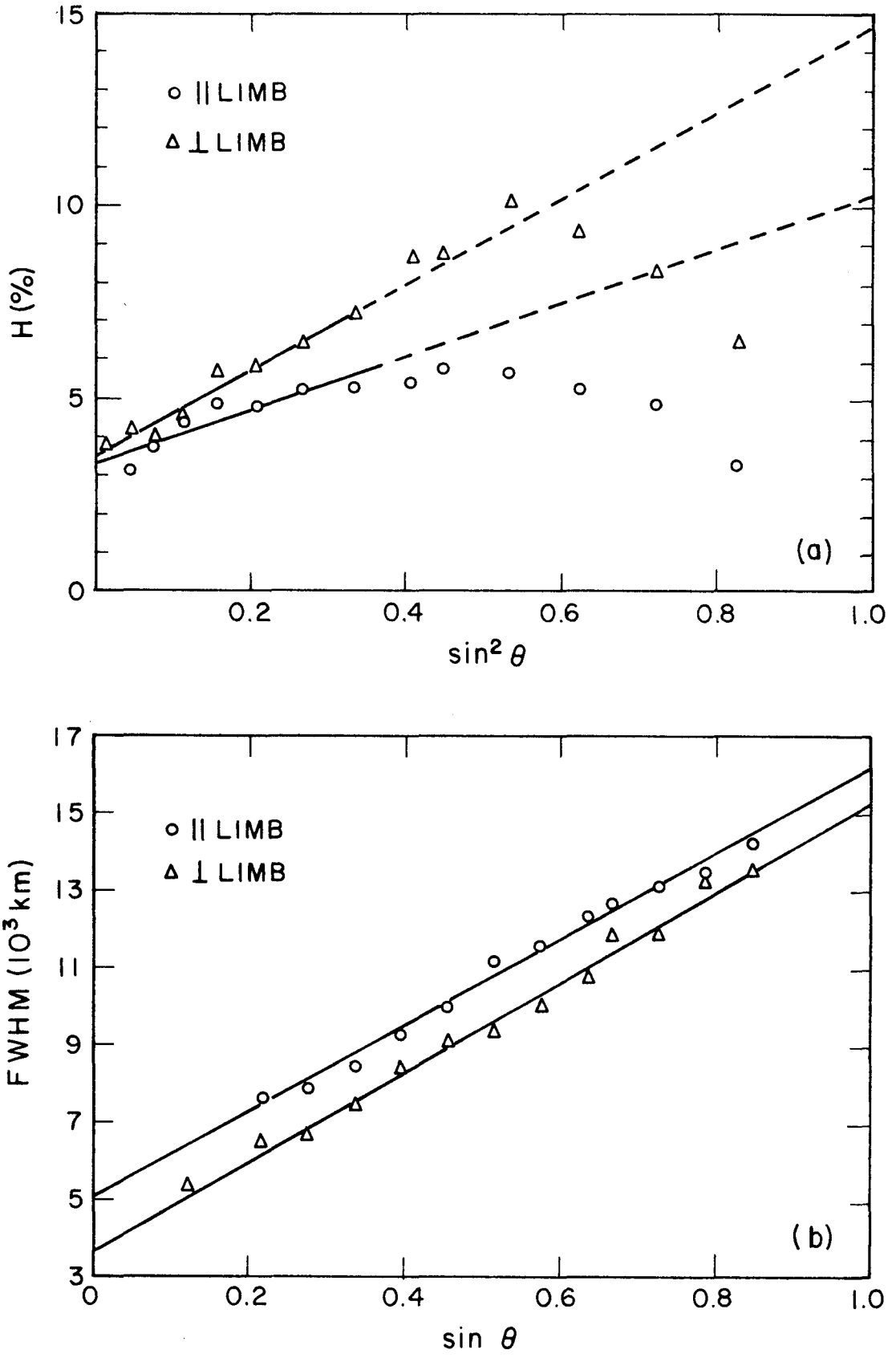

Figure 7. Caption on facing page.

Figure 8. a) Actual tracing of an A-C function scanned parallel to the limb.

b) Same region of same plate as in a) above; scan perpendicular to limb. Note secondary maxima at 32×10^3 km and 62×10^3 km.

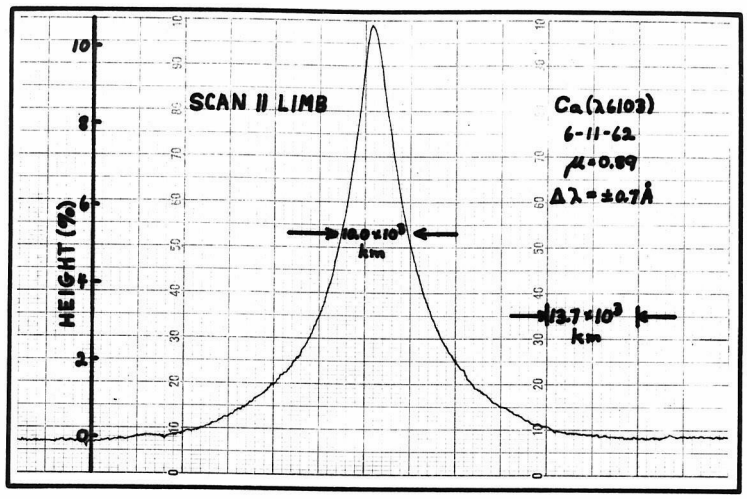
SCAN II LIMB
HEIGHT (%)
Ca (λ6102)
6-11-62
μ = 0.89
Δλ = ±0.7Å
10.9 × 10³ km
13.7 × 10³ km

a.

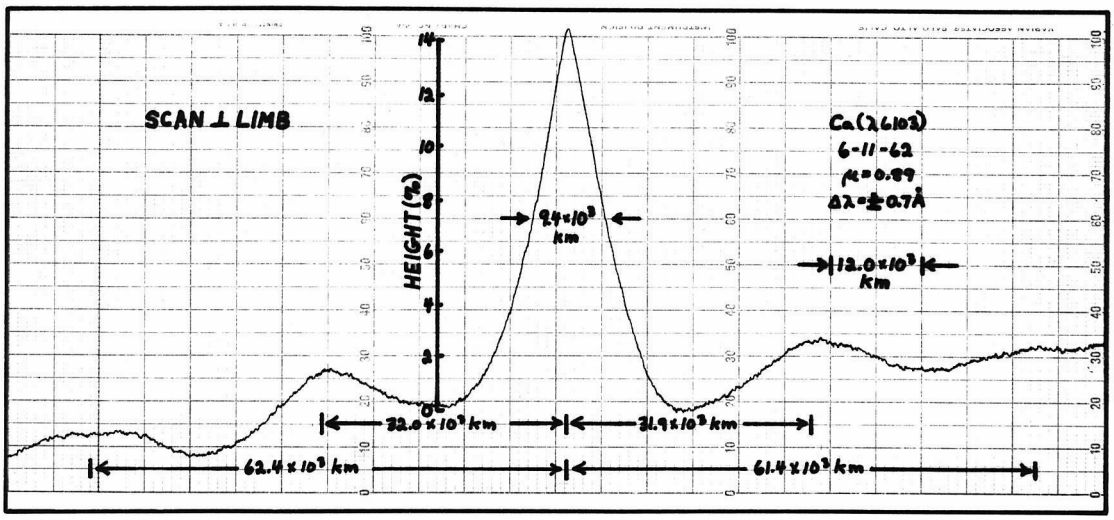
SCAN ⊥ LIMB
HEIGHT (%)
Ca (λ6102)
6-11-62
μ = 0.89
Δλ = ±0.7Å
9.4 × 10³ km
12.0 × 10³ km
32.0 × 10³ km
31.9 × 10³ km
62.4 × 10³ km
61.4 × 10³ km

b.

Figure 8

parallel and perpendicular to the limb, at the same place on a single image of the sun.

Two other characteristics of such tracings can be seen in Figure 8. One is the smaller width (FWHM) of the scan perpendicular to the limb, the second is the presence of secondary maxima for the perpendicular scans.* For the hypothetical function $F_h(\rho)$ described in equation 15 the FWHM is 0.44L for perpendicular scans, 0.64L for parallel scans, where L is the cell diameter. In Figure 7(b) we have plotted the average FWHM versus $\beta = \sin\theta$ for all six cases combined. The steady decrease in FWHM as $\beta \to 0$ is due to the superposition of the large-scale mainly horizontal motion and the small-scale mainly vertical oscillatory field discussed by RWN. As $\beta \to 1$, this small-scale motion mainly disappears, so that the remaining FWHM is due primarily to the large-scale motion. A least-squares straight line fit to this data gives a FWHM at $\theta = 90^\circ$ of 15.3×10^3 km and 16.2×10^3 km for the perpendicular and parallel scans, respectively. Using the theoretical relation above between FWHM and L, we then obtain an average cell size of 34.8×10^3 km and 25.3×10^3 km, respectively.** Since

* In perpendicular-to-the-limb scans, secondary maxima occur almost 100 percent of the time, while only occasional (perhaps 10 percent) parallel-to-limb scans show weak secondary maxima.

** Note that the FWHM values quoted above agree very well with those published in LNS. However, an error was made in LNS in equating the FWHM to the cell size; subsequent analysis of A-C functions indicates that L, not FWHM, is more representative of the cell size, where $L \approx 2$ FWHM; i.e., about 30000 km.

these latter two numbers should agree if our model is correct, either the model is not too successful in this regard, or else there still remains enough small-scale field (even at $\theta = 90^{o}$) to mask out most of the predicted size difference between the two types of scans. However, the model is at least qualitatively correct, because in every case studied, the FWHM for parallel scans was larger than for perpendicular ones. In addition, it is worth noting that the above results demonstrate the approximately polygonal, or circular, cell shape, since the perpendicular scans have all been corrected for geometrical foreshortening, while the parallel scans have not, and yet both types lead to roughly equal cell sizes.

The secondary maxima imply some sort of periodicity or local order to the cell structure. That is, we can define an average "cell spacing" or "cell diameter" by a quantity L. Sometimes, as in Figure 8(b), we are able to see a second, and occasionally even a third subsidiary maximum. Returning to Figure 6(b), we have plotted the distribution of the distances to the first subsidiary maximum for 132 measurements from A-C tracings of the six plates studied. The average value for L is 32.5×10^{3} km. Since the range of L sizes varies from 20000 - 54000 km, one concludes that there exists a large spread in cell sizes, and at most we can claim only a quasi-periodicity for the cell spacing. This problem will be discussed further in Sections B and C, following.

Let us return now to the interpretation of the heights of

the A-C curves. Since the sinusoidal velocity distribution seems to be a reasonable approximation to the true velocity variation across a large cell, we have calculated the H vs. δ dependence of this function for several values of gamma, as discussed earlier in Part III(A), and as shown in Figure 1(b). From the measured values of H (at the limb, where H is primarily due to the large-scale velocity field), we read the value of δ from Figure 1(b), and then compute the velocity V_h of equation 15 directly from the Doppler equation 1. The results of these calculations are shown in Table 3.

Table 3

Case	Date	Line	V_h (km/sec)
1	6-11-62	Ca 6103	0.42
2	6-23-62	Ca 6103	0.35
3	6-27-62	Ca 6103	0.31
4	6-23-62	Ba^+4554	0.31
5	7-2-62	Ba^+4554	0.34
6	7-2-62	Ba^+4554	0.37

The average velocity from these six plates is 0.35 km/sec. Although the agreement between the velocities from the Ca (λ6103) and the Ba II (λ4554) plates appears to be excellent, this may be fortuitous, since the large uncertainty in gamma remains an unknown factor in these calculations. Comparing these velocities with those obtained from the direct microphotometer tracings shown

in Table 2, we note that the A-C scans give slightly smaller velocities. This is to be expected, since the A-C function is integrated over many cells, while the direct tracings were made across a few chosen cells which clearly had a "proper" cell appearance, and particularly good contrast (i.e., large velocity) between the dark and light halves of the cell.

There remains still the problem of the vertical motions in the large cells, which would be given by H at the center of the disc. Unfortunately there remains at the disc center the oscillating small scale field described by RWN. We have tried to eliminate this by forming Doppler sums from plates taken half an oscillation period apart, so that the small-scale contrast is at a minimum, also by use of the 8.4 cm image, rather than the 16.8 cm one, and finally by slight defocusing of the image. However, some of this granular motion remains, and is inseparably mixed with the large cell vertical motion. Thus it is not worthwhile analyzing H at the center of the disc in more than a short qualitative manner. The average height on these six plates at the center of the disc is about 55 percent of the height at the limb. Since the velocity goes roughly as the square root of the A-C height, this would imply vertical velocities about 75 percent of the horizontal velocities. Thus the upper limit for the vertical cell velocity is about 0.25 km/sec, assuming none of the height is due to the granulation field. This is, of course, very improbable. It seems much more likely that the center-of-the-disc height is due primarily

to the small-scale motion, since we recall that the FWHM in Figure 7(b) decreased sharply as one approaches the center of the disc. Thus our second attempt to definitely establish a large cell vertical motion also comes to an inconclusive end.

To conclude this section we note that if we take the measured cell spacing L, and compute the number of cells on the solar surface by the relation $N = 4\pi R_{\odot}^2/L^2$ we find $N = 5.8 \times 10^3$. Actual counts yield numbers in the range $4.0 - 5.5 \times 10^3$, indicating that the density of cells is not perfectly uniform or close-packed, a fact easily seen upon close inspection of a LC plate.

B. Correlation Between the Large Cells and the Ca II Network

In the previous section we have described a system of velocity cells which is distributed in a fairly uniform fashion across the solar surface. Immediately after discovery of the large cells, it was noticed that a rather strong moiré pattern could be produced by superimposing a cell plate upon a Ca II (K_{232}) spectroheliogram, and sliding one plate slowly across the other. This moiré pattern usually extends over two to four cell diameters, and persists even if the two plates were taken several hours apart. Not only did this imply at least a quasi-periodicity in the observed structures, but also a relatively long lifetime, of perhaps many hours. In this section we shall describe two methods which were used to prove that the boundaries of the large cells coincide with the positions of the emission network visible in the K_{232} core of Ca II (λ3933).

In the following two sections we shall then discuss the periodicity and lifetime of the network, respectively.

1. Correlation by Counting Individual Cells

The first successful attempt to describe quantitatively the correlation between the Ca II network and the large cells (henceforth called "K-LC correlation") was made as follows: An 8.4 cm K plate was placed in an enlarger and projected as a 46 cm image on a sheet of white paper. A drawing was made of the emission network. Then an 8.4 cm LC plate, taken within an hour or so of the K plate, was enlarged to the same scale, and a drawing made of all structures which appeared as cells to the viewer.* One observer then placed the two drawings in register and made four sets of identifying marks, one with the drawings in proper registration and three with one drawing rotated at successive 90° intervals. A second observer, who did not know which set of marks corresponded to the correct alignment, then measured the K-LC correlation for all four orientations of the two drawings in the following manner: The two figures were placed on a light box. Each cell on the LC drawing was assigned a letter C or A. A value "C" indicated that the cell "correlated;" i.e., it lay within or just touched the boundary of a K network polygon; an assignment "A" meant "anti-correlation;" i.e., the cell was intersected by one or more pieces

* To qualify as a cell, the object had to have the "right" polarity; i.e., receding velocity in the half of the cell nearer the limb of the sun.

of the K network structure. A few cells, though not intersected by the K network, were not counted as C, if they were a large distance (roughly more than one cell diameter) away from the nearest network piece. These cells were thrown out. This procedure was carried out twice (to check the observer's judgment consistency) for each of the four orientations, and for four pairs of drawings. Two of the LC drawings were made from Ca (λ6103) plates; two used Ba^{+}(λ4554).

For each pair of drawings, the three "wrong alignment" positions measured the probability P that a randomly placed, uncorrelated cell would appear as a "C" cell. In the correct orientation, the actual correlation was measured in terms of the number of C cells relative to the total number N counted; i.e., N = C + A. In terms of the quantity P defined above, the probability that at least C correlations would be observed in N trials, if the distribution of the cells is random, (i.e., uncorrelated with the K network) is given by the cumulative binomial probability E (C; N, P):

$$E\,(C;\,N,\,P) = \sum_{i\,=\,C}^{N} \frac{N!}{i!(N-i)!}\; P^{i}\,(1-P)^{N-i} \qquad (19)$$

For the four pairs of drawings investigated, the results are shown in Table 4.

Looking first at Cases 1 - 3, each of which involved plates with time differences less than a hour, one is immediately struck by the extremely small probability that the measured correlation is

Table 4

Case	Type	Date	Δt	N	C	P	C/N	E
1	Ca-K	6-27-62	12^m	492	387	.540	.786	3×10^{-22}
2	Ba-K	6-23-62	36^m	394	231	.511	.587	4×10^{-3}
3	Ca-K	6-22-62	49^m	275	185	.482	.672	3×10^{-10}
4	Ba-K	7-2-62	96^m	674	386	.603	.573	0.92

due to random statistical fluctuations in the cell-network distribution. Or, saying it in a more positive fashion, the very high (well over 99 percent) probability that the observed correlation is real.

However, in Case 4, one notes that the ratio C/N is only .573, actually less than P, while in the other cases, C/N is always greater than P. That is, the cells in Case 4 appear to be anti-correlated with the K network. This is borne out by the large value of E, which is over 90 percent. The time interval for this case probably explains the discrepancy. In 96 minutes, objects within 40° or so from the solar equator will move roughly 10000 km across the surface. This is approximately 1/3 the average network diameter (see Section C, following); thus many of the cells which correlated with the K network at $\Delta t = 0$ will now have moved enough to be intersected by segments of the K network.

Another point worth mentioning is the significance of the calculated values of E, which is seen to vary tremendously from case to case, over many powers of ten. For the large values of N

and C used in the E calculation, a small change in N or C causes an inordinately large change in E. Thus a small difference from trial to trial in the observer's judgment regarding whether a cell is to be counted as an A or a C, becomes unreasonably important to the answer. For example, in Case 3, a counting difference of two cells in N and C changed E by a factor of 13. In Table 4, we have quoted the average value of the two trials for each case. It should be pointed out that this type of behavior appears only in the extreme tail of the probability distribution curve: the E variation is much more gradual in Cases 2 and 4 than in 1 and 3.

Several other factors affect the value of E. These include the ability of the observer to correctly identify what cells are when making the drawing, his accuracy in aligning the two drawings and enlarging them to the same scale, "seeing" quality of the two plates, etc. Probably another significant contributor is the subconscious prejudice of the observer. When the correlation is very good, it is immediately obvious to him that the drawings are in proper alignment. Thus in Case 1, which had by far the best correlation due to excellent seeing and a very small Δt, the observer counted 18 fewer C's on the second trial then the first. This was by far the largest trial-to-trial variation of any of the four cases. It indicates either that the observer got a bit too enthused about the obviously "good" result on the first trial, or, what is more likely, he became too critical in his judgments on the second trial in the fear of having favorably prejudiced his first

results! This difference of 18 C's changed E by at least a factor of 10^{16}!

Thus we conclude that we cannot take the exact measured values of E too seriously, especially when it takes on extreme values. However, it seems safe to say that this method has been successful in demonstrating that a very strong correlation exists between the large cells and the Ca II network; this correlation is of a form such that the velocity cells are enclosed by the polygonal structure of the K network, not intersected by it.

2. Correlation From Direct Cross-Correlation Measurements

Since the above method proved the spatial coincidence of the cell boundaries and the K network, a new effort was made to verify this correlation directly from plates without recourse to an intermediate stage involving drawings. A similar attempt had failed in 1961 because of the great difficulty in aligning properly the two plates (17 cm. Doppler plates generally do not show opposite limbs of the sun). This problem was eliminated through use of the new 8.4 cm full-disc Doppler images available in 1962.

Consider the very schematic one-dimensional drawing of a superposition of the cells and K network, shown in Figure 9(a). Three cells are shown, one at the center of the disc, and one each on the "left" and "right" side of the disc, as seen by the observer. The dashed lines refer to the K emission network, the solid lines to the velocity field (assumed to be mainly horizontal motion in the left and right cells, and vertical at the

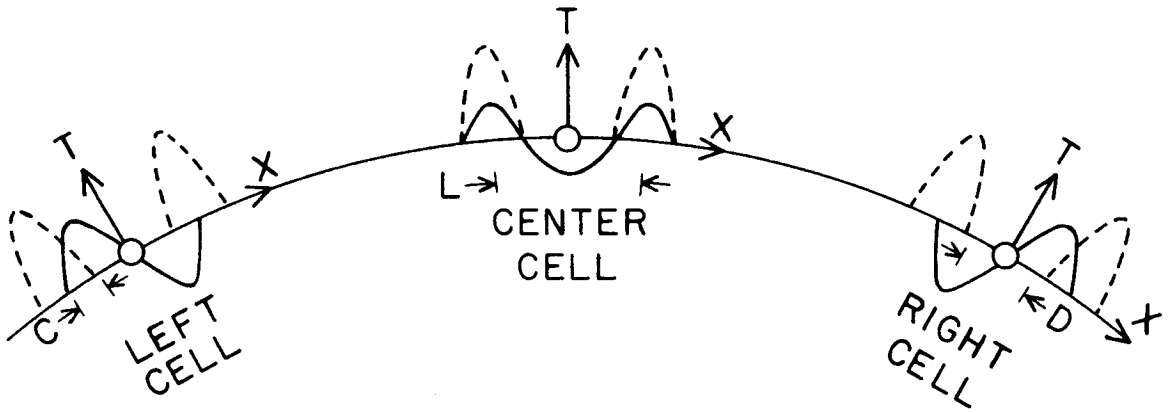

(a)

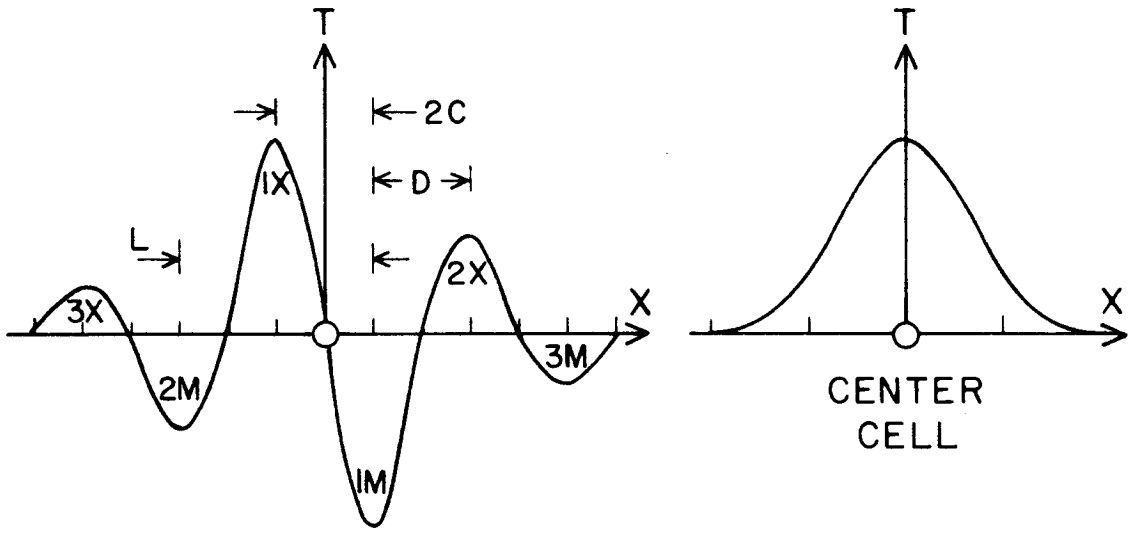

(b)

Figure 9. Schematic model of K-LC correlation.

center). The x-axis represents displacement along the solar surface, the vertical axis transmission on the plates. In the plates studied, the polarities were such that both the K network and receding line-of-sight velocities appeared as lighter than the average transmission. Thus a displacement of the left cell to the left (relative to the K plate) by an amount C, or the right cell to the right a similar distance, should produce a relative maximum, since then bright objects would coincide with bright objects. Conversely, a displacement by the left cell to the right, or the right cell to the left, would superimpose dark and light objects, and result in a relative minimum. Both of these effects could easily be seen with the eye when two such plates were superimposed, especially the transmission minimum, which produced a featureless flat grey appearance. At the center of the disc, where we assume that the motion is up at the cell center, downward at the edges, one would expect a relative maximum when the displacement is zero. With the eye it was extremely difficult to detect more than a faint hint that such a maximum might exist, demonstrating again that the vertical cell motion is either very small or covered up by the small scale oscillating field.*

These relative maxima and minima in the cross-correlation function are shown schematically in Figure 9(b), where the left sketch refers to the left cell, the right figure to the behavior at

---

* In this study we again tried to eliminate as much of the small scale noise as possible, by using Doppler plates taken 2 - 3 minutes apart, approximately half of the oscillation period; thus in a Doppler sum plate, the oscillatory field tends to "cancel itself out."

the disc center. (The right cell C-C function obviously is equal to that for the left cell, if we change x to -x.) In the left-hand sketch, a series of successive maxima (1X, 2X, 3X) and minima (1M, 2M, 3M) are shown. Whether all of these peaks appear depends on the regularity of the velocity cell and K network spacing. If we define the distance (in Figure 9(a)) between the velocity cell maximum and minimum as D, and the cell size as L, then the cross correlation curve in Figure 9(b, left) measures various distances which are combinations of D, L, and C = (L - D)/2. If all six of the drawn peaks exist, then 15 such combinations can be measured in a single C-C run, thus providing a wealth of statistical information from a relatively small number of tracings. (Compare this to a typical A-C run, which gives but one measurement of L, and one of the FWHM, a quantity roughly equal to D.)

Such cross-correlations were measured on three pairs of Ca (λ6103) and Ca II (λ3933) plates, as shown in Table 5. The quantity Δt refers to the time difference between the cell plate and the K plate, ΔT to the time difference at the center of the disc between the two plates used in making Doppler sum, and L, R, and C to the number of tracings made on left, right, and center of disc cells.

An L (or R) tracing was made at 10 different radii each 0.2 inch wide (on the 3.3 inch diameter image), by masking out all of the annulus except a narrow sector of 40 degrees on the left (right) side of the image. The open sector was centered on the x axis; i.e., along the direction of scan, which was

Table 5

Case	Date	Δt	ΔT	L	R	C
1	6-11-62	102^m	165^s	10	6	4
2	6-22-62	49^m	154^s	6	10	4
3	6-23-62	48^m	129^s	9	10	4

perpendicular to the limb of the sun. For each L and R tracing, the locations of all the maxima and minima were recorded (as positions of the micrometer on the correlation machine). These data, plus the value of μ, were fed into a 7090 computer, which corrected for geometrical foreshortening, transformed the micrometer readings into kilometers on the sun, combined all the tracings, least-square analyzed the data, and produced the results shown in Table 6. A typical cross-correlation tracing for a "right" cell is shown in Figure 10(a). Note the similarity between this actual tracing and the schematic model of Figure 9(b, left), with $x = 0$ occurring between 1M and 1X.

In Table 6 the numbers N_L, N_D, and N_C refer to the number of measurements of L, D, and C. The quoted values of L, D, and C are the averaged results, all points more than three standard deviations from the mean having been discarded. The error refers to the standard deviation in the mean.

Several interesting points should be noted. Firstly, as expected, the value of L agrees quite well with that found in Section A for the distance to the subsidiary maximum in the large

Figure 10. a) Actual C-C tracing across a "right" cell. Note the close similarity to the schematic model in Figure 9(b, left). However, the polarities are reversed, since the model is of a "left" cell. Plates taken 6/11/62.

b) Actual tracings across a "center" cell on the same plates as in a). In this case too, the agreement with the model in Figure 9(b, right) is very good.

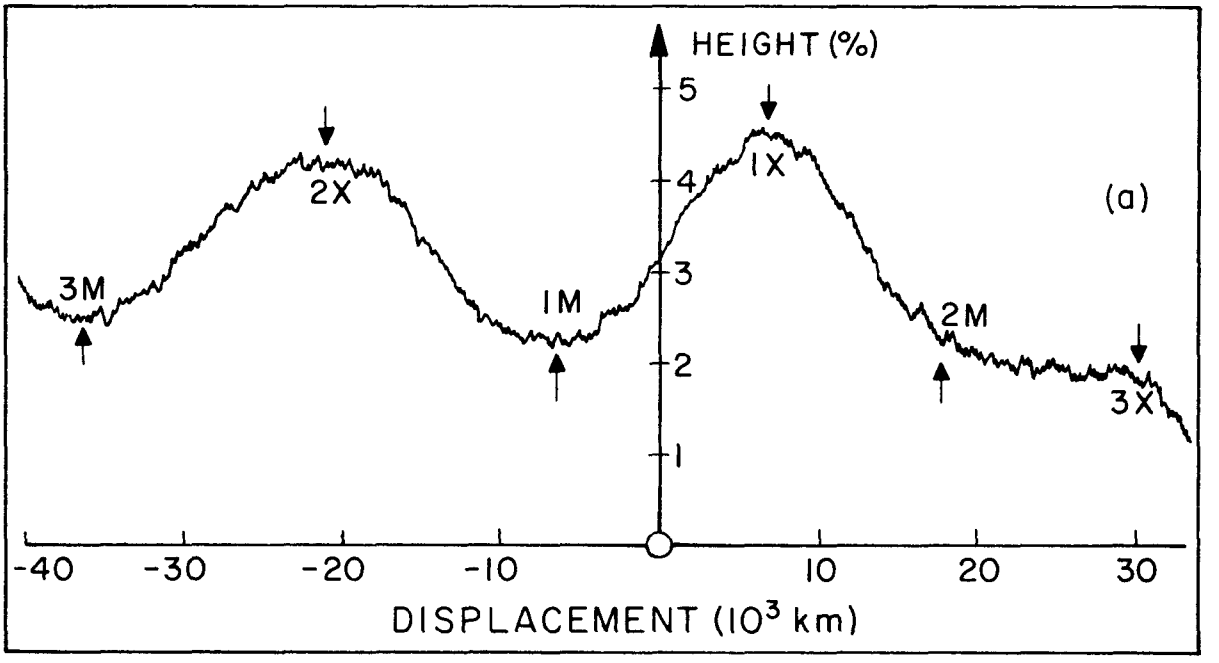

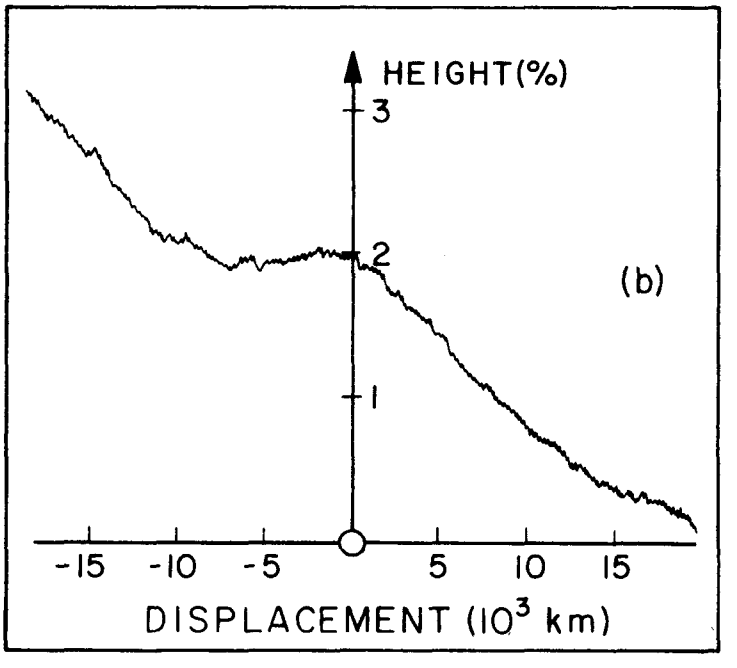

Figure 10. Caption on facing page.

Table 6

Case	L	N_L	D	N_D	C	N_C
1	30.4 ± 0.7	57	15.9 ± 0.9	29	7.4 ± .3	31
2	29.0 ± 1.0	39	16.2 ± 1.1	20	6.6 ± .4	28
3	31.8 ± 1.1	46	17.3 ± 1.1	28	7.3 ± .3	29
TOTAL	30.8 ± 0.6	142	16.5 ± 0.6	77	7.1 ± .2	88

(Note: L, D, and C are in thousands of kilometers)

cell A-C curves, and with the spacing of the K network to be discussed in Section C which follows. Secondly, D agrees very well with the FWHM measurements of Section A. Thirdly, if the horizontal velocity field has the previously assumed sinusoidal form, we would expect that $L = 2D = 4C$.* From Table 6 we find that D/L is equal to .53, indicating that our crude model contains some semblance of reality. In addition, the cross-correlation tracings confirmed in every case the right - left odd parity of maxima and minima formation seen by the eye, described earlier. Fourthly, what about the regularity of the cell structure? On the 51 R-L tracings which showed 102 first maxima and minima, there were 77 second and 37 third maxima and minima. No peaks beyond the third order were recorded, although a few existed. These figures suggest that some local order exists in the cell structure, extending perhaps over two or three cell diameters. But the reader is warned to realize that a third order

* This is true for a rectangular cell plan form. For a circular plan form, the ratio D/L is not .50, but .57.

maximum is not synonymous with a correlation extending across three cells, but only extending to the first neighboring cell. Referring back to Figure 9(b), one can see that the distance to the first peaks is C, to the second is C + D; both of these are less than the cell spacing L. Only the third order peak involves a displacement which is slightly larger than L, and thus clearly extends into the neighboring cell. Further evidence for the lack of a precise regularity in the spacing and/or size of the cell system is the spread in L and D sizes, shown in Figure 11.

So far we have said nothing about the very important maximum whose existence was predicted by our model (Figure 9), for correlations at the center of the disc. The significance of such a maximum, as has been pointed out above, is that it would confirm the existence of downward vertical motions at the cell boundaries and/or upward motions at the cell center.

On each of the three pairs of plates, four scans were made at the center of the disc. A typical tracing is shown in Figure 10(b). Note that the central peak occurs at $x = 0$, in agreement with the schematic model (Figure 9(b, right)). The fields of view consisted of discs 0.2, 0.3, 0.4, and 0.5 inches in radius. Each of these twelve C-C runs demonstrated a maximum, just as predicted. However the height of the maximum, expressed as a percentage change in the transmission through the two plates, ranged between 0.08 percent and 0.6 percent, making it quite obvious why these maxima were difficult to see by eye (It was even hard for the photomultiplier tube!). Indeed, they were so small that one would normally

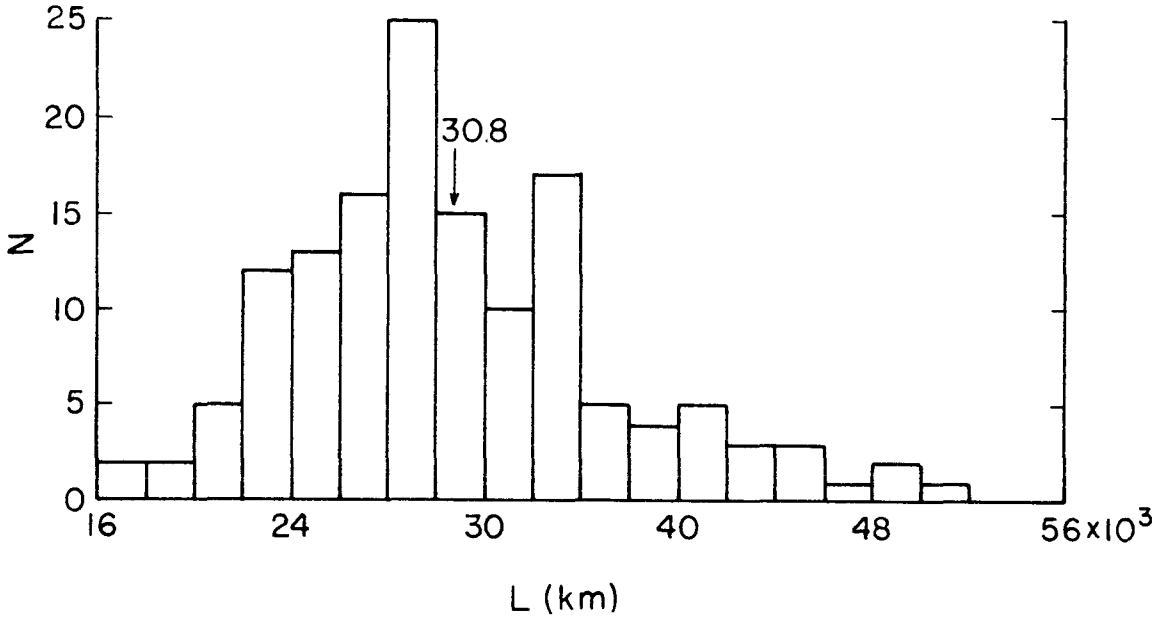

Fig. 11(a). Distribution of L sizes measured in K-LC correlations.

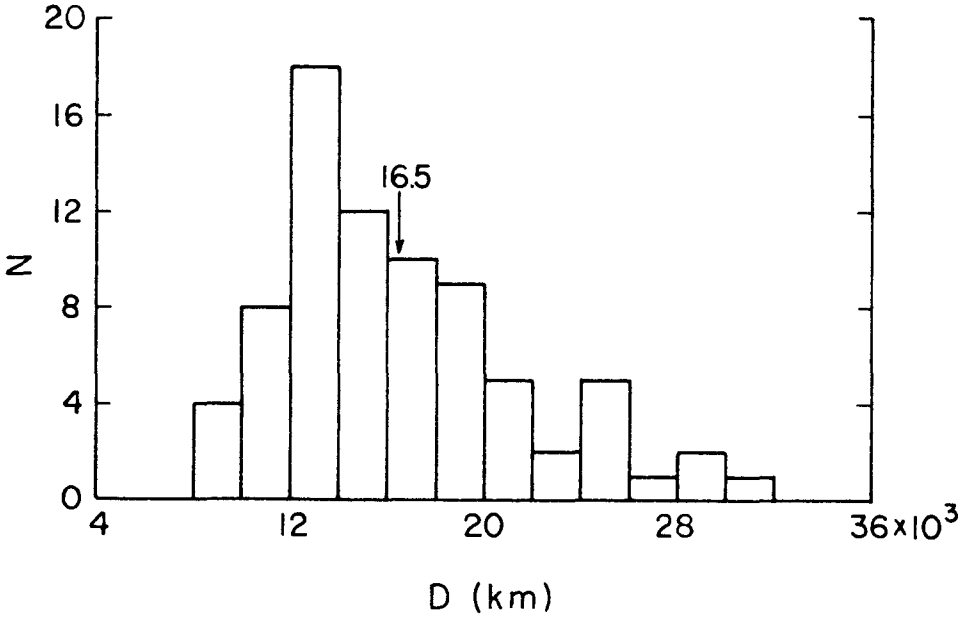

Fig. 11(b). Distribution of D sizes measured in K-LC correlations.

tend to discard them as being due to random noise fluctuations, except for one very important property which all but one of these maxima possessed: They occurred not more than 0.1 mm* from the position in which the two plates were in perfect registration; i.e., at $x = 0$, exactly as predicted.

In order that we could make the above assertion, it was first necessary to determine what micrometer setting corresponded to $x = 0$. To do this, we assumed what we wished to prove, and then checked for consistency. The average micrometer setting for the 12 center-of-disc maxima was calculated and defined to be x_o. Then the distance (in km on the sun) was measured from x_o to each of the R-L first maxima and minima. Referring to Figure 9, the distances to all of the "left-handed" peaks (i.e., displacements to the left; namely, to 1X for a "left" cell, to 1M for a "right" cell) were averaged together; similarly for all the "right-handed" peaks. If x_o is a good zero, then the two distances should be equal. The two calculated average distances were 7.78×10^3 km and 7.75×10^3 km. That these numbers agree to 30 km is obviously fortuitous; that they agree within one or two thousand kilometers is important, and seems to prove that the center-of-disc maxima at x_o are not merely spurious fluctuations, but are really telling us that small vertical velocities do indeed exist in the large cells. This would confirm the shaky evidence seen in the microphotometer

---

* A distance of 0.1 mm on the 8.38 cm image corresponds to about 1700 km on the sun.

tracings described in Section A.

Finally, we must determine how strong the correlation is between the large cells and the Ca II network. In terms of the A-C functions $(AC)_1$ and $(AC)_2$ of two transmission functions T_1 and T_2, we define the normalized C-C function F as

$$F = \frac{H_{cc}(K - LC)}{\left[H_{ac}(K) \times H_{ac}(LC)\right]^{1/2}} \qquad (20)$$

where T_1 refers to the K transmission function and T_2 to the LC function. We have computed F for each of the 51 C-C runs, and plotted as circles in Figure 12, the average F calculated by combining the results of all three cases, at each radius. Points which have $R > 1.0$ inch ($\theta > 37^\circ$) should probably be disregarded, since the behavior becomes irregular beyond this point. These results will now be compared with the simple schematic model pictured previously in Figure 9.

For the large cells, we adopt the "hexagonal-cell" velocity field described in Section A, while for the Ca II emission, we use the symmetric transmission function $T(\rho) = \sin \pi(2\rho/R + 1)$ for $.5 < \rho/R < 1$, and $T(\rho) = 0$ elsewhere. This latter function is an annular transmission region which has a maximum at $\rho_o = .75R$. In making the cross correlation, we changed the scale so that ρ_o, not R, would represent one-half the cell size L. This then necessitated scaling down the size of the hexagonal velocity pattern, so that the sine function would go to zero at the new cell boundary ρ_o. A series of such C-C functions was computed

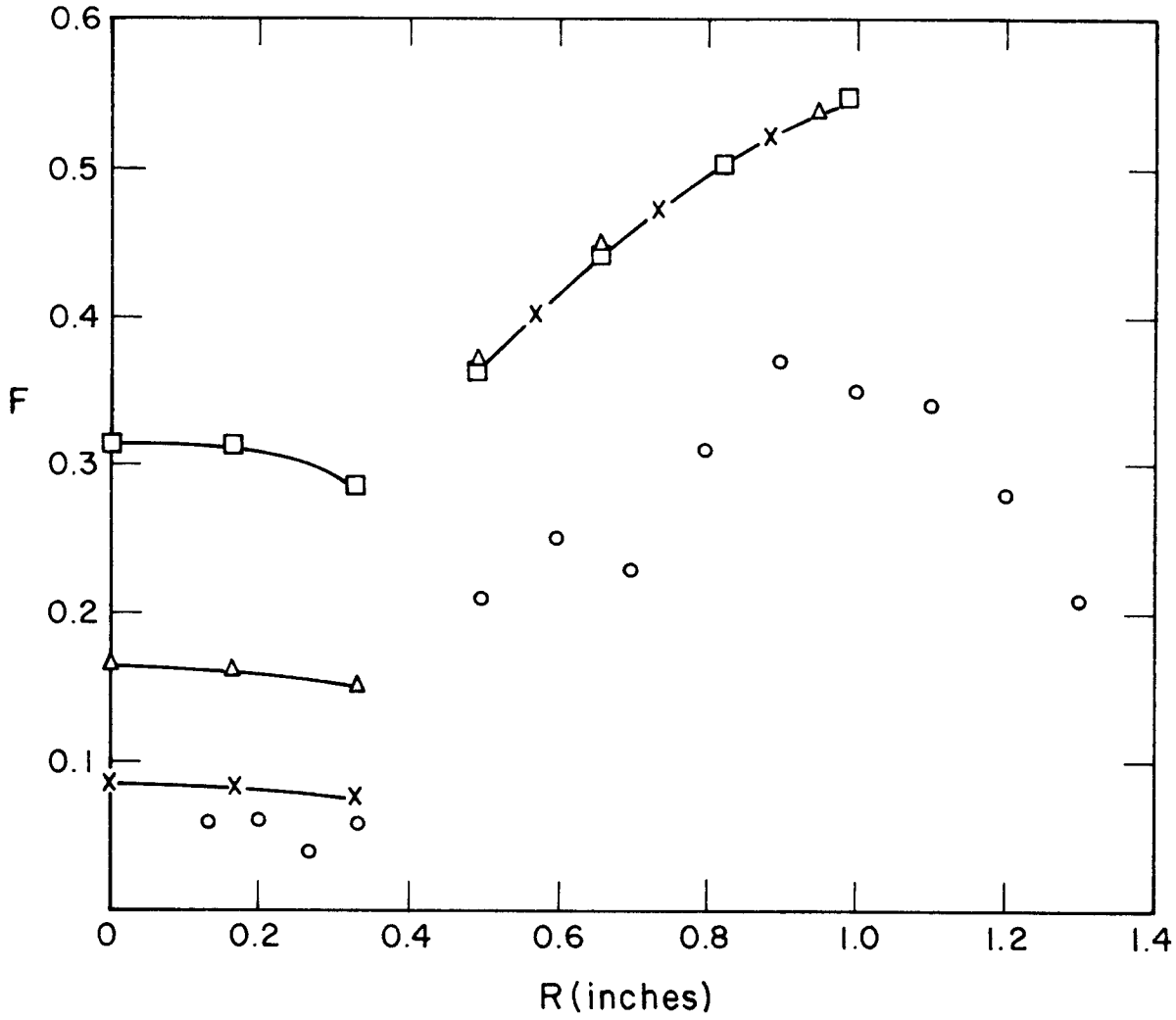

Figure 12. Cross-correlation (F) vs radius (R) for K-LC correlation. Circles are measured values; solid lines represent theoretical prediction of the correlation. Theoretical ratio of vertical to horizontal velocity in cells is 0.05 (X), 0.10 (△), and 0.20 (□).

by the 7090, using three values for the ratio (R_v) of vertical to horizontal velocity in the large cell; namely, 0.05, 0.1, and 0.2. The theoretical values of F (equation 20) were then computed. In doing this, an attempt was made to compensate for the small-scale noise always present in the large cell A-C curves. For the three plates used for this study, the noise ratio H_o/H_L (ref. Section A) was about 0.20;* the resulting change in F was computed. In Figure 11 we see the theoretical curves of F for the three values of R_v. In the region where R-L runs were made ($R > 0.5$ inch), the three theoretical curves virtually coincide, and increase to the right as $\sin^2\theta$. The measured values of F range from 50 percent of the theoretical value at $R = 0.5$, to 70 percent at $R = 1.0$. In the center-of-disc region ($R < 0.4$ inch), the theoretical curves are very sensitive to the ratio R_v. If we assume that here the measured values are also about 60 percent or so of the theoretical, then a value of R_v between 0.05 and 0.1 seems to fit the data best; that is, the vertical velocity in the cells is between 5 and 10 percent of the horizontal component. It will be recalled that the microphotometer tracings in Section A implied that the stronger vertical velocities might occasionally reach 50 percent of the horizontal component. If both of these sets of numbers can be believed, then we conclude that vertical velocities do indeed exist in the large cells. However, these velocities are in general

---

* H_o refers to the A-C height at the center of the disc due to granulation, while H_L is the height at the limb, due primarily to large-scale fields.

very small relative to the horizontal motion, a fact already confirmed by visual inspection of large cell plates.

Of course there is the very real danger that we may be trying to extract more information out of our large cell model than is justifiable. The strongest evidence that the model is at least qualitatively correct was given by the correct predictions concerning (1) the polarities of the maxima and minima on the R-L runs, and (2) the position of the maximum for the center-of-disc scans. To these two successes we can now add the fact that the shape of the theoretical F vs R dependence agrees very well with that of the experimental data, in Figure 12, even though the magnitude is too high. But one would expect the magnitude to be different, even if the model were perfect, because certainly the K-LC correlation isn't completely one-to-one. If the correlation is truly about 60 percent, as the model indicates, then these results very strongly corroborate those found with the cell-by-cell counting technique discussed in the first part of this section; namely, that the boundaries of the large cells generally coincide with the Ca II emission network.

Let us now turn to a more detailed study of the Ca II network itself.

C. Spatial Periodicity of the Ca II Network

The existence of a coarse polygonal network pattern in spectroheliograms taken in the K_{232} core of Ca II was first reported by Deslandres (25) in 1899, and has been discussed by

numerous authors since that time. We have already presented a photo of this network in Figure 2. Close inspection of this network structure quickly reveals two features: (a) There is a large spread in the sizes of the polygon "diameters" or "meshwidths," which, for example, Rogerson (31) measured as 25000 to 70000 km. (b) To speak of a "meshwidth" at all is somewhat dangerous since most of the polygons are quite irregular in shape, and moreover are usually fragmented, with one or more sides missing.

Yet there is little doubt that there exists some sort of "characteristic" size to the structure, with at least a quasi-periodic spacing over small distances. If this were not true, it would have been impossible to obtain the high degree of spatial correlation between Ca II emission and the large-scale velocity cells, discussed in the previous section. Nor could one otherwise explain the very strong moiré effect when one member of a Ca II right-left pair is moved across its mirror image.

Using auto-correlation analysis of right-left pairs, two measurements were made of the network pattern. In the first of these, seven 17 cm images, taken at various positions within 0.2A of the λ3933 line-center during the summer of 1961, were reduced in size to a diameter of 3.70 inches so that the entire solar disc would fit into the 3.75 inch opening of the correlation machine plate holders. Using the circular scan drive, a series of auto-correlations was obtained for ten successive

annular regions, each 0.2 inch wide. That is, all of these tracings were made parallel to the limb, at various radii. For the second study, six 17 cm 1962 plates were treated by the foreshortening-removal apparatus. Then two linear runs were made on each, at the center of the disc, one in a roughly N-S heliographic direction, the other E-W.

Results for the first case are shown in Figure 13. In 13(a) the FWHM (interpreted as the average width of the network emission - the thickness of the polygon sides) for all 61 tracings are plotted as a function of annulus radius, while in 13(b) is shown the distance L (the "meshwidth") to the first subsidiary maximum for 102 measurements. Superimposed on the data in each figure is a horizontal dashed line representing the mean value, and a cubic least squares fit giving the radial dependence of the data.

The apparent minimum in the FWHM data at about r = 1.0 inch ($\theta \approx 33^{\circ}$) should not be taken seriously. One would expect that as one approached the center of the disc the FWHM would steadily decrease, since more and more of the fine mottling would be resolved. The slight rise in FWHM at small radius is probably due to the smearing effect of the circular scan: If r_1 and r_2 are the inner and outer radii of the annulus,* the arc lengths $s_1 = r_1(\Delta\phi)$ and $s_2 = r_2(\Delta\phi)$ will be very different if r_1 and r_2 are small. Thus, for r = .3, a solar feature of length s will move in and out of

---

* The quantity r plotted in Figure 13 is the average of r_1 and r_2.

Figure 13. Results from auto-correlations of the K network. a) FWHM vs radius. b) L vs radius. Dashed lines are mean values averaged over all radii. Solid lines are least-squares fits to the data. The radius values refer to a solar image of 3.70 inch diameter.

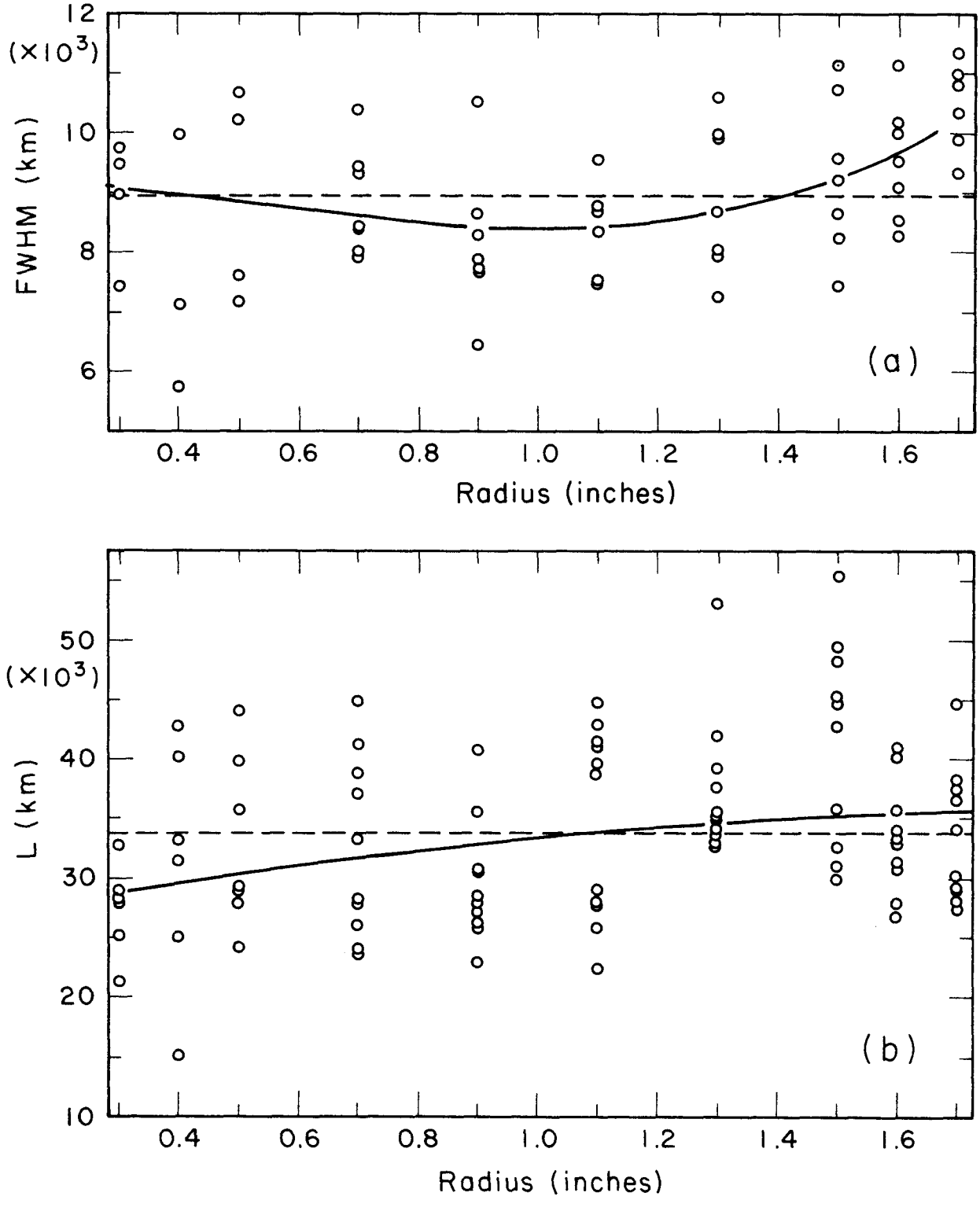

Figure 13. Caption on facing page.

register about twice as fast if it is near r_2 than if it is close to r_1. Alternatively, the minimum may be due merely to the poor statistics; namely, the small number of data points and the large spread in their values.

The average FWHM for those cases which had the exit slit centered on K_{2v} is 6000 - 7000 km; for K_3 plates the average is 9000 - 10000 km. The difference is due to the relative amounts of fine mottling mixed with the coarse mottle-network emission. The K_3 values are probably closer to the true network emission widths, since they are freer of the fine structure. Recalling from the auto-correlation analysis (Part III(C)) that for a symmetric transmission function, the FWHM is roughly 80 percent of the true width, we conclude that the average thickness of a polygonal side is approximately 11000 - 13000 km.

In Figure 13(b) the increase in L with increasing radius is probably due to the disappearance or overlapping of the finer network features near the limb, so that the apparent meshwidth increases.

Consider next the runs made at the center of the disc with the foreshortening-removed plates. Here the fine mottling is relatively important; thus the average FWHM is only 7.7×10^3 km. For the average L we obtain 30×10^3 km, somewhat less than the 34×10^3 km measured in the circular scans.

Since secondary maxima in auto-correlation functions are interpreted as evidence for a periodicity in the observed phenomenon,

the above results would seem to imply the existence of a regular network pattern in Ca II emission with a cell size or meshwidth L = 30000 - 35000 km. Thus a composite curve in which one averages together many individual auto-correlations should show a strong maximum at a distance L. Such a composite curve was made from the circular scan data, and completely failed to corroborate the maximum seen in each of the individual cases. Apparently the spread in the individual L's was such that minima on some curves coincided with maxima on others, the net effect being to "wash out" the hoped-for maximum at 30000 - 35000 km.

It is therefore necessary to consider in some detail the distribution of L sizes, and to investigate whether the previously asserted "meshwidth" is indeed a real quantity, or merely the product of spurious effects. In the following discussion we shall analyze together the four different measurements of cell size L which we have obtained: 1. The circular scan data of this section. 2. The linear scan data of this section. 3. The large cell data (perpendicular to the limb) of Part IV(A). 4. The K-LC data of Part IV(B). (These four types of L will be labeled L1, L2, L3, and L4 in what follows). We have included L3 and L4 in this discussion since we have shown in Part IV(B) that the velocity cells and the Ca II network are essentially in one-to-one spatial correspondence.

Already in Figure 6 and Figure 10 we had drawn histograms for L3 and L4. Two more histograms, for L1 and L2, are now shown in Figure 14, and a final composite histogram, combining together all 399 measurements of L, in Figure 15(a). A typical auto-correlation

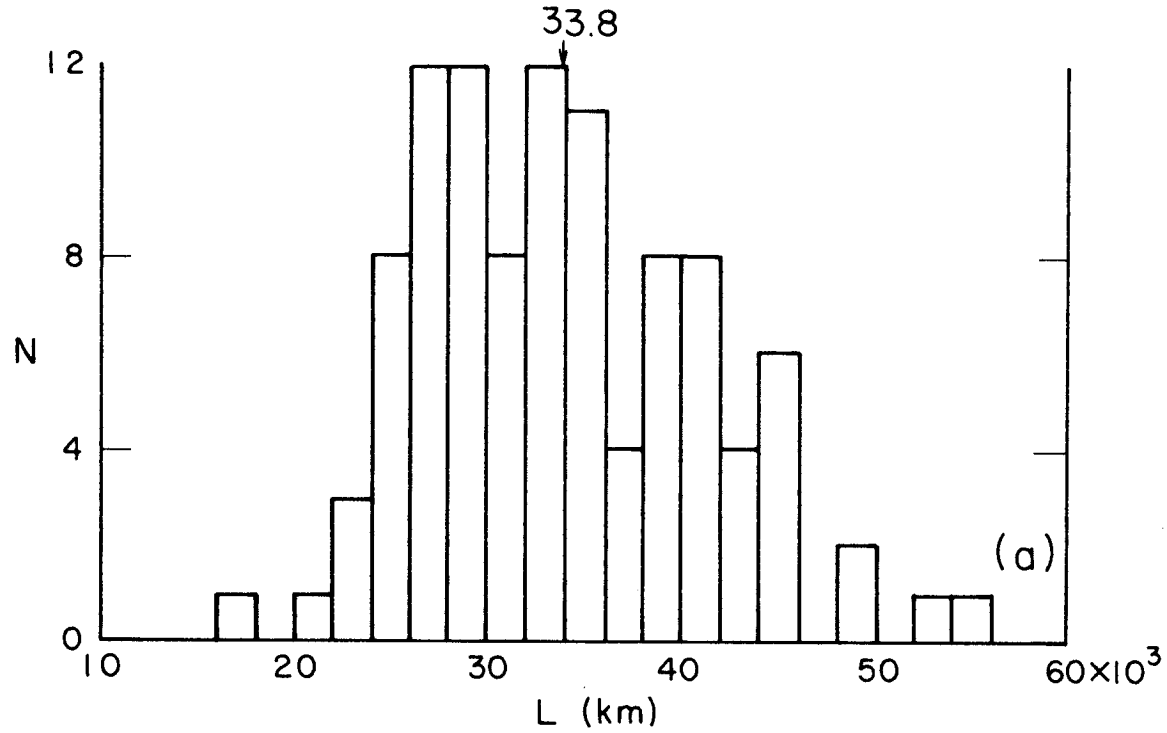

Fig. 14(a). Distribution of L sizes for circular scans of the K network.

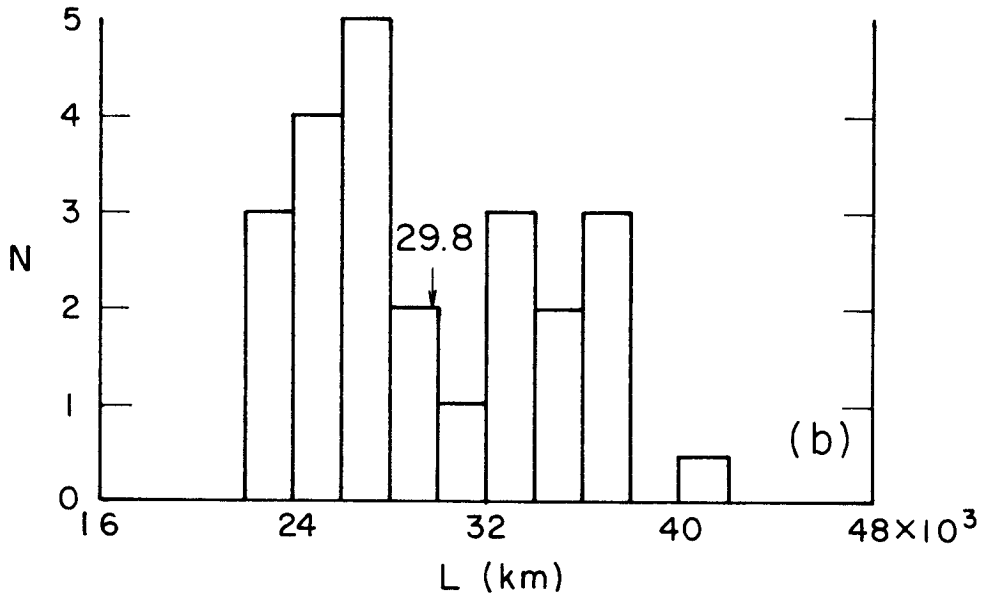

Fig. 14(b). Distribution of L sizes for linear scans of the K network.

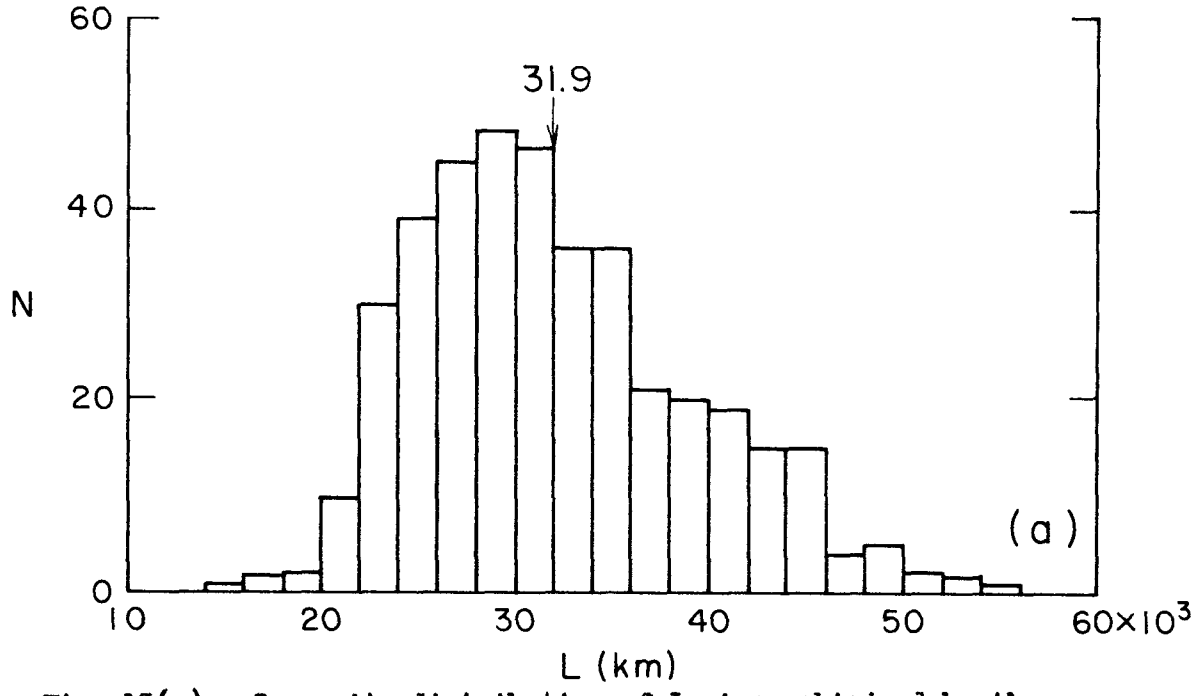

Fig. 15(a). Composite distribution of L sizes obtained by the four methods.

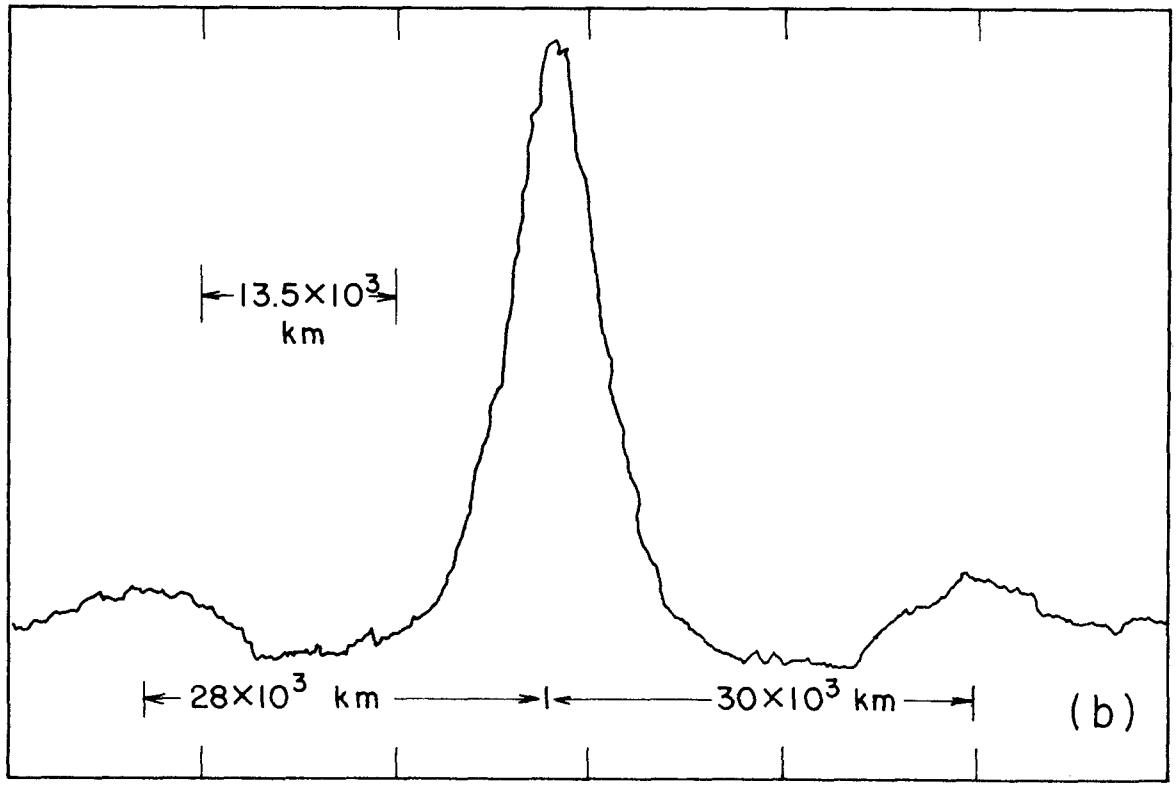

Fig. 15(b). Typical A-C curve of K network showing secondary maxima.

tracing of the K network is shown in Figure 15(b). Of all the histograms, only the composite one shows the expected "normal" distribution of sizes, with a definite strong peak in the distribution. This is probably due to the wide spread in L sizes, so that the individual cases do not contain enough data points to achieve "good" statistics. In particular note that Figure 14(a) has a double peak, with a dip between, so that it is not surprising that the composite auto-correlation curve failed to show a secondary maximum.

If the L data is valid, then the results of Figure 15(a) verify that there exists a local periodicity, but that this periodicity varies greatly in size from time to time, from area to area, and even depends on scanning direction. That the scanning direction is important can be outlined in a very schematic fashion as follows: Consider the case of a perfectly regular square lattice, as illustrated in Figure 16. In the scanning direction AB a subsidiary maximum occurs whenever the displacement X is a multiple of the unit cell size L. For the diagonal direction AC, peaks occur for displacements $\sqrt{2}L$, $2\sqrt{2}L$, etc. And for scans along AD, major peaks occur at 5L, 10L, etc.; and in addition minor peaks are seen at 5/4 L, 10/4 L, 15/4 L, and at 5/3 L, 10/3 L, whenever either the vertical, or horizontal lines reinforce. Since the actual lattice on the sun is neither a regular polygonal structure, nor perfectly repetitive, one might expect even wider variations in subsidiary maxima than in the idealized

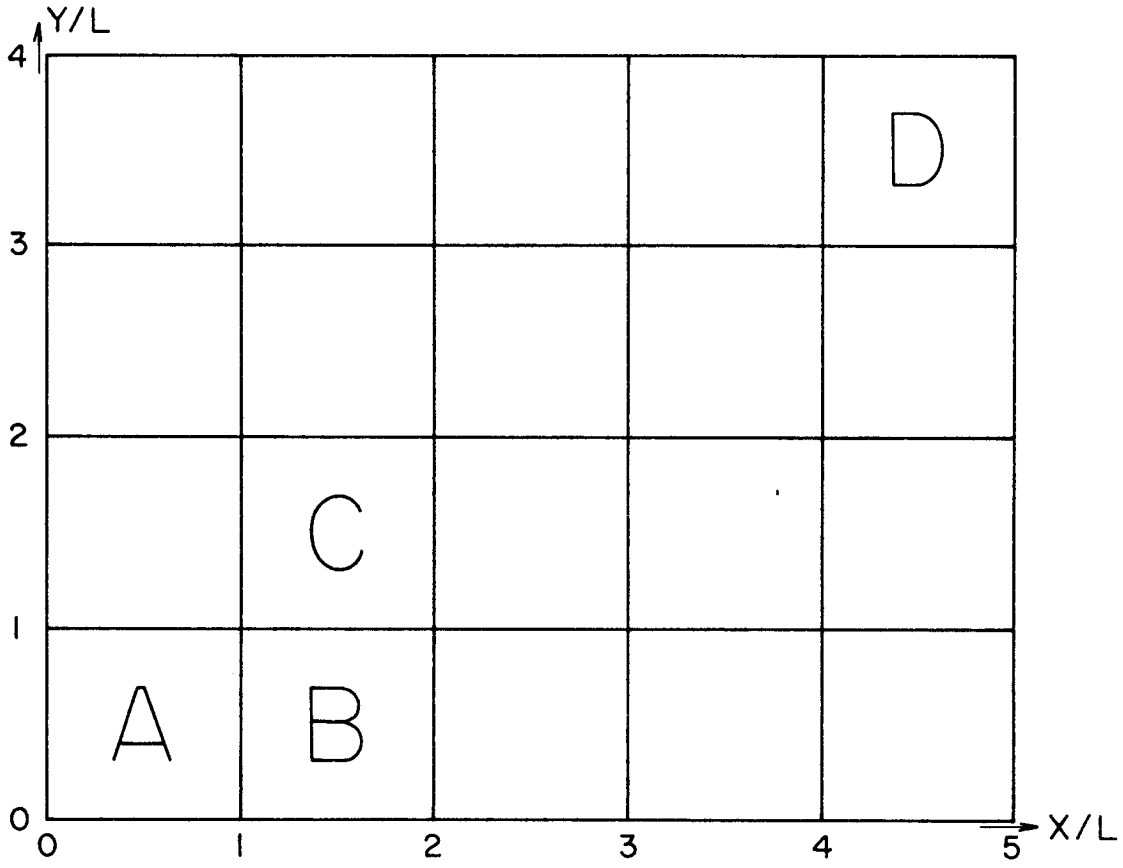

Figure 16. Illustrating the importance of scanning direction on measured cell size. In the direction AB, secondary maxima occur at displacements L, 2L, 3L, etc. Along the diagonal AC, they occur at $\sqrt{2}L$, $2\sqrt{2}L$, $3\sqrt{2}L$, etc. But along AD, major peaks occur at 5L, 10L, 15L, etc., and minor peaks at 5/4L, 10/4L, 15/4L and 5/3L, 10/3L, whenever either the vertical or horizontal lines reinforce.

example above, due to geometry alone. This was actually observed in the study of L2, where two runs were made across the same field of view, but in perpendicular directions. The average of the smaller L's of each pair is 25.8×10^3 km; the average of the larger L's is 33.9×10^3 km.

But we have still not answered the question of the validity of interpreting the subsidiary maximum as reflecting a real periodicity on the sun. By definition, an auto-correlation function must be symmetric about the origin, i.e., any subsidiary maxima should occur in pairs, which we shall call "two-sided." Furthermore, all auto-correlation functions should show this behavior, if a persistent network exists on the sun. If the true network is strongly periodic, one might expect to find not only one secondary maximum, but perhaps several more. In Table 7 are summarized the results of the measurements of the first and second subsidiary maxima for cases L1, L2, and L3.

Table 7

Case	Number of First Maxima			Number of Second Maxima			Ave. No. of Cells
	2-sided	1-sided	0-sided	2-sided	1-sided	0-sided	
L1	44	14	3	22	15	24	130 - 170
L2	12	0	0	2	0	10	230 - 260
L3	59	13	6	7	10	61	70 - 90

First consider the number of first maxima. Only case L2, which had the "best" statistics, namely a large rectangular field of view and many more cells visible than in L1 and L3, exhibited the ideal two-sided pattern for all runs. Furthermore, if one refers again to the histograms of L sizes, it will be seen that the L2 case also had a much smaller spread in sizes than did L1 or L3. In L1 and L3, annular regions were used, with fewer cells, and one narrow dimension usually only 3 - 6 cell diameters wide. Only 70 - 80 percent of these latter cases exhibit the symmetric pattern, implying that end effects due to the finite field of view may be affecting the results. This suspicion is increased when we look at the second maxima data. The L2 case implies that the periodicity is not too strong, since only 2 runs exhibited a second maximum. However both of these were the proper two-sided type. Both L1 and L3 showed considerably more second maxima, but almost as many of these were one-sided as two-sided, and thus must be viewed with suspicion.* Indeed, case L1 also showed a number of 3rd, 4th, and 5th maxima, and even one run with a 7th order maximum. But these higher-order maxima look very similar to small peaks on "noise" runs; i.e., cross-correlations of two unrelated Ca II plates taken some days apart.

---

* It should be noted, however, that despite the possibility that these results may contain spurious effects, the average distance from 83 measurements of the second maximum is 57×10^3 km, very close to twice that obtained from the first maximum. The spread in sizes is again large, ranging from 32×10^3 to 90×10^3 km.

To summarize the above discussion, we conclude that on the sun there exists a relatively "weak" local ordering of the emission structure in Ca II plates. It exists because of the high percentage of two-sided first maxima seen on auto-correlation curves, because of the moiré effect and K-LC correlation mentioned at the beginning of this section, and because of the excellent agreement among the average sizes $\bar{L}$ found by the four methods L1, L2, L3, and L4, as discussed in the next paragraph. It is weak, firstly because of the small number of tracings which show a symmetric second subsidiary maximum, secondly because of the large spread found in individual L sizes, and thirdly because the height of the first subsidiary maximum is usually only one to five percent that of the central maximum, a fact not mentioned previously.

In conclusion, let us calculate the grand mean of all the $\bar{L}$ measurements, in which we weight each value of $\bar{L}$ by the square of $1/\sigma_m$, where σ_m is the standard deviation in the mean. This final value for the characteristic cell diameter, or network meshwidth, is $(31.9 \pm 1.4) \times 10^3$ km, as shown in Table 8.

D. Lifetime of the Ca II Network

Having established in Section B above that the Ca II network and the large cells are spatially related in essentially a one-to-one correspondence, it follows that the lifetimes of these two phenomena must also be quite similar. To measure directly the cell lifetime is extremely difficult, since the cells virtually disappear at the center of the disc, and thus can be observed only for a

Table 8

Case	$\bar{L}(10^3$ km)	$\sigma_{\bar{L}}(10^3$ km)	No. of Measurements
L1	33.8	0.72	102
L2	29.8	1.07	24
L3	32.5	0.65	132
L4	30.8	0.57	141
Weighted Grand Mean	31.9	1.38	399

relatively short time and only near the limb. Geometrical foreshortening is severe in the regions where the cells are visible, and cannot be adequately removed by the foreshortening-removal apparatus discussed in Part III.

Fortunately the Ca II emission network is visible over the entire disc, so that individual elements can be followed for over a week, if their lifetimes are that long. As mentioned in Part II, using the foreshortening-removal apparatus would permit almost distortionless viewing of a given element for just under five days; that is, for about 9.6 cm. along the equator of the 17 cm. image.

The lifetime of the bright Ca II flocculi (also called "coarse mottling" or "large chromospheric granules" by different authors) has been measured by Macris (4, 5), who followed visually over 150 individual flocculi and recorded the percentage which remained as a function of time. In the present study, cross-correlation functions were employed to measure the Ca II network lifetime. Considerable

ambiguity exists between the terms "flocculi" and "network," so it is not at all certain that Macris and the present work have measured lifetimes of different phenomena; indeed we are more inclined to believe that there is more similarity than difference between the phenomena studied in the two cases. De Jager (26) has pointed out that the "fine mottles" cluster together to form the "coarse mottles" which in turn are often arranged in a "coarse network," making it clear that there are no sharp lines of demarcation among these groupings. Probably it would be more accurate to say that in the present work we have measured an "average" lifetime associated with both flocculi and network emission, since the correlation machine responds to all intensity fluctuations in the field of view.

A total of 17 plates in four sets was analyzed in this study. Table 9 lists the number of plates in each set, number of correlations, inclusive dates of observation, image size, surface area on sun in the field of view, number of cells in the field of view, and time interval between first and last plate of the set. The number of cells in the field of view was estimated as follows: On these plates 1 cm = 68×10^3 km $\approx$ 2 cell diameters (ref. Section C), thus 1 $cm^2 \approx 4$ cells. Since the Ca II network shows up almost equally well in K_{2v}, K_{2r}, and K_3, spectroheliograms taken at various wave lengths within $\Delta\lambda \approx 0.2$A of the line center were analyzed together. All the plates were processed in the foreshortening-removal apparatus before correlations were made. In addition, all "larger-than-network-size" emission regions and plages were masked out, so that

Table 9

Set	No. of Plates	No. of Correlations	Dates (1962)	Image Size	Area on Sun (10^{10} km^2)	No. of Cells	Maximum Δt
1	3	3	8/4-8/6	17cm	10.7	92	$48^h\ 54^m$
2	8	17	8/21-8/23	8.4cm	9.3	80	$43^h\ 53^m$
3	4	12	8/31-9/1	8.4cm	6.2, 5.2*	53,45*	$24^h\ 6^m$
4	2	1	9/23	8.4cm	28.3	244	4^m

only quiet-sun phenomena remained in the field of view. Each pair of plates to be correlated was aligned by placing in register as many emission features as possible. Nearby sunspot regions (later masked out) proved very helpful in this regard.

In analogy to the fractional cross-correlation discussed in equation 20 of Section B, we define the normalized correlation $F(\Delta t)$ of two plates taken at times t_1 and t_2 as:

$$F(\Delta t) = \frac{H_{cc}(\Delta t)}{\left[H_{ac}(t_1) \times H_{ac}(t_2)\right]^{1/2}} \qquad (21)$$

where $\Delta t = t_1 - t_2$.

From the 17 plates, some 33 cross-correlations were made, at time intervals ranging between 4 minutes and 49 hours. All measurements were linear scans across the center of the disc ($\theta \leq 34^\circ$). The results are shown in Figure 17. In (a), F is plotted vs. Δt;

* Correlations of two separate areas on these plates were made.

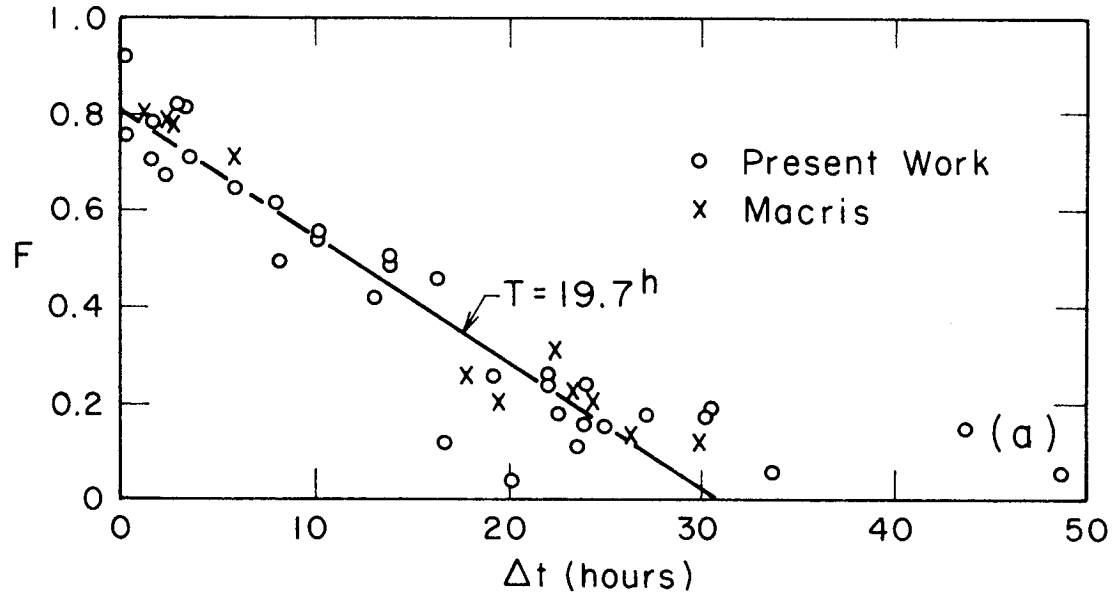

Fig. 17(a). Lifetime of the Ca II network (linear decay curve).

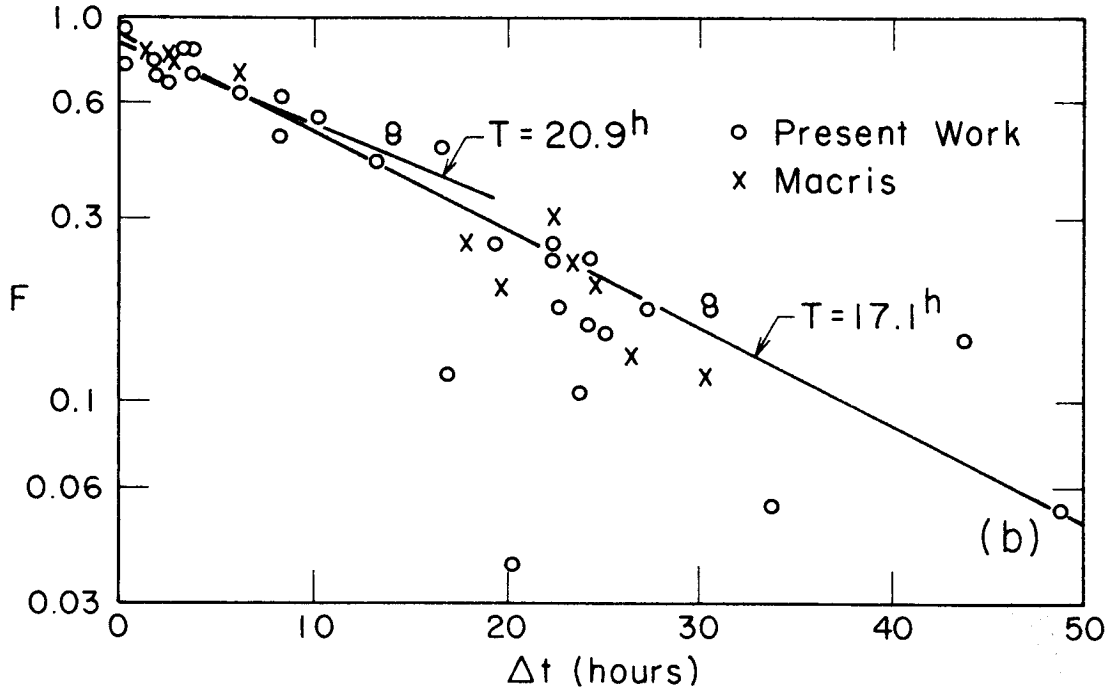

Fig. 17(b). Lifetime of the Ca II network (exponential decay curve).

in (b), $\log_{10} F$ vs. Δt. From these figures one could be equally well convinced that the correlation decays linearly or exponentially with time. Least-squares fits of the form $F = a + bt$ and $\log_{10} F = c + dt$, respectively, are shown in the figures. All data points are included in the figures, but only those points within 2.5 standard deviations were used in the least-squares analysis.

The lifetime T, defined as the length of time for the correlation to fall to e^{-1} of its initial value is then given by $T = a(1 - e)/be$ or $T = 1/d$ in the two cases. It can be seen from Figure 17 that the value of T depends on the maximum time interval (t_m) used in the analysis. In (b) two fits are shown, one with $t_m = 20.3^h$, the other with $t_m = 48.9^h$, while the straight line in (a) uses $t_m = 27.3^h$. Several points are worth noting:

1. Although any reasonable straight line fit in (a) would imply that F goes to zero in 30 - 35 hours, a small amount of correlation seems to persist much longer.

2. The large decrease in T as t_m increases is illustrated in Figure 18, using the logarithmic straight-line analysis. This is understandable when one realizes both that the foreshortening-removal is not perfect and that as t_m increases, the network slowly changes shape, even though individual flocculi may remain; these two effects both tend to decrease F for large t_m, thus lowering T. Also shown in Figure 18 are values of T from the linear straight-line fit; these are not so sensitive to t_m. It remains an open question what the "best" value of T is. We are more inclined to

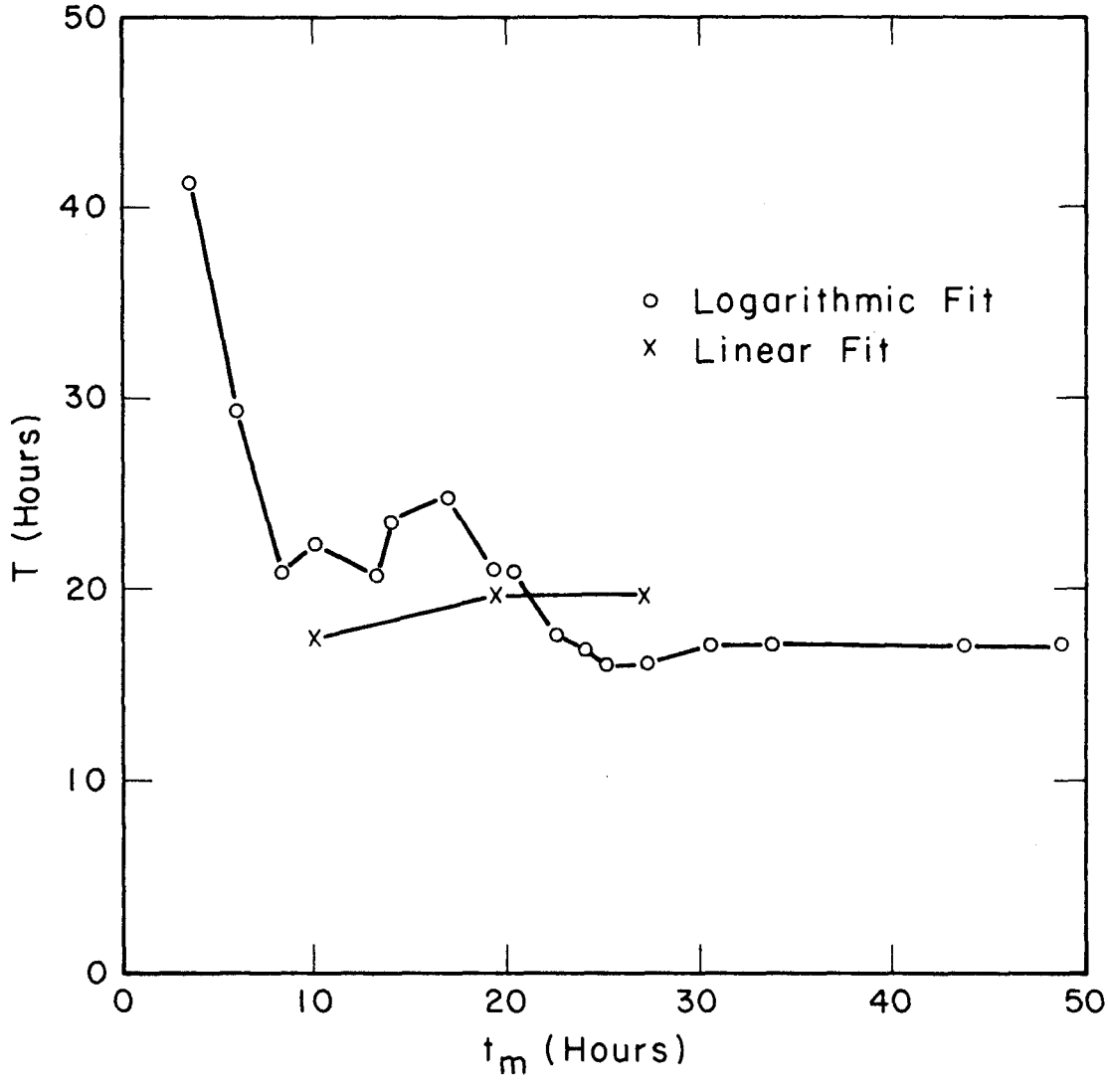

Figure 18. Dependence of the Ca II network lifetime (T) on the maximum time interval (t_m) used in the correlation analysis.

choose the value $T = 19^h - 21^h$ obtained from Figure 17(a) and the upper line of Figure 17(b), but if one chooses to include also the data with $t_m > 1^d$, one must assign a value $T \approx 17^h$.

3. The effect on the measured correlation due to fine mottling, photographic grain, small plate blemishes, etc., can be seen in Figure 17. One would expect from equation 1 that as $\Delta t \rightarrow 0$, F should go to unity. However, from the data analysis we find that the F axis intercepts are $F_o = a = c \approx 0.82$. As an illustration, even for two spectroheliograms taken only four minutes apart, a Δt negligibly short relative to the network lifetime, the average value of F was 0.84. That is, small-scale solar details, which add to the height of an auto-correlation function, do not contribute significantly to cross-correlations, either because they disappear or shift in position (due perhaps to shorter lifetimes, local velocity fields, or very often due to changes in the local "seeing"). Similarly, photographic grain and tiny blemishes are impossible to mask out and also contribute more to auto-correlation heights than to cross-correlation heights.

To compare the present results with those of Macris (5), we assume that our F is equivalent to his percent of flocculi remaining after a time Δt. After multiplying his percent data by 0.82 so that the two methods agree for $\Delta t = 0$, we have plotted his data together with ours in Figure 17. The agreement is excellent, and forms the basis for our earlier assertion that despite the differences in method and in terminology, we are essentially measuring the same phenomenon as Macris.

E. Correlation Between Hα and Hβ Velocity Fields and the Ca II Network

Spectroheliograms taken far in the wings of the hydrogen lines, Hα, Hβ, and Hγ, show a dark network pattern very similar to that of the bright Ca II emission network. This phenomenon was first described by Deslandres (27), and has since been discussed in detail by de Jager (26, 28, 29) and others. For the following wavelength shifts in the three lines:

$$\Delta\lambda(H\alpha) = \pm 0.7A$$

$$\Delta\lambda(H\beta) = \pm 0.4A$$

$$\Delta\lambda(H\gamma) = \pm 0.2A$$

one finds that the network pattern is at a maximum, with a quiescent background. De Jager estimates the height of formation of these features to be about 1000 km above the photosphere. Another well-known characteristic of these spectroheliograms is that the contrast between the intensity of the network and that of the background is much greater on the red side of the line than for an equal displacement to the violet. This is clearly seen in Figure 19(a), a portion of a 17 cm photograph of Hβ with $\Delta\lambda = \pm 0.4A$. In addition, de Jager (28) found a persistent red shift in the network regions on such spectroheliograms, and later concluded that the "coarse mottles and the chromospheric network must be considered as a field of large scale descending motions" ((29), p. 80).

Figure 19. a) Spectroheliograms of same region of the sun illustrating the difference in contrast on red and violet wings of Hβ line. Top left, violet; top right, red. Plate of 9/2/62, $\Delta\lambda = 0.4A$.

b) Lower photo is a Doppler sum in Hα ($\Delta\lambda = 0.7A$) taken on 6/27/62. Brighter-than-average network is descending. Small dark rising spots may be spicules.

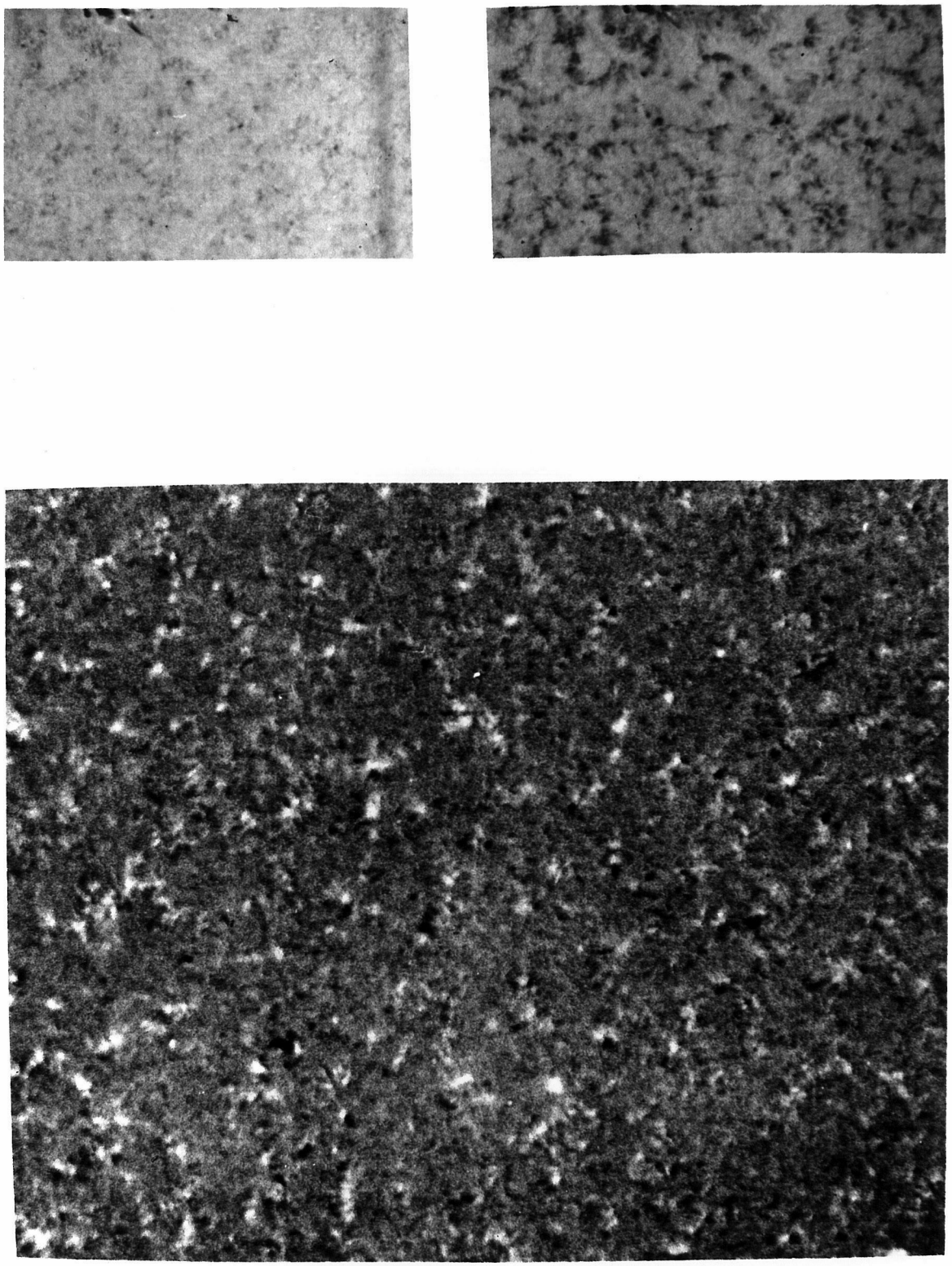

Figure 19

In this section we shall present results obtained from Doppler plates taken in Hα and Hβ at the Δλ's listed above.* These corroborate the findings of the previous investigations. In addition, we shall show that the spatial position of the hydrogen network coincides with that of the Ca II emission.

Figure 19(b) shows a typical second-cancelled 17 cm Doppler sum spectroheliogram photographed at the center of the disc in Hα ($\Delta\lambda = \pm 0.7$A), while Figure 20 contains three similar photos in Hβ with $\Delta\lambda = \pm 0.40$A, ± 0.32A, ± 0.24A, from top to bottom. The polarity in these plates is such that light regions are receding, while dark areas are approaching. Immediately apparent in 19(b) and 20(a) is the brighter-than-average network superimposed on a rather featureless grey background. Upon closer inspection, a number of small dark spots can be seen mixed in with the predominantly light network. Also, particularly in 20(a), a few of the network cells appear to enclose dark (rising) regions. In 20(b) and especially in 20(c), as one goes higher into the chromosphere, the network, though still visible, becomes submerged in a granular background of small dark and light elements.

From microphotometer tracings made across selected regions where the network pattern was most pronounced, the following peak velocities relative to the background were measured (minus sign indicates receding line-of-sight velocity), as shown in Table 10.

---

* The Hγ plates were not of a high enough quality to warrant analysis.

Figure 20. Three Doppler sum photos of same region of sun taken in wings of Hβ. In top picture ($\Delta\lambda$ = 0.40A) descending network predominates. In center and lower photos, network becomes less clear, corresponding to higher elevations in the chromosphere ($\Delta\lambda$ = 0.32A, 0.24A; center and lower, respectively). Plates taken 9/2/62.

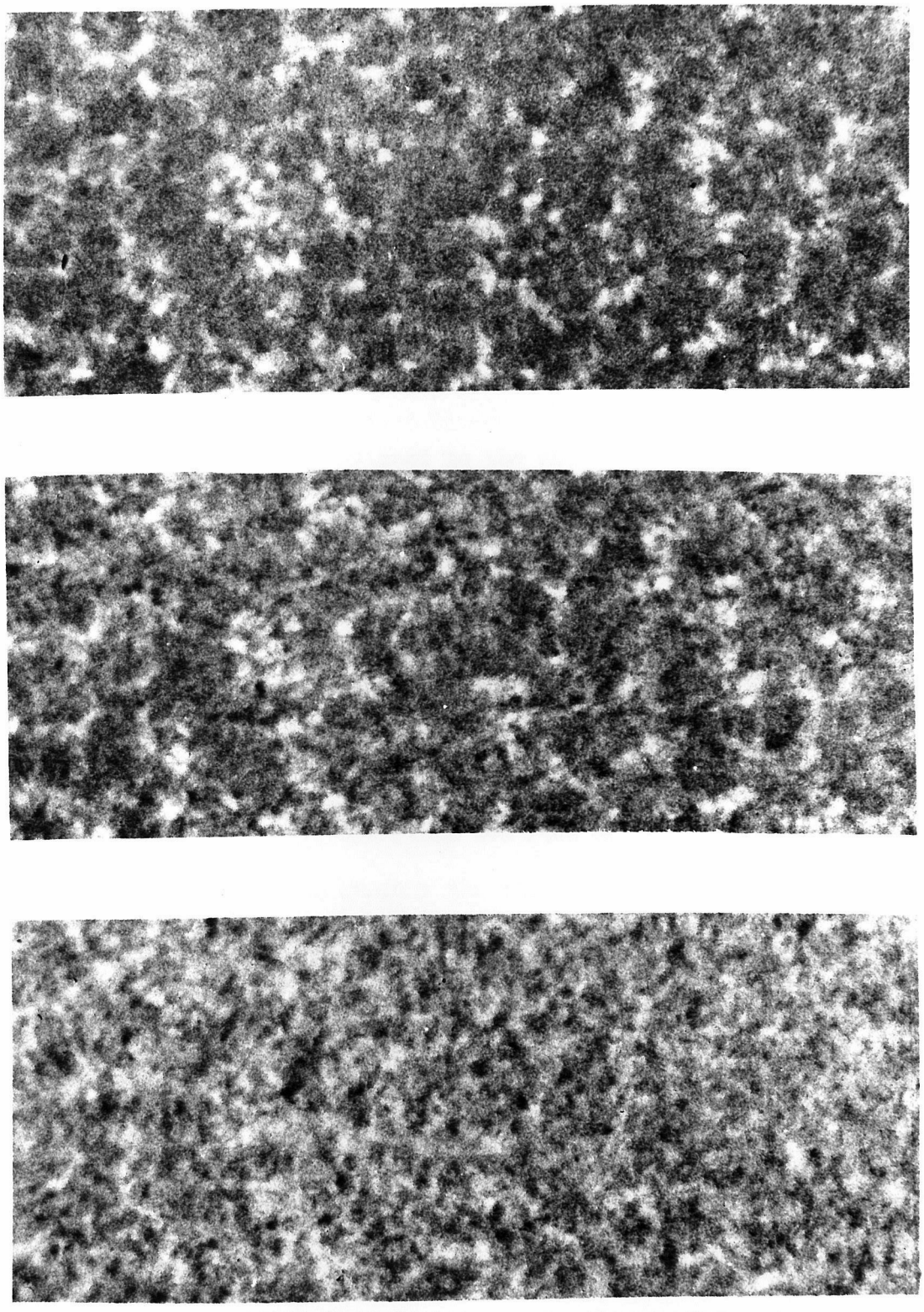

Figure 20

Table 10

Line	$\Delta\lambda$	No. of Plates	No. of Measurements	Ave. Vel. (km/sec)	Max. Vel. (km/sec)
Hα	0.70A	2	13	-1.3	-2.0
Hβ	0.40A	3	36	-1.1	-1.9
Hβ	0.32A	1	15	-.53	-.84
Hβ	0.24A	1	20	-.55	-.82

No errors have been assigned to the above velocities because of the large (30 - 50 percent) uncertainties in the calibration and plate reduction processes, discussed in detail by RWN and also in Part III. The sample standard deviations for the above measurements (which refer to relative velocities) were 10 - 20 percent on each plate.

In this paper we are primarily interested in the network velocity pattern; namely, the first two rows of Table 10, which presumably originate from roughly the same elevation in the chromosphere, where the network pattern is best visible. These velocities are in close agreement with each other, and with the results of de Jager (28), who quotes an r.m.s. velocity displacement of the Hα line of $\pm$ 1.1 km/sec. In addition, Giovanelli and Jefferies (30), using Hα photographs taken with a birefringent filter and processed by essentially the same photographic subtraction technique as in the present work, find the same velocity structure as de Jager and ourselves. Although they do not quote velocity data, they show a schematic diagram ((30), p. 216) of the chromosphere which

indicates mainly falling velocities in the network, and some rising velocities in the centers of these "cells."

We have also calculated the network velocities with auto-correlations, rather than with the microphotometer. From the measured FWHM (average size = 5.2×10^3 km) we computed H vs δ^2 curves using the correlation model described by equations 12 and 13, and thus find average downward velocities of 0.44 km per second, only about 40 percent as big as from the microphotometer tracings. The discrepancy can be easily explained in a qualitative manner. The annular ring model assumes the existence of completely closed, uniformly bright annuli. In the first place, visual inspection shows that most of the network cells are very fragmented in appearance. Just by noting that the observed structure probably doesn't exceed 50 percent of the packing of an ideal close-packed network, would at least double the true H, and thus increase the measured velocity by about 40 percent. Secondly, the microphotometer tracings were made through regions where the network structure was most pronounced, while the correlation function was integrated over a much larger region including some rather faint network patterns. A third effect, counter to the first two, is the additional height in the auto-correlation function due to small-scale granulation and other "noise" not associated with the network pattern. It is difficult to estimate the magnitude of this effect, which is probably not too large due to the rather "quiet" appearance of the background.

Up to now, we have assumed that our standard Doppler subtraction procedure is valid in studying velocity fields in the Balmer lines. There are, however, a number of difficulties in interpreting these observations:

Firstly, even if our Doppler calibration procedure is correct, we have still only measured the network velocity relative to the background. The numbers quoted in Table 10 are real receding velocities only if the intra-network region has essentially no radial velocity component.

Secondly, the opacity and line profile in the network and in the background are probably different, so that we may well be observing features at different temperatures and/or different levels in the atmosphere. That is, the calibration profile on our Doppler plates is an "average" profile, whose shape is due to a mixture of the many types of structures seen in the Balmer lines, formed at different heights and temperatures. The observed fact that the network pattern is darker than the background in Hα at $\Delta\lambda = \pm 0.7$A, but lighter than the background in the core of the line, implies that the line profile associated with the network is somewhat wider and more shallow than the "average" profile. This would explain the increased contrast in the red wing where the downward moving material is seen, and the higher contrast on the violet side where the small rising dots are observed. It should be noted that both the dark and light elements on the Doppler-cancelled plate are darker than the background on the

original spectroheliograms taken in both the red and violet wings of the line. From the above discussion, since the "true" profile in the network region seems to be less steep than the "average" profile, the measured quantity $d(\ln T)/d\lambda$ is probably too large. Thus the velocities in Table 10 would be too small, and can be considered as lower limits on the real velocities.

Thirdly, both for $\Delta\lambda = \pm 0.7$A in Hα, and $\Delta\lambda = \pm 0.40$A in Hβ, the profile slope is not constant, so that accurate Doppler calibrations are difficult in the region where the network is most prominent.

Despite all these qualifications about the accuracy of the results, it seems rather safe to say that there is a predominantly downward motion in the network. This is the conclusion of primary importance for our study, and leads us to the second half of this section; namely, the correlation between the downward flowing hydrogen network and the bright Ca II network.

Two Hβ and one Hα plates were cross-correlated against Ca II plates, with the results shown in Table 11, where F is the by-now-familiar cross-correlation coefficient.

These results strongly confirm visual observations of this correspondence, which is apparent to the eye either by using the moiré effect or by matching structures on the two plates. The values of F indicate excellent correlation, although they are less than 0.5. It will be recalled from Part IV(D) that it is very difficult for F to exceed 0.8. This correction alone brings

Table 11

Case	Date	Lines	Image Size	Δt	F
1	6-27-62	Hα - K	17 cm	$0^h\ 37^m$	0.19
2	8-12-62	Hβ - K	17 cm	$1^h\ 43^m$	0.44
3	8-22-62	Hβ - K	17 cm	$0^h\ 38^m$	0.46

two of the "true" values close to 0.6. We have previously pointed out that the hydrogen network is very fragmented, much more so than in Ca II. This is a real effect, which will lower the correlation. Another look at Figures 19(b) and 20(a) will convince the reader that the network appears more broken in Hα than in Hβ, one reason for the relatively small F in Case 1. Two other effects decrease F. One is the time difference Δt between exposure of the correlated plates. The second, and more important effect, is the fine mottling and other "noise" which adds appreciably to the heights of the auto-correlations, but not to the cross-correlation, as already mentioned in previous sections. This noise is particularly high in Case 1, because both the Hα plate and the K_{2v} plate used in the correlation were of "grade A" variety, thus showing a great deal of fine detail, and present another reason for the low value of F for this case.

To summarize this section, our observations confirm those of other authors with regard to the downward flowing material seen in the Balmer lines, and in addition show that this velocity

network coincides with the Ca II network, and thus occurs at the boundaries of the large cells.

F. Correlation Between Photospheric Magnetic Fields and the Ca II Network

That there exists a close spatial correspondence between Ca II plages and bipolar magnetic field regions was first observed by H.W. and H.D. Babcock (9), using the solar magnetograph (10). By modifying several features of the magnetograph apparatus, Howard (6) was able to obtain magnetic field tracings with much better spatial resolution (his aperture was a square 10" of arc on a side), and again found that the correlation between Ca II emission and magnetic fields* was excellent. Howard's investigation ranged over field strengths of about 5 to 75 gauss, with observations made both in sunspot regions where plages were usually present, and away from sunspots where generally only the Ca II network was visible. Howard's work was simultaneously complemented by that of Leighton (8), who used a different approach to map the solar magnetic field, a method which had the advantages of far better spatial resolution and scanning speed, but was only able to record intensities above about 20 gauss. Leighton's magnetic spectroheliograms confirmed photographically the observations of the Babcocks and Howard. Both Leighton and Howard found the K-B correlation so striking that the former speculated that "all calcium emission, no matter where it occurs on the solar surface, is associated with magnetic fields" ((8), p. 376) while the latter suggested a "nearly

* Henceforth called "K-B" correlation.

one-to-one correspondence between the magnetic features and the calcium-plage regions, not only with respect to their generally similar location but also in most small structural details" ((6), p. 196).

Although the K-B correlation is clearly apparent to the eye when looking at the figures in references 6 and 8, no quantitative analysis of this correlation has been attempted, and not even a qualitative study has been made at field strengths less than 5 gauss, the lower limit of Howard's studies. In the present investigation, three different techniques were used in an effort to quantitatively measure the correlation at field levels below 5 gauss.

The first method was an attempt to extend the sensitivity of Leighton's apparatus to field strengths below 20 gauss. It was hoped that through the use of an improved beam splitter which transmitted more light and thus permitted narrowing the spectroheliograph slits, one might increase the Zeeman sensitivity of the apparatus. However this approach failed, firstly because it was impossible to increase the sensitivity enough to reach the 5 gauss level, and secondly because the photographic noise level remained at least as high as in the earlier work. In addition to the noise causes discussed by Leighton, the major sources of noise which swallowed up signals below 20 gauss appear to be due to nonuniformities in the polaroids and/or quarterwave plate. These produce a rippled or "curleycued" appearance to the background, and are very hard to distinguish from low-intensity field patterns, which usually are in the form of short lines or pieces of a network pattern.

The second method was suggested by Leighton and carried out on Sept. 20-21, 1962 by Howard and the author, using the solar magnetograph in the 150 foot solar telescope at Mount Wilson Observatory. The two exit slits of the spectrograph were separated by 25.7 mm so that the Fe I (λ5250) line was centered on the first exit slit in third order light, and the Ca II (λ3933) line was centered on the second exit slit in the fourth order. With a fourth order dispersion of 0.21A/mm, the second slit width of 2.3 mm corresponded to a wavelength spread $\Delta\lambda$ = 0.48A, which is roughly the width of the K_{232} emission peak. The light emerging through this slit passed through a dark blue filter, and thence to a 931A photomultiplier tube and amplifier. The light from the first exit slit was treated in the usual magnetographic fashion, set in the magnetic mode. The aperture for the incident light was a rectangle 10" × 18" of arc, located near the center of the 40 cm solar image. The magnetic signal was fed into the Y channel and the K_{232} emission signal into the X channel of a Mosely X-Y recorder. (In addition, each signal was separately measured on a strip-chart recorder.) Any correlation between the Ca II emission and magnetic field intensity should then show up directly through a motion of the X-Y recorder pen away from the X and Y axes.

A series of roughly NNE-SSW-direction scans were made, separated from each other by 30" of arc. Three such scans are shown in Figure 21. In Figures 21(a) and 21(b) the magnetic field calibration is 10 gauss per inch along the vertical axis, while in 21(c, left) the scale is 20 gauss/inch and in 21(c, right) it is

Figure 21. Actual X-Y recorder tracings showing K-B correlation. Roman numerals indicate: I, "No-light" noise level; II, Noise level with aperture open at fixed point on solar image; III and IV, tracings made with aperture moving back and forth across image. Motion of recorder pen along x-axis indicates change in K_{232} intensity; motion in y-direction measures magnetic field changes. Figures 21(a) and 21(b) are tracings in "quiet-sun" regions; figure 21(c) is over a small plage.

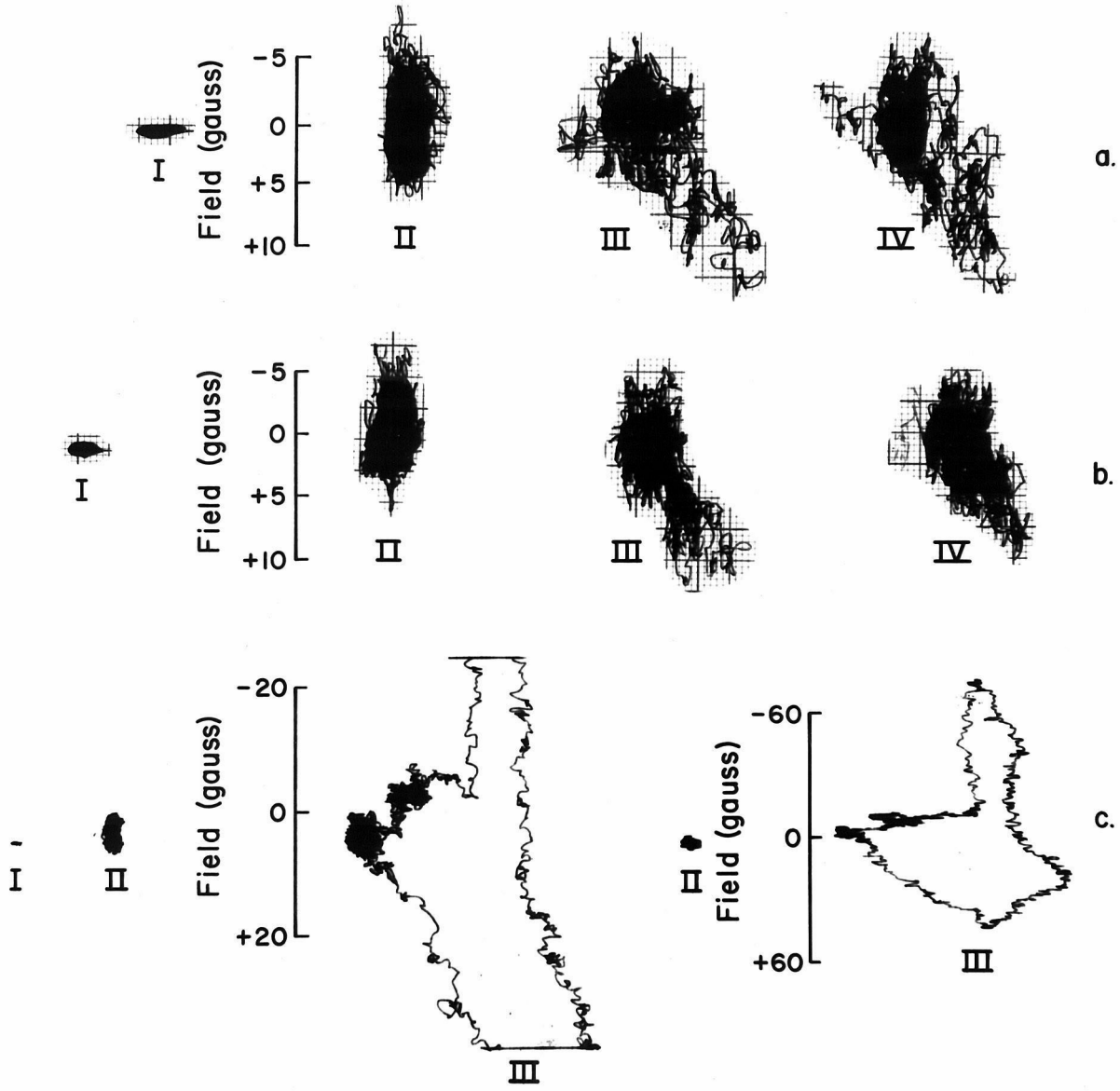
I
Field (gauss)
-5
0
+5
+10
II
III
IV
a.
I
Field (gauss)
-5
0
+5
+10
II
III
IV
b.
I
II
Field (gauss)
-20
0
+20
III
II
Field (gauss)
-60
0
+60
III
c.

Figure 21

60-65 gauss per inch. Figures 21(a) and 21(b) were obtained from scans made in quiet regions of the sun, where the Ca II emission occurs primarily in the network, while 21(c) came from a scan through a small sunspot region. The magnetic field polarity is mainly positive (down on graph) in (a) and (b), while it has both signs in (c). On each figure, I is the no-light noise level, II is the light-on noise level with the scanner stationary, while III and IV are the actual scans. It is seen that the noise level II is 3-4 gauss, and that the method is quite successful in directly showing the K-B correlation if the field level is 5 gauss or larger.

In the third and most successful attempt to demonstrate the correlation below the 5 gauss level, a more detailed analysis was made of the polar region magnetograph tracings and Ca II spectroheliograms obtained by Howard (6). Using his tracings of September 3 and 5, 1958, magnetic contour maps were made at the 2, 5, 10, and 15 gauss level. The latter three levels resulted in contour maps essentially the same as those shown in Figure 4 of (6); new information was obtained only by addition of the 2 gauss contour. (It should be noted that due to a calibration error in the present work, the contour levels for the September 5 case were actually 1.5, 3.5, 7, and 11 gauss, somewhat smaller than had been intended.) In all cases, the measured levels were well above the noise level, which was less than one gauss. The two Ca II spectroheliograms were enlarged to the same scale as the magnetic maps, and black-on-white drawings made of the regions where K_{232} emission was visible.

The quantitative analysis of the K-B correlation was made in three stages, as follows:

1. From the contour map, a black-on-white drawing was made of those regions having field strength $B \geq 10$ gauss, as shown in Figure 22(a) for the September 3 case. It will be recalled that Howard's scans were made with a 10" of arc aperture, adjacent scans being 10" apart, so that the entire region was mapped out. In the present analysis, a straight-edge was placed along the center of each 10" scan on Figure 22(a), and a line drawn wherever the straight-edge intersected a region having $B \geq 10$ gauss. The line drawing so produced is Figure 22(b). Next the K_{232} emission drawing and the line drawing were superimposed on a light box. Each line segment was then given a value 4, 3, 2, 1, or 0, depending on whether it was completely covered by K_{232} emission, 3/4 covered, etc. A line segment was considered to correlate with the K_{232} emission whenever it had a value 3 or 4, and to anticorrelate if the value was 0 or 1. Segments with value 2 were not counted. This procedure was carried out both when the two drawings were in proper alignment, and in three other "random" orientations. These last three measurements essentially determine the fraction of the area covered by the K_{232} emission, just as discussed in section IV(B). As before, the cumulative binomial probability distribution is used to calculate the probability that the observed correlation is merely a random statistical fluctuation.

2. In the second stage of the analysis, drawings similar to

Figure 22. a) Black regions contain magnetic fields ≥ 10 gauss. Small open square in lower left-hand corner shows size of aperture (10" of arc on a side).

b) Line drawing of a) produced by placing straight-edge along the center of each 10" scan, and recording positions of magnetic fields.

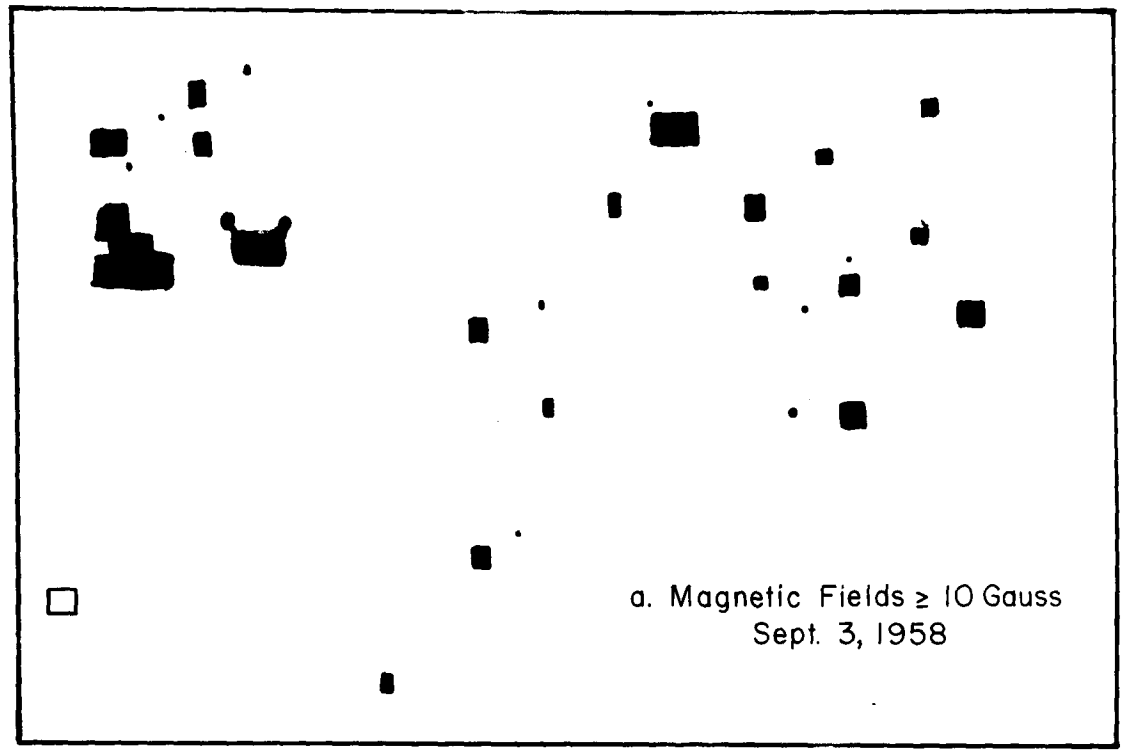

a. Magnetic Fields ≥ 10 Gauss
Sept. 3, 1958

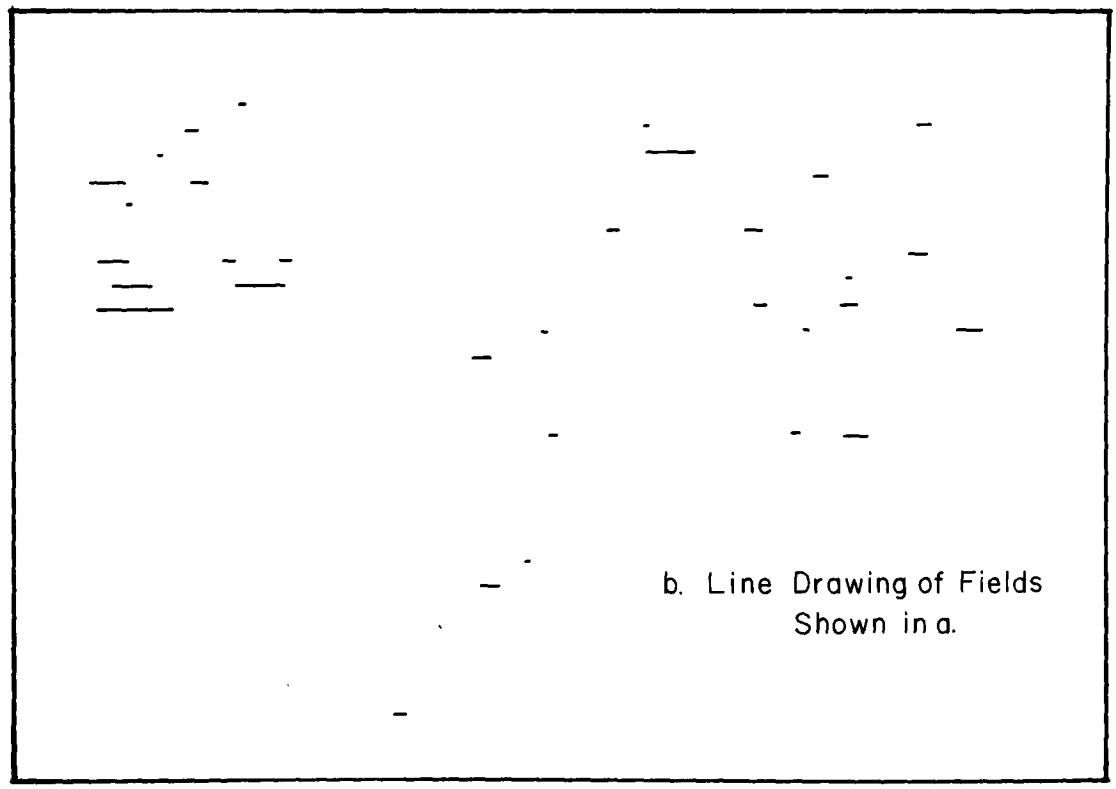

b. Line Drawing of Fields
Shown in a.

Figure 22

those of Figure 22 were made, with the new criterion that all fields with $B \geq 5$ gauss were now included. The K-B correlation was measured exactly as in the previous case.

3. Since it is obvious that there must in general be a region of lower field strength surrounding a given contour line, it is expected that a certain amount of "artificial" correlation would exist between fields with strengths of two gauss and the K_{2v2} emission, even if the "true" correlation were due only to fields greater than 5 gauss. Thus, before making the B = 2 gauss analysis, a new drawing similar to that of Figure 22(a) was made, which included all fields in the range $2 \leq B < 5$ (or, $1.5 \leq B < 3.5$ for September 5). That is, all the high-level fields were removed, resulting in Figure 23(a). In addition, all of the Ca II emission which corresponded spatially with the strong magnetic field regions was similarly removed from the Ca II emission drawing. The resulting drawing, full of rectangular "holes," is shown in Figure 23(b). In both Figure 23(a) and 23(b), a small additional region surrounding the B = 5 contour line was also removed, to further reduce any remaining "artificial" correlation. It is hoped that by this method, any correlation which still persists is really due to weak magnetic fields, of strengths less than five gauss.

The results of this investigation are shown in Table 12. At the 5 and 10 gauss levels, in each case there is, roughly speaking, only about one chance in a million, that the observed correlation is due to random statistical fluctuations. Note that about 95 percent of the line segments correlated with the Ca II

Figure 23. a) Magnetic fields on 9/3/58 with strengths $2 \leq B < 5$ gauss. Note rectangular "holes" where stronger fields have been removed.

b) Drawing of Ca II emission (shown in black) for same region of sun as in a), with "holes" corresponding to regions where strong (> 5 gauss) fields existed.

a.

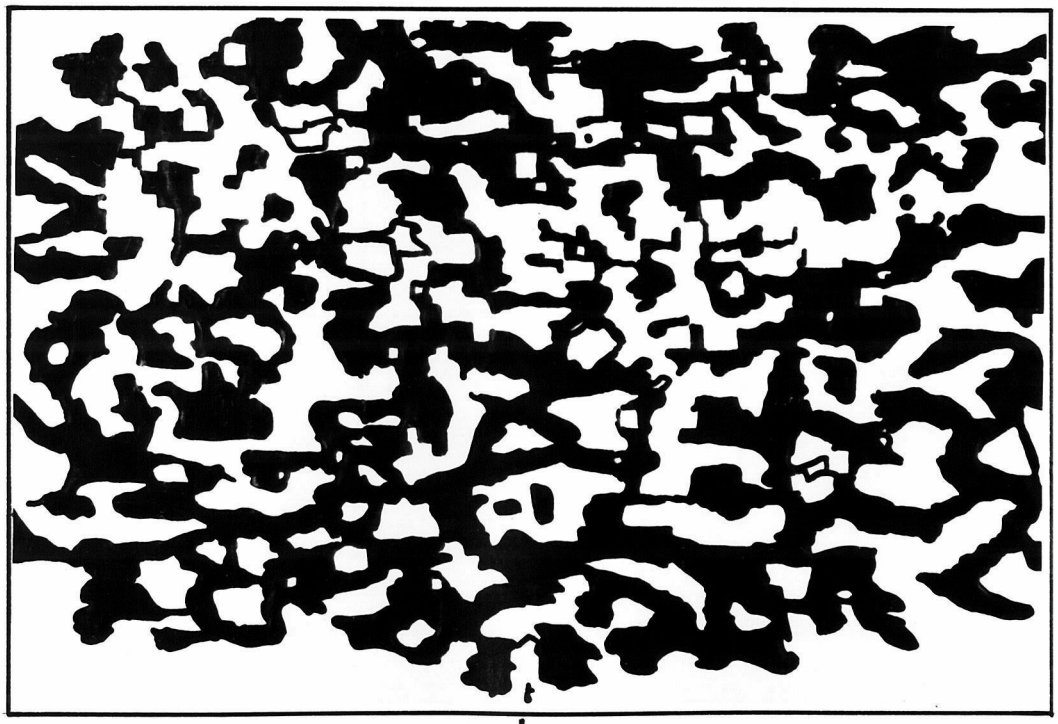

b.

Figure 23

emission at the 10 gauss (7 gauss, September 5) level and 80 percent at the 5 (3.5) gauss level. At the 2 (1.5) gauss level, only 60 - 65 percent of the line segments correlated, and there remains a 2 (6) percent probability that this weak field correlation is due to chance. However, if we treat these two cases (September 3 and September 5) as independent events, the probability that both correlations are merely random fluctuations is only about one in a thousand. Furthermore, there are several reasons to believe that the true correlation is higher than measured, but this discussion will be deferred to Part V.

Table 12

Field (gauss)	Date (1958)	Trials N	Successes R	R/N	P	E(N; R, P)
2	Sept.3	423	272	.64	.59	.020
1.5	Sept.5	472	285	.60	.57	.059
5	Sept.3	91	76	.84	.63	1.7×10^{-5}
3.5	Sept.5	132	105	.80	.54	5.6×10^{-10}
10	Sept.3	32	30	.94	.54	1.3×10^{-6}
7	Sept.5	29	28	.97	.55	6.5×10^{-7}

This completes the section describing the observations and results. We turn now to Part V, in which we first summarize these findings, and then try to combine them into a coherent picture of "supergranulation" phenomena.

V. DISCUSSION

A. Summary of the Results

Since we have discussed at some length a number of seemingly diverse phenomena, it seems appropriate at this point to briefly summarize these observations. First we described a system of "large cells" with average diameters of 30000 km and lifetimes of 20 hours. These velocity cells consist of mainly horizontal motions, the flow proceeding from the center of each cell toward the boundary with 0.4 km/sec average velocity. At any given time, there are roughly 5000 cells on the solar surface. Evidence was found for the existence of small vertical motions in the cells, the direction of the velocity being upward at the cell centers, and downward at the boundaries. The average magnitude of this vertical motion is perhaps on the order of 0.1 km/sec.

Secondly we measured correlations between the cells and three other phenomena; namely, the chromospheric Ca II emission network, the downward-flowing Hα and Hβ network, and the 1.5 - 15 gauss magnetic field pattern. The correlation, in each case, showed that these phenomena occur at the boundaries of the cells.

From these observations, we are now able to construct a plausible and consistent model of large-scale phenomena which exist in the atmosphere of the quiet sun. Four significant solar features are explained or clarified by this research:

1. Definite proof of the existence of a large-scale structure in the photosphere. Up to the time of Leighton's two-dimensional Doppler photographs (2), only Miss Hart's spectrographic (one-dimensional) tracings (17) had shown this structure, and her results had been seriously challenged by Fellgett (47) and others, who implied that the secondary maxima in Miss Hart's "correlograms" were not truly solar phenomena but due to spurious effects such as poor seeing. This controversy has now been resolved in Miss Hart's favor by our photographs which strongly corroborate her work. Not only does Miss Hart concur with our conclusion that the distribution of cell sizes is very irregular,* but also her peak velocities of 0.3 - 0.5 km/sec agree perfectly with our results. Two other one-dimensional studies of the large-scale velocity field have also recently confirmed our observations. One is the previously mentioned work of Evans and Michard (23); the other is the magnetographic study (using the Doppler mode) of Howard (48), who measured a power spectrum with a strong maximum in the 20×10^3 - 60×10^3 km wavelength region.

2. The horizontal cell motions provide a mechanism (to be discussed later) for building up relatively large magnetic fields in a narrow network pattern, which we observe. With these magnetic "channels" we will then explain:

---

* Miss Hart pointed out that the broad maximum and small peak in her correlogram reflected the absence of a single well-defined size.

3. The origin of the Ca II (K) emission network which has puzzled observers for seventy years since its discovery by Deslandres (25). The same phenomenon also produces the bright emission network in the center of the Hα line, and the dark network in the wings of Hα and Hβ.

4. Finally, the magnetic field enhances the flow of ionized material and the propagation of magnetohydrodynamic (MHD) waves in the channels, thus accounting for the downward-flowing Hα, Hβ network and the presence of spicules (46) in these regions.

We shall now discuss each of these four points in more detail.

B. Interpretation of the Observations

1. Large Cells as a Convection Phenomenon

From the observed dimensions of the large cells (30000 km) it seems obvious that they must have their origin somewhere in the sun's convective envelope which extends from the bottom of the photosphere to depths of 50000 - 100000 km; thus it seems reasonable to assume that the cells are convective motions. Leighton has coined the term "supergranulation" to describe the large cells. In analogy to Schwarzschild's description (35) of the small-scale granulation, it seems that what we are observing can probably best be described as non-stationary convection, a condition somewhere between Bénard cells (36) on the one hand and completely irregular turbulent convection on the other. The classical Bénard cells represent a stationary laminar convection with quite regular

polygonal cells of almost equal sizes and shapes. As we have seen, however, the supergranulation has a very irregular size and shape structure, and the 20 hour lifetime, though it seems very long at first glance, is actually rather short when one considers the large distance scale with which we are dealing. Since we are unfortunately unable to look at these cells from the side, but only from above, we have no way of determining whether this convection is a circular cellular convection, or, what is more likely, a columnar type of convection such as a cloud or plume. Both Leighton (2) and Spiegel (37) have adopted the latter viewpoint. Such plumes often have "mushroom" or "cauliflower" tops, as seen, for example, in nuclear bomb explosions or in the beautiful experiments of Batchelor (38). If the horizontal cell motion which we observe on the sun is similar to such a mushrooming cloud top, then it is not hard to understand why the underlying vertical motion is mainly hidden from view.

Let us try next to estimate the depth from which this convective motion originates. Consider some examples from nature. If D is the cell diameter, and H the depth, then the ratio $R = D/H$ ranges between 2 and 3 in both experimental and theoretical calculations of stationary Bénard cells. However, in non-stationary convection observed in nature, R is usually 5 to 10; this holds true over tremendous density and size ranges of at least 10^8! As examples, we refer the reader to Woodcock and Riley's observations of convection patterns in pond ice (39) which had $R = 10 - 30$, to Tiros I satellite photos of cloud formations

over oceans (40) with $R \approx 10$, and solar granulation which has $R \approx 5$.* In particular, the Tiros I photos show an amazing resemblance to the Ca II network pattern in the solar chromosphere. Thus for supergranulation diameters of 20000 - 50000 km, and $R = 5 - 10$, we might expect a range of depths $H = 2000 - 10000$ km. As a second order-of-magnitude argument, it has often been observed that the lifetime T of a cell in non-stationary convection is given by $T \approx H/V$, where V is the average velocity of the rising currents. From our measured lifetime of 20 hours and assumed vertical velocity of 0.1 km/sec, we obtain $H = 7200$ km, in good agreement with the previous values.

It seems proper then to ask whether there is any mechanism in the sun which would select cell depths of roughly 5000 km, when the convection zone extends much farther, approximately 10 to 20 times that depth. A possible solution lies in the ionization zones of either neutral He atoms or singly ionized He^+, or perhaps both. According to a solar model of Iben and Sears (41), shown in Figure 24, these two regions begin at depths of about 2000 and 7000 km, respectively, which agrees very nicely with the above calculations. Zero depth in Figure 24 corresponds to optical depth 2/3, perhaps 300 km below the top of the photosphere. Note that Figure 24 also shows the hydrogen ionization

---

* In the solar atmosphere the height H cannot, of course, be measured like the depth of a pond of ice. In this case, we define H as the scale height at the granular level (about 200 km), and compare this with the average granule diameter of perhaps 1000 km.

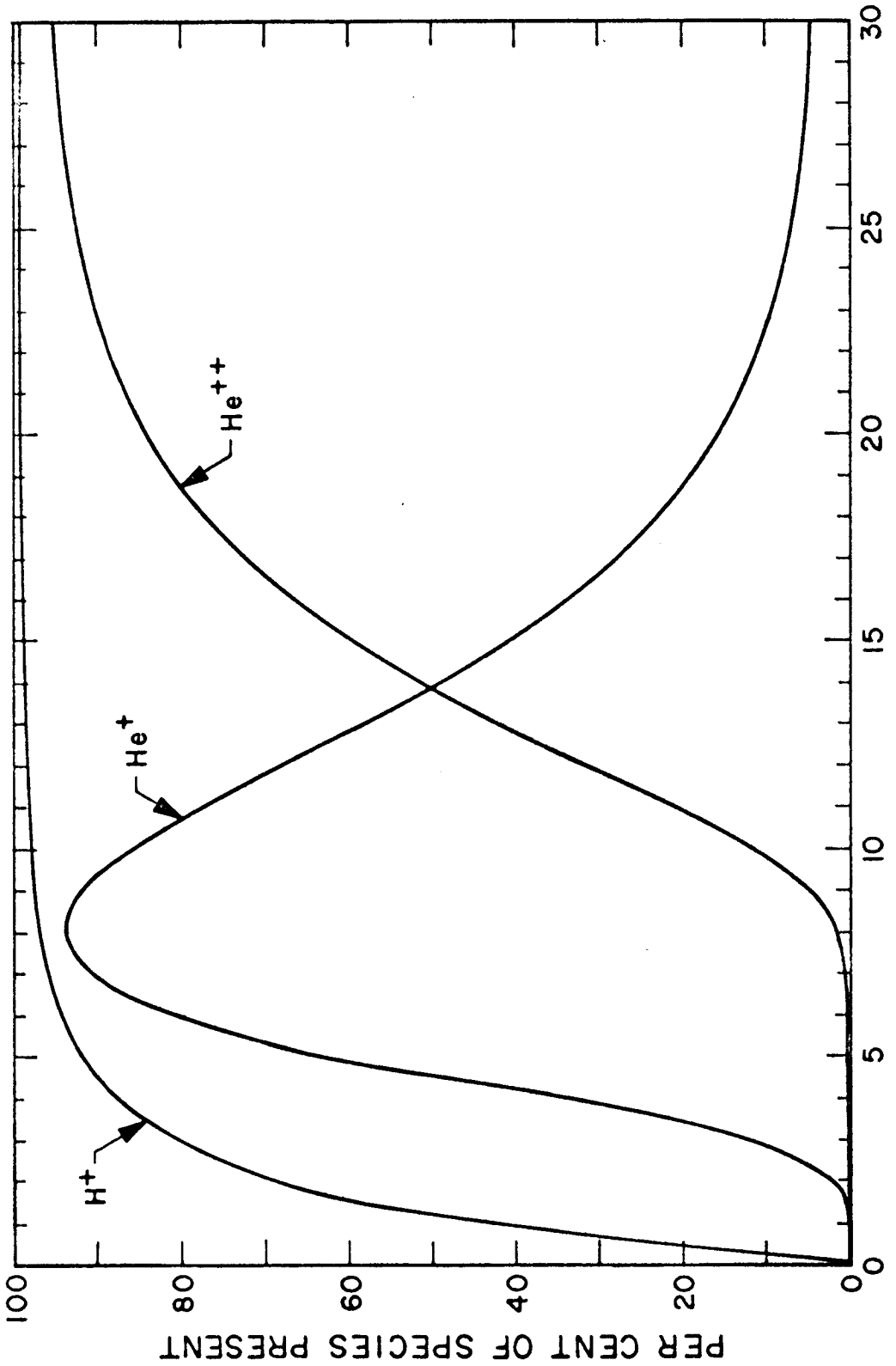

Figure 24. Ionization of hydrogen and helium in the convective envelope of the sun. Depth is measured relative to optical depth 2/3 in the continuum.

zone which lies immediately below the photosphere. It is often argued that this hydrogen ionization may be partly responsible for the formation of the granulation because it produces a region with lower molecular weight lying below one of higher molecular weight, thus adding a secondary instability or perturbation to the already unstable convection region. A similar argument would then be applied to He ionization to "explain" the supergranulation.

Before leaving the subject of the supergranulation, let us make an order-of-magnitude estimate of the energy flux deposited at the top of the photosphere by these cells. Writing the convective flux as $F = \rho \epsilon C_p V(\Delta T)$, where $\epsilon = .01$ is the fractional area covered by the rising columns of gas, $\rho = 2 \times 10^{-8}$, $C_p = 1.5 \times 10^8$, $V = 10^4$, and $\Delta T = 100^\circ$, (all units are cgs), we obtain $F = 3 \times 10^4$ ergs/cm^2/sec, about a factor of 1000 less than that due to the granulation. The value of ΔT was not calculated, but arbitrarily chosen equal to computed temperature differences (35) in the granulation regions. To estimate ϵ, we considered a rising core at the cell center with diameter of about 3000 km relative to the typical cell diameter of 30000 km. For V we took our earlier 0.1 km/sec estimate, while the density was taken from Allen (42).

We shall now turn to an analysis of the regions of enhanced magnetic field strength, which appear to be caused by the large cell motions, and then, in turn, provide mechanisms for the other

phenomena which we observe.

2. Magnetic Regions Due to Large Cell Motions

In describing magnetic phenomena in the solar atmosphere, which contains sufficient ionized material to make magnetohydrodynamic effects important, one usually employs the parameter ν, defined as the ratio of the magnetic energy density $\beta = B^2/8\pi$ to the kinetic energy density $\alpha = \rho v^2/2$. Whenever ν is less than unity, magnetic fields tend to be carried along with the mass motions, while the condition $\nu > 1$ implies that the matter can be "trapped" by the magnetic lines of force. Thus, near the top of the photosphere, where we observe horizontal cell motions of 0.4 km/sec and densities of 2×10^{-8} g/cc, we calculate that $\nu \approx 0.0025$ if we assume an average field strength of about one gauss (43). These small fields would therefore be swept to the cell boundaries by the horizontal currents, and concentrate there in strengths several times greater than the average field. Theoretically it would be possible in these regions to constrain magnetic fields up to about 20 gauss, the limit being reached when equipartition of kinetic and magnetic energy occurs; i.e., when $\alpha = \beta$. Let us compare this prediction with the observations. As we mentioned in Part IV(F), on the best Zeeman plates obtained by Leighton's method (8), we often detect very faint magnetic fields in the form of short lines or segments of a network pattern. Since these narrow regions are barely detectable, they must have field

strengths comparable to the sensitivity of this method, namely 10 - 20 gauss. Furthermore these field regions are sometimes so narrow that they are seen only on plates with excellent seeing. This indicates that the widths of the magnetic network in many cases may not exceed perhaps one second of arc ($\approx$ 700 km), which is approximately the best resolution obtainable with the 60 foot tower telescope.* These results are in excellent agreement with the observations of Howard (48) and Kiepenheuer (49). Howard, using an aperture about two seconds of arc on a side, measured r.m.s. magnetic field fluctuations of 8 gauss, with peaks of 10 - 20 gauss occurring at distances of perhaps 20000 - 30000 km along his tracings. Kiepenheuer's earlier work had much poorer spatial resolution; however he also found occasional "field patches" in the 10 - 20 gauss size. Under good seeing conditions he observed a fine structure in these patches, and speculated that this structure had dimensions not larger than 10 or 20 seconds of arc, and that the field amplitudes might well exceed 20 gauss. Also we compare these results with our study of Howard's tracings (6) described in Part IV(F). In this case, the aperture was 10 seconds of arc on a side, and we found that a field level of about 2 gauss correlated well with the Ca II network. If the actual dimensions of the magnetic fine structure are really closer to 2 seconds of arc on a side, then we must correct our smeared-out observations, and

---

* Of course the possibility exists, from an observational point of view, that we are seeing only smeared-out fields due to our resolution limits, and that the actual fields are stronger and concentrated in smaller regions.

then obtain a field of roughly 50 gauss. To summarize these observations, we note that the observed fine-structure field strengths of perhaps 10 - 50 gauss are consistent with the limit imposed by the equipartition argument.*

We have not yet explained how the average solar field of perhaps one gauss can be magnified 10 to 50 times to the observed values. This is accomplished as follows. Since we have pointed out that the field lines are "frozen" into the matter and swept to the cell boundaries by the horizontal motion of the supergranulation, we may invoke the conservation of magnetic flux $\phi = \int B \cdot dA$ to qualitatively satisfy the observations. That is, if we compress the lines of force into a smaller area, the field strength rises proportionally. Considering a square cell with side 30000 km, enclosed by a narrow boundary one second of arc wide (700 km), it is easy to calculate that the ratio of total enclosed area to boundary area is approximately ten. Therefore an average field of 0.5 - 2.0 gauss would lead to a network pattern of 5 - 20 gauss, in very good agreement with the observations. Because this calculation is very sensitive both to the assumed width of the boundary region, and to the estimated strength of the average magnetic field, the excellent quantitative agreement is perhaps only fortuitous.

---

* The 50 gauss figure is not in disagreement with the 20 gauss limit mentioned earlier, since it was obtained by studying the Fe (λ5250) line which is formed deeper in the atmosphere where the density may be a factor of 10 or so higher. Thus equipartition would permit fields roughly 3 times larger than the previous limit. In addition of course, these arguments are only order-of-magnitude, and we should not take factors of 2 or 3 seriously.

We have dealt here with a concentration into narrow regions, of the weak (≈ one gauss) average field of the sun. The origin of this low-intensity field on the sun has been a subject of much controversy for some forty years.* It is argued that by a "dynamo" or "spaghetti" process, it is possible for turbulent motions to induce local magnetic fields. Some authors have claimed that this process will continue to build up the field strength until the equipartition limit is reached. Others have disagreed, pointing out that the turbulence will split the induced field into small parts, preventing it from reaching large values. Agreeing with this latter viewpoint, Cowling ((50), p. 94) asserts that "the field can be maintained only as a result of some large-scale dynamo mechanism depending on a fairly regular large-scale motion." The supergranulation may provide this regular large-scale motion, although this is speculation and not supported by calculations or observations.

Another qualitative observation is worth mentioning before we leave this section. We often observe at the periphery of sunspot and plage regions that the patches of magnetic fields and Ca II emission tend to break up into a network pattern. In Ca II spectroheliograms the transition from solid plage to bright network to weak network is a smooth process as one follows the emission from the center of a sunspot outward into a quiet region on the solar surface.

---

* For references, see de Jager ((26), p. 103-104) and Cowling (50).

For examples of this behavior, refer to figures 7(b) and 7(c) of reference 8. In addition, if one traces the life history of a large sunspot region, many times one finds that as the spot group breaks up, the plage appears to disintegrate slowly into a network pattern. We infer from these observations that the horizontal currents in the large cells may be breaking off bits of magnetic field from the edges of the sunspot penumbra, sweeping them to the cell boundaries, and then slowly dispersing this field from one cell boundary to another, into a continually expanding network pattern around the sunspot group.

To summarize these observations, it appears that the large cell motions are closely connected with the localization of magnetic fields in the solar atmosphere, both by concentrating the weak average field into narrow network regions, and through the breaking up of concentrated sunspot fields into a wide-spread network pattern. In addition we have suggested, without any proof, that the supergranulation may also provide the large-scale dynamo mechanism discussed by Cowling. We consider next some of the consequences of the magnetic network.

3. Origin of the Ca II and Hydrogen Networks

The fine network of relatively strong magnetic fields formed by the large cell motions is presumed to extend upward into the chromosphere, and there forms the basis for the Ca II, Hα, and Hβ networks, as follows. Osterbrock (45) has shown that enhanced

heating of the chromosphere occurs in those regions where magnetic fields exist. Therefore we expect the network structure to be at a higher temperature than the surrounding material. According to the theory of K and Hα line formation summarized by de Jager ((26), p. 131), this is exactly the condition required to explain the bright network in the cores of the K and Hα lines, and the dark network in the wings of Hα (and Hβ). That is, previous observers had correctly predicted higher temperatures for the network regions, but were unable to explain a mechanism for producing these increased temperatures. Our observations of the strong K-LC, K-B, and K-Hα, Hβ correlations,coupled with Osterbrock's calculations, seem to provide the final link in explaining one of the oldest puzzles in solar physics. Thus, the Ca II network is not due to a circulation of matter in the chromosphere as suggested by Deslandres (27) and Wasiutynski (12), but due to one (the supergranulation) at the bottom of the chromosphere.

Two more points are worth mentioning. First, we would expect that the contrast between network and background should be a maximum in the region of highest energy dissipation. Osterbrock finds that for fields between 2 and 50 gauss, maximum dissipation occurs at chromospheric heights of 500 to 2000 km, which is in excellent agreement with the heights where the dark network is most clearly seen.

Secondly, the magnetic lines of force will diverge as they

extend higher into the chromosphere, where the matter density decreases, thus explaining the larger FWHM (10000 km) of the Ca II network at a height of 4000 km, compared to the Hα and Hβ network at 1000 km, which has a FWHM of 5000 km. And both of these widths are much larger than that of the photospheric magnetic fields, which are barely resolvable under the best seeing conditions, and thus generally not over 1000 - 2000 km in size.

To summarize many of our findings about the magnetic network and its relation to the Ca II network, we refer to Figure 25. The two columns of photos were obtained on successive days, July 18 and 19, 1962 and both refer to approximately the same region on the sun. In each column, the upper figure is a print of the original Ca (λ6103) spectroheliogram taken at a distance $\Delta\lambda = -0.072$A from the line center. Note that the solar surface appears to be very quiet; only one tiny spot is present in the July 19 photo. In the middle photos is shown the corresponding Ca II network obtained in K_{2v}. The magnetic network appears in the lower photos; these are Zeeman pictures obtained by Leighton's method (8). In a qualitative manner, it is easy to see three features from these two sets of photos: a) The long lifetime of the network structure (many objects clearly have survived for at least 24 hours), b) The strong K-B correlation which persists even in this quiet-sun region away from plage areas, and c) The much narrower appearance of the magnetic network relative to the K network.

Finally, we turn very briefly to the enhanced flow of ionized material and MHD wave propagation due to the magnetic network.

Figure 25. Photos taken on successive mornings showing details of the magnetic and Ca II networks. Left hand column, July 18, 1962. Right, July 19, 1962. Top photo in each case is original Ca (λ6103) spectroheliogram, middle picture shows Ca II (λ3933) emission, bottom photo is Zeeman plate showing magnetic field regions.

18 JULY 1962

19 JULY 1962

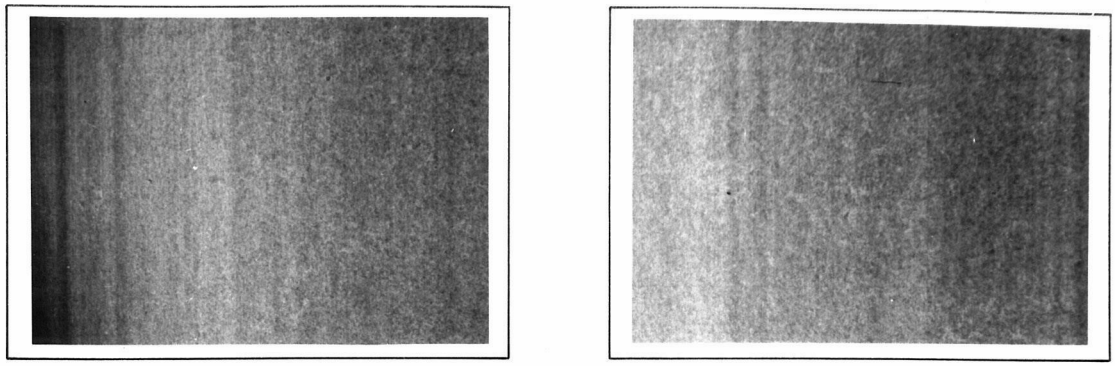

Ca (λ6103) SPECTROHELIOGRAMS

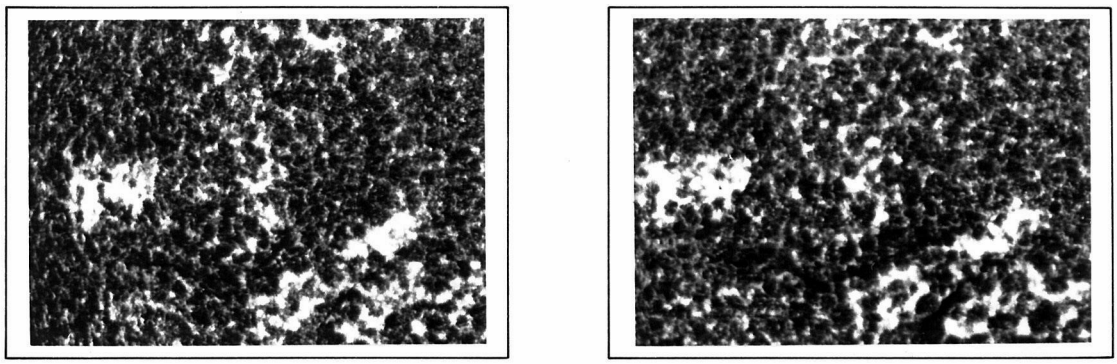

Ca II (λ3933) SPECTROHELIOGRAMS

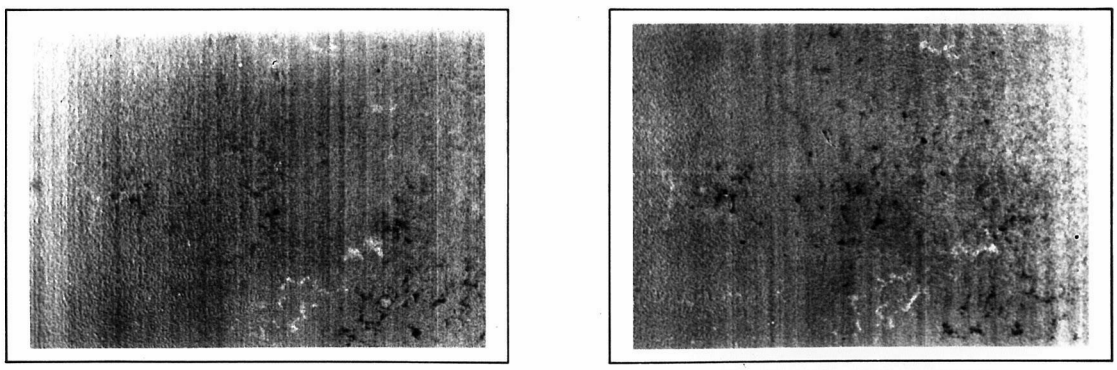

ZEEMAN PHOTOGRAPHS

Figure 25

0 1 2
Scale (10^5 km)

4. Magnetic Influences on Chromospheric Velocities

At the level of the large cells, we showed that the ratio ν of magnetic to kinetic energy density was much less than unity. However, in the chromosphere where we observe the Hα, Hβ and Ca II networks we find that $\nu > 1$. Let us suppose that the concentrated fields at the cell boundaries are on the order of 10 gauss. Then de Jager's values (44) for the densities at 1000 km (Hα, Hβ) and 4000 km (Ca II), namely, 8×10^{-11} and 10^{-13} g/cc, respectively, lead to ratios $\nu = 2.5$ and $\nu = 2000$, if we assume $v = 2$ km/sec. Thus at both heights ionized material can be trapped by the magnetic field in the network. Since some of the hydrogen and most of the metals at these chromospheric levels are ionized,* we would expect the matter to move more freely along the lines of force. If one accepts a chromospheric and coronal model in which matter is carried to high levels by various eruptions such as flares and spicules, then it seems reasonable that much of this excess material will slowly fall back down into the lower atmosphere. This descending, partly ionized gas should therefore funnel down along the lines of force concentrated above the cell boundaries, resulting in the descending network seen in the wings of Hα and Hβ.

It seems quite possible that the small rising spots which we see at the edges of the falling Hα and Hβ network are spicules seen

---

* According to van de Hulst (51), at the bottom of the chromosphere, only one hydrogen atom in 10^6 is ionized. But the fraction of protons increases rapidly with height, and becomes equal to the neutral atoms at a height of 4000 - 5000 km.

on the disc (46). This phenomenon, also, can be explained by the enhanced magnetic fields in this network region, if we accept Osterbrock's interpretation ((45), p. 347) of spicules as "slow-mode disturbances carrying chromospheric material up along the magnetic lines of force into the corona."

Before leaving the subject of the Hα, Hβ network velocities, we should mention that the present research seems to have cleared up the question raised by LNS concerning the possibility that the downward-moving Hα and Hβ motions might spread out horizontally upon reaching the photosphere and produce the observed horizontal velocities in the supergranulation. Since we have shown that the Hα and Hβ networks occur at the cell boundaries, then this hypothesis would imply horizontal motions toward the cell centers, not away from them as observed. In addition, there does not seem to be enough mass flow available, even if the direction of horizontal flow were correct. To estimate crudely an upper limit for the velocity V_o of the Hα network at the top of the photosphere (h = 0), we write a conservation equation for the mass flux: $\rho_1 V_1 A_1 = \rho_o V_o A_o$, where the subscript one refers to h ≈ 1000 km, the height at which we measure a velocity $V_1 \approx 2$ km/sec, and an area $A_1 \approx$ (FWHM)C ≈ 6000 C km^2, where C is the cell circumference. Since we see almost no vertical motion at the h = 0 level, we assume such motion, if it exists at all, must occur in a small region too narrow to be resolved on our spectroheliograms. So it cannot exceed roughly 1000 km in width, and we write $A_o = 1000$ C. At a height of 1000 km, the density is estimated to be $\rho = 8 \times 10^{-11}$ g/cc by de Jager (44),

leading to a maximum velocity at the top of the photosphere of $V_o \approx 0.05$ km/sec, which is much smaller than the observed horizontal velocities of 0.4 km/sec, even though we have neglected all dissipative phenomena in this crude calculation. We conclude that our observations are inconsistent with the hypothesis that the downward-flowing network causes the horizontal large-scale motions.

C. Conclusion

In Figure 26 we summarize the results of this research in a schematic, pictorial form. Near the top of the photosphere, the horizontally spreading supergranulation sweeps magnetic fields to the cell boundaries. These fields in turn provide channels in which matter funnels back down into the photosphere from the high chromosphere, and in which enhanced heating of the chromosphere occurs, resulting in the Ca II emission network. Thus, despite the very qualitative, order-of-magnitude nature of some of the calculations and comments discussed above, our observations infer a plausible, consistent picture of supergranulation and its consequences.

Before closing we should mention two areas which did not yield completely satisfactory results and in which further work would be desirable. The first of these is the correlation between the Ca II emission and the magnetic networks. Although the measured K-B correlation below 5 gauss appears to be real and positive, it was certainly not a one-to-one correlation. However, it seems quite possible that the true solar correlation is still one-to-one. If so, then any distortions due to our observing techniques will

gure 26. Schematic model showing supergranulation circulation in the photosphere and downward flowing columns in the chromosphere above the cell boundaries.

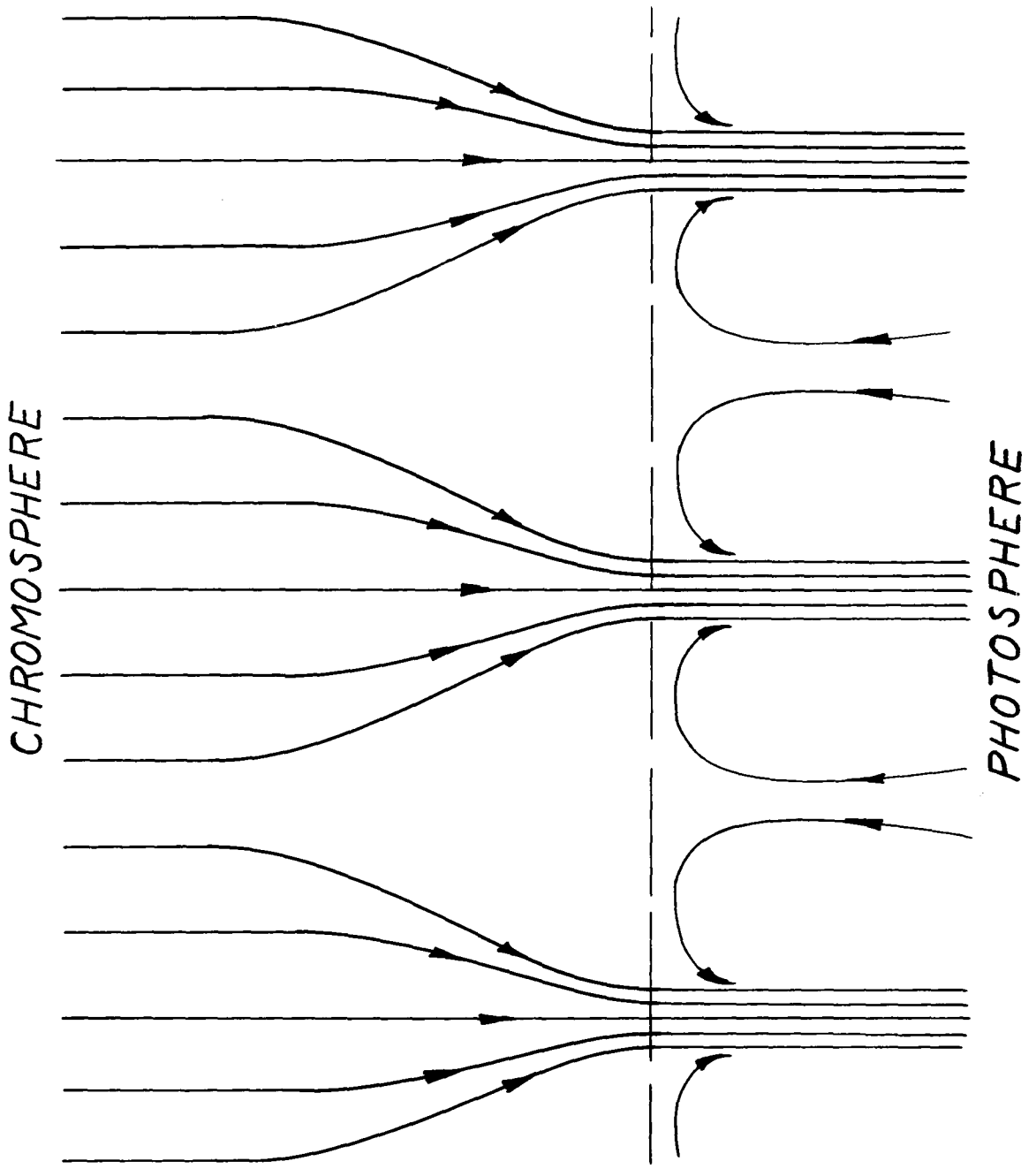

Figure 26

tend to lower the measured correlation. Several such correlation-destroying effects were present. These included poor seeing, the long time (about two hours) needed to complete the magnetic tracings (during which both solar rotation and finite cell lifetime produce an artificial anti-correlation), large aperture (about 7000 km on a side) which "smeared out" small-scale features, the use of drawings of the Ca II network (subject to the observer's judgment concerning the extent of the emission region) and use of line drawings (ref. Figure 22(b)) for the magnetic field regions, close proximity of the solar limb to the measured regions with resultant foreshortening distortions, and finally the fact that the magnetic measurements were made in a photospheric line, while the Ca II emission probably originates some 3000 - 4000 km higher in the atmosphere, where the lines of force are more spread out (due to the lower density), and thus the apparent size of the magnetic field region may be much smaller than the dimensions of the Ca II emission.

Unfortunately it is presently impossible for Howard to make a two-dimensional map of the magnetic field regions using the very small 2 seconds of arc apertures described in reference 48, since there is no way of guiding the solar image accurately enough. This may become feasible in the future, and seems very necessary. In the meantime, improvement in the sensitivity of the X-Y recorder technique so that smaller apertures can be used, would yield valuable information on the K-B correlation. This method has the great

advantage that both channels of the recorder simultaneously see the same spot on the solar surface; the correlation is made automatically without need for elaborate drawings, enlargements, superposition of images, and other hocus-pocus in the laboratory. The preliminary observations of 1962 used an aperture of 10 × 18 seconds of arc. A reduction to 5 × 5 should provide useful new information, while a 2 × 2 aperture would completely clarify the matter of the K-B correlation.*

The second area needing more research is the matter of vertical motions in the supergranulation. No completely satisfactory evidence for such motions was found, other than the indirect correlation with the Ca II emission at the center of the disc. However, although the evidence for vertical velocities in the cells was not too strong, nevertheless it was seen by four different methods, thus adding some confidence to the result. These four techniques were: a) visual and microphotometer measurements of a few cells at the center of the disc on the best LC plates; b) auto-correlation functions at the center of the disc which had widths (FWHM) too large to be due entirely to the small-scale oscillatory field; c) occasional rising motions in the centers of the downward-flowing Hα and Hβ network, reported also by Giovanelli and Jefferies (30), (although these Balmer line observations undoubtedly arise from a higher (500 - 1000 km) level in the atmosphere); and d) the already-

---

* The limitation on aperture size is due mainly to the sensitivity of the photomultiplier tube which observes the Ca II emission.

mentioned K-LC correlation found at the center of the disc, which is clearly the strongest evidence of the four.

Three effects could produce the difficulty in observing the vertical motions. Firstly, they may really be so small that they are difficult to resolve by the Doppler photographic technique. Secondly, they may be hidden from view by a mushrooming cloud top. Thirdly, they may be masked by the small-scale vertical oscillations.

Thus it would be worthwhile to investigate other methods of approaching this problem. For example, it may be possible that the large cells could be seen superimposed on the small-scale granulation. Close inspection of high resolution granulation photos shows not only a scattered number of dark "pores," but also a very fragmentary system of dark, narrow "strips." Perhaps these dark holes and strips are regions where either the large cell vertical motion or the magnetic network is breaking through the granular surface. It will be recalled that numerous authors have reported secondary maxima at about 15000 km in auto-correlation studies of the small-scale granulation. This figure is close enough to supergranulation dimensions to suggest the presence of some features of the large cells. With respect to the large-scale horizontal currents in the granulation reported by Janssen (13), this observer recently had the opportunity of inspecting some of Janssen's photographs in the possession of Pierce (32). We definitely agree with the conclusion of Hansky (14) and Chevalier (15) that Janssen's "photospheric net" was not a solar effect, but due to poor seeing, and

thus there is at present no evidence for large-scale horizontal motions in the granulation outside of sunspot regions. Of course this is also apparent from inspection of the magnificent Stratoscope I photographs (33-35), in which atmospheric seeing problems have been virtually eliminated. None of these show any distortions of the granular pattern which might be due to large horizontal velocities.

Another technique for observing the large cells may be provided by a Doppler motion-picture camera for studying line-of-sight velocities, now being constructed by Title and Leighton (52). This should yield new information on the velocity structure in the supergranulation, if periods of good seeing persist long enough to show observable changes in these long-lived, slowly-moving structures.

A third new approach to the study of the supergranulation might be to follow the life history of individual cells. Up to now we have used mainly statistical analysis of many cells taken together. Because of the long lifetime and large size of a cell, it is likely that one could identify the same cell on plates taken hours, or even a day or more, apart. The main difficulty with this approach is that the cells are visible only near the limb. Thus firstly, we must put up with distortions of the cell shape due to foreshortening. Secondly the cell disappears for several days at the center of the disc and would be very hard to identify positively when it reappears (if, indeed, it had survived that long). Despite these complications, this method should be investi-

gated.

Earlier in the discussion we suggested that the gradual disintegration of sunspots might be due to "erosion" of the penumbral boundaries by the large cell currents. Not only this aspect of possible sunspot-large cell relations needs further study, but also the following idea: Perhaps pores and sunspots are formed directly as the result of the circulation in the supergranulation. This could conceivably happen in either of two ways. First, it has been observed in the study of Bénard cells that small particles, swept to the cell boundaries by the horizontal currents, then flow along the boundary and pile up at the vertices of the polygonal cells. In analogy, if there is a weak magnetic field already present on the solar surface, then the large-cell motions might be expected to concentrate these fields at the polygon vertices, resulting in the small pores seen in granulation photos. The second method of sunspot genesis concerns a completely different aspect of the large cell motions, and requires that the sunspot be formed at the cell centers. This argument states that sunspots may be the result of strong deep-lying magnetic fields which are carried up from below by a rising plume of gas. The well-known Evershed effect may give some credence to the second hypothesis. In the photospheric levels, penumbral velocities are directed radially outward from the umbra, and thus look very much like the large cell motions. Both of these ideas are completely speculative at this time, but clearly deserve detailed study.

Finally, it is hoped that the observations reported in this paper will stimulate theoretical studies which may explain more satisfactorily the true origin and nature of the convective supergranulation.

REFERENCES

1. Noyes, R.W., Ph. D. Thesis, California Institute of Technology, 1963
2. Leighton, R.B., Nuovo Cimento (Supp.), 22, 321-325 (1961)
3. Leighton, R.B., Noyes, R., and Simon, G., Ap. J., 135, 474-499 (1962)
4. Macris, C., Rend. Accad, naz. Lincei Roma VIII, 21, 303 (1956)
5. Macris, C., Mem. Soc. Astron. Ital., 33, 85-95 (1962)
6. Howard, R., Ap. J., 130, 193-201 (1959)
7. Simon, G., and Leighton, R., Astron. J., 68 (1963), (in press)
8. Leighton, R., Ap. J., 130, 366-380 (1959)
9. Babcock, H.W., and Babcock, H.D., Ap. J., 121, 349-366 (1955)
10. Babcock, H.W., Ap. J., 118, 387-396 (1953)
11. Noyes, R., and Leighton, R., Ap. J., 137 (1963), (in press)
12. Wasiutynski, J., Ap. Norvegica, 4, 143-182 (1946)
13. Janssen, J., Ann. Obs. Astr. Phys. Paris, 1, 103 (1896)
14. Hansky, A., Bull. Soc. Astron. France, 23 (1906)
15. Chevalier, S., Ap. J., 27, 12-24 (1908)
16. Hart, A., M. N., 114, 17-38 (1954)
17. Hart, A., M. N., 116, 38-55 (1956)
18. Frenkiel, F., and Schwarzschild, M., Ap. J., 116, 422-427 (1952)
19. Frenkiel, F., and Schwarzschild, M., Ap. J., 121, 216-223 (1955)
20. Stuart, F., and Rush, J., Ap. J., 120, 245-250 (1954)
21. Edmonds, F., Jr., Ap. J., 131, 57-60 (1960)
22. Goldberg, L., Mohler, O., Unno, W., and Brown, J., Ap. J., 132, 184-194 (1960)
23. Evans, J., and Michard, R., Ap. J., 136, 493-506 (1962)
24. Pellew, A., and Southwell, R., Proc. Roy. Soc., A176, 312-343 (1940)
25. Deslandres, H., Comptes Rendus, 129, 1225 (1899)

26. de Jager, C., Handbuch d. Physik, 52, 80-362 (Berlin, Springer-Verlag, 1959)
27. Deslandres, H., Ann. Obs. Astr. Phys. Paris, 4, 116 (1910)
28. de Jager, C., B. A. N., 13, 133-148 (1957)
29. de Jager, C., Colloq. Astrofis. (Supp. Mem. Soc. Astron. Ital.), No. 3, 73-80 (1961)
30. Giovanelli, R., and Jefferies, J., Austr. J. Phys., 14, 212-217 (1961)
31. Rogerson, J., Jr., Ap. J., 121, 204-215 (1955)
32. Pierce, A., private communication, April 1963
33. Danielson, R., Ap. J., 134, 275-288 (1961)
34. Baking, J., and Schwarzschild, M., Ap. J., 134, 312-322 (1961)
35. Schwarzschild, M., Ap. J., 130, 345-363 (1959)
36. Bénard, H., Ann. Chim. Phys., 23, 62-144 (1901)
37. Spiegel, E., private communication, April 1963
38. Batchelor, G., Quart. J. Roy. Meteor. Soc., 80, 339-358 (1954)
39. Woodcock, A., and Riley, G., J. of Meteor., 4, 100-101 (1947)
40. Krueger, A., and Fritz, S., Tellus, 13, 1-7 (1961)
41. Iben, I., Jr., and Sears, R., 1962, unpublished
42. Allen, C., Astrophysical Quantities, p. 133 (London, Athlone Press, 1955)
43. Howard, R., private communications, March - May 1963
44. de Jager, C., Vistas in Astronomy, 4, 143-183 (1961)
45. Osterbrock, D., Ap. J., 134, 347-388 (1961)
46. Beckers, J., Astron. J., 68 (1963), (in press)
47. Fellgett, P., M. N., 119, 475-511 (1959)
48. Howard, R., Ap. J., 136, 211-222 (1962)
49. Kiepenheuer, K., Ap. J., 117, 447-453 (1953)
50. Cowling, T., Magnetohydrodynamics, pp. 77-98 (New York, Interscience, 1957)
51. van de Hulst, H., The Sun, ed. G. Kuiper, Chapt. 5 (Chicago, U. of Chicago Press, 1953)
52. Title, A., and Leighton, R., private communication, April 1963